



universität
wien

MASTERARBEIT / MASTER'S THESIS

Titel der Masterarbeit / Title of the Master's Thesis

„Cation Dynamics in Halide Organometal Perovskites: A
Monte Carlo Method Based on Ab-Initio Molecular
Dynamics“

verfasst von / submitted by

Jonathan Lahnsteiner B.Sc

angestrebter akademischer Grad / in partial fulfilment of the requirements for the degree of
Master of Science (M.Sc)

Wien, 2016 / Vienna 2016

Studienkennzahl lt. Studienblatt /
degree programme code as it appears on
the student record sheet:

A 066 862

Studienrichtung lt. Studienblatt /
degree programme as it appears on
the student record sheet:

Masterstudium
Chemie UG2002

Betreut von / Supervisor:

Univ.-Prof. Dipl.-Ing. Dr. Georg Kresse

Mitbetreut von / Co-Supervisor:

Jonathan Lahnsteiner

Curriculum Vitae

Education

- 01.10.2013–present **Master of Science**, *The University of Vienna*, Vienna.
Chemistry
- 2011–2012 **Bachelor of Science**, *The University of Vienna*, Vienna.
Chemistry
- 20.10.2009 **University entrance exam**, *The University of Vienna*, Vienna.
Chemical Institute
- 01.04.2008–31.12.2008 **Civil service**, *PVA*, Bad Ischl.
- 2004–2008 **Apprenticeship laboratory chemist**, *Solvay Group*, Ebensee.

Masters Thesis

- Title *Perovskite solar cells*
- Supervisors Univ.-Prof. Dipl.Ing. Dr. Georg Kresse & Dr. Menno Bokdam
- Description This thesis should figure out the influence of organic ions in perovskite solar cells on the high efficiency of the material

Experience

Vocational

- 2004–2008 **Laboratory Chemist**, SOLVAY GROUP, Ebensee.
Micro analysis of inorganic resources and products; environmental analysis
- Detailed achievements:
- Trace element analysis
 - Application of ICP and AAS
 - Developing methods for ICP and AAS which were used in- house
 - Environmental analysis
 - Analysis of impurities in lake water
 - Heavy metal analysis in water and soils
- 2004–2008 **Bioanalyst**, INSTITUT FÜR GEWÄSSERÖKOLOGIE, FISCHEREIBIOLOGIE UND SEENKUNDE, Mondsee.
Environmental analysis
- Detailed achievements:
- Environmental analysis
 - Analysis of impurities in lake water

Währinger Gürtel 59/ 20 – Wien, 1180

☎ (0043) 650 561 6621 • ✉ jonathan.lahnsteiner@gmx.at

Contents

1	Introduction	3
2	Background	4
2.1	Halide- Perovskite Structure	4
2.2	Important Interactions	4
2.3	Foregoing Ab Initio Molecular Dynamics Simulations	5
3	Methods	6
3.1	Density functional theory	6
3.1.1	Hohenberg- Kohn approach	6
3.1.2	Kohn- Sham self consistent field equations	9
3.2	Local- density approximation	11
3.3	Generalized gradient approximation- PBE exchange correlation	13
3.4	Perdew-Burke-Ernzerhof revised for solids	15
3.5	Generalized gradient approximation with included dispersion interactions	17
3.6	Molecular Dynamics	18
3.7	Monte Carlo Metropolis-Rosenbluth algorithm	19
4	Computational Details	20
4.1	Considered Organo-Halide Perovskite Systems	20
4.2	Ab-initio Molecular Dynamics Simulation	22
4.3	Monte Carlo approach	22
5	Results	24
5.1	Dipole moments of organic molecules	24
5.2	Molecular Dynamics	26
5.2.1	Heat capacity from of ab-initio molecular dynamics simulations	26
5.2.2	Autocorrelation functions of ab-initio molecular dynamics	28
5.2.3	Comparing $CH_3NH_3^+$ orientations for different starting structures and system sizes	31
5.2.4	Behaviour of the inorganic framework	38
5.2.5	Comparing ab- initio molecular dynamics of two different exchange correlation potentials	40
5.2.6	Considering different coordination spheres	41
5.2.7	Correlation of $CH_3NH_3-CH_3NH_3$ and $PbI_3-CH_3NH_3$ movement	45
5.2.8	Comparing two simulations with different hydrogen masses	47
5.3	Comparing Polarization of different simulations	50
5.4	Parametrization of Monte Carlo Approach	52
5.5	Monte Carlo model	56
5.5.1	Single Layer Simulations	56
5.5.2	Comparing ab- initio molecular dynamics results with Monte Carlo results	59
5.5.3	Comparing two 0K structures	62
5.5.4	Calculating hysteresis of polarization when applying an electric field	66
5.5.5	Local Polarisation which arises due to the dipole contribution	68
5.5.6	Temperature dependence of Polarization	71

6	Conclusion	74
7	Outlook	75
8	Appendix	76
8.1	Abstract	76
8.2	Zusammenfassung	77

1 Introduction

Perovskite solar cells have become very famous in the recent years within the photo voltaic community. The main reason for this are the high efficiencies that can be reached with those cells, the low costs and the ease in production. There exist publications reporting perovskite cells with efficiencies of 15 % [7]. Moreover, Nam-Gyu reported in April 2013 that it will be possible to drive the efficiency of those cells even further and reach values of about 20 % [38]. Approximately one year later there were research groups that were able to build perovskite cells with efficiencies of 19.6 % and wrote that it will be possible to improve these materials even further [45]. These few examples indicate the fast development of the perovskite solar cell field.

But this is not the only reason why perovskite solar cells receive so much attention. Another reason is that they are very easy to produce for example by coating TiO_2 or Al_2O_3 with very thin perovskite layers [18]. Furthermore they possess a very high light absorption coefficient [18][38] whereby the maximum of the absorption coefficient is at about 410 nm [39].

But there are also some negative properties which can be associated with the perovskite solar cell. The most harmful is maybe that a main component of the cell is lead which is very toxic. This may cause troubles during the fabrication, during application or after the disposal of these cells[18].

Nevertheless, these solar cells are very promising and one should try to understand the mechanisms behind them, which cause the high efficiencies. Maybe then it would also be possible to replace the harmful lead by other metals.

This work will deal in a completely theoretical way with the behaviour of the hybrid-halide organo metal perovskite solar cells. In the beginning, the results gained from foregoing works, (mainly theoretical in nature) will be summarized. This illustrates the starting point for this work. Afterwards, the methods that were used and their suitability for the considered problem will be discussed. First we used an ab initio molecular dynamics approach and second a Monte Carlo approach which we then compare to.

2 Background

2.1 Halide- Perovskite Structure

First, the structure of the system that will be considered in this work should be described. The common chemical formula expressing halide perovskites reads as ABX_3 . Where X is a monovalent anion, which can be one of the halogenides. In this work we will only consider iodine. Then B can be any bivalent metallic cation, for which we will take lead in the present thesis. Then last A describes a monovalent cation. This can be either organic or inorganic in nature. For the monovalent cation, we considered methyl ammonium, which possesses a permanent dipole moment. The chemical formula for the considered system reads as $CH_3NH_3PbI_3$. Such a structure can be seen in figure 2.1. Every lead atom (with an ionic radius of $R_B = 0.119$ nm) is surrounded by six iodine atoms (ionic radius of $R_X = 0.220$ nm) [18]. These iodine atoms form an octahedron with the lead atom in its center. The bonds between the iodine atoms and the lead atoms are heteropolar. This means that they are mixed out of ionic and covalent bonds [3]. The valence band is mainly formed by the p orbitals of the iodine atoms with a little admixture of the s orbitals of the lead atoms. The energetically higher lying conduction band is made up of the p orbitals of the lead atoms [3].

The organic cations are locked inside the cages. These are built up of the quadratic bipyramids of the lead and iodine atoms. Methyl ammonium is an organic cation with a ionic radius of $R_A = 0.18$ nm [34]. Also other organic cations have been considered in previous studies like ethyl ammonium or formamidinium. The methyl ammonium cation possesses a permanent dipole moment, which reads for the neutral species as 2.29 D [16]. For the spacing between the dipole molecules values between 6.00 Å [3] and 6.29 Å [17] have been published.

The system is able to posses several crystallographic structures: orthorhombic, tetragonal, and cubic. The orthorhombic structure is stable beneath 160 K and undergoes a phase transition to the tetragonal symmetry at approximately this temperature [16]. There is another transition to the high temperature phase which is cubic at 330 K [46] and which we will consider in the recent work.

2.2 Important Interactions

Because the methyl ammonium cation is positively charged and the PbI_3 is a negatively charged framework surrounding the organic molecule, the main interaction between the two species should be electrostatic in nature. It is assumed that there exists a strong electrostatic potential which hinders the dipoles in their rotation. The rotation barrier energies for different ions have been reported. For example the rotation barrier for NH_4^+ is estimated to be 0.3 kJ/mol, for $CH_3NH_3^+$ 1.3 kJ/mol and for $NH_2CHNH_2^+$ 13.9 kJ/mol [16]. One can see the rotational barrier increases with the size of the ion. The next important contribution should be the dipole charge interaction which also arises between the molecule and the framework. For sure this interaction has to be dependent on the orientation of the considered dipole [3]. An ab- initio molecular dynamics simulation suggests that also hydrogen bonding should have a significant influence on the interaction of the dipoles with the framework and the behaviour of the perovskite system [8]. This interaction arises between the hydrogens located on the nitrogen atoms of the, for example, methyl ammonium cation and the partly negatively charged iodine atoms of the cage. All

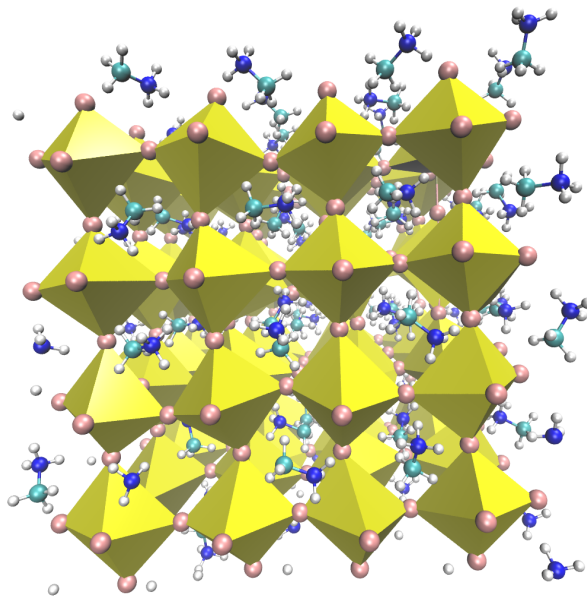


Figure 2.1: Organohalide perovskite structure at 300 K

of these interactions are electrostatic in nature and thus it should be very difficult to distinguish between them [3]. The next contribution that should have an influence on the behaviour of the considered system are dipole-dipole interactions between the molecules. Their contribution should have less influence on the system because it may be shielded by the PbI_3 framework which is located between the interacting dipoles. A measure for the extend of the shielding may be the dielectric constant of the framework where published values are around $\epsilon_0 = 24.1$ and $\epsilon_\infty = 4.5$ [17]. The dielectric constant can be written as a sum of different contributions $\epsilon_0 = \epsilon_\infty + \epsilon_{\text{ionic}} + \epsilon_{\text{other}}$. In this sum, ϵ_∞ denotes the electronic contribution to the relative epsilon, and ϵ_{ionic} the contribution which arises due to the present ions which are moving in an oscillating field. The ϵ_{other} contribution arises for example due to molecules with a permanent dipole moment present in the system as is the case for CH_3NH_3^+ [16].

Moreover Egger and Kronik reported that it should also be very important to include VdW interactions when performing an ab initio- molecular dynamics simulation. In their paper, they report that the cell volume would slightly decrease if one includes VdW interactions resulting in better agreement with experiments [15]. So in this work we will try two different approaches for small $2 \times 2 \times 2$ cells to see how the choice of the DFT functional- with and without VdW interactions- will influence the results and especially the dynamical behaviour of the system. The $2 \times 2 \times 2$ cells denote systems that have a cubic symmetry and consisting of 8 dipoles (methyl- ammonium cations) and 8 PbI_3 units in total.

2.3 Foregoing Ab Initio Molecular Dynamics Simulations

In this section the results of two foregoing molecular dynamics simulations are discussed. One of them was performed by Quarti et al. and another by Carignano et al. First of

all one has to be careful to take a sufficiently long equilibration time for the considered system. For a $3 \times 3 \times 3$ super cell one should take at least a minimum of 5 ps for the initial equilibration of the considered system [8]. This equilibration time is expected to increase with growing system size which was reported by Carigano et. al. by comparison of a $2 \times 2 \times 2$ and a $3 \times 3 \times 3$ super cell [8]. The starting geometry of the considered system should be chosen very carefully. For example Quarti et al. tested three tetragonal structures with various initial orientations of the methyl ammonium molecules. They tested a system which they called $MA\beta 1$ which has an isotropic (random) orientation of the dipoles in the **ab** plane and an anisotropic behaviour in the **c** direction. This is because the angle between the dipoles and the **ab** plane is written as $\approx 30^\circ$. As a result this structure shows polarization along the **c** axis.

This structure was compared to two systems they denoted as $MA\beta 2$ and $MA\beta 3$ which possess an isotropic behaviour (random orientation) in both the **ab** plane and the **c** axis and therefore they are para electric. The $MA\beta 2$ structure possesses a symmetry plane at half of the **c** axis which is not present in the $MA\beta 3$ structure. So $MA\beta 2$ has two oppositely polarized domains. For these structures they calculated the radial distribution functions of the framework (the PbI_3 cages) which differ in the broadening and height of the corresponding peaks. From this behaviour they concluded that the dynamics of the inorganic framework are not decoupled from the organic compounds locked inside the cages. The larger broadening was found due to a diminished long range order. This long range order decreases from the $MA\beta 1$ to the $MA\beta 2$ and $MA\beta 3$ [44].

Moreover, Carigano et. al. reported that the crystalline structure of the system is stable during the whole simulation when using a DFT approach for the electronic structure and Langevin dynamics for the propagation of the ions. Out of this they concluded that this will be an adequate approach for systems of this kind [8]. As mentioned in section 2.2, hydrogen bonds must play an important role when considering the interactions of the halide perovskite cages and the organic cations. However, the structures reported by Quarti et al. show a decreasing number of hydrogen bonds from $MA\beta 1$ to $MA\beta 3$. That may also be why they report that the $MA\beta 1$ structure is the most stable one.

Another very interesting fact is that the nitrogen atoms are oriented towards the face centres of their cubic cages which is a sterically unfavourable orientation because the most space would be available for the molecules, if they are arranged along the room diagonal but this might also arise due to the presence of hydrogen bonding [8].

3 Methods

3.1 Density functional theory

3.1.1 Hohenberg- Kohn approach

To determine the electronic structure of the systems we used the well known Density Functional Theory method. The DFT method was proposed by Hohenberg and Kohn [24] and further developed by Kohn and Sham [51]. The main difference of DFT to other methods for the determination of electronic structures is, that the energy is expressed in terms of the electronic density and not in terms of the wavefunction like for example in the Hartree Fock method.

First of all, one has to define a Hamiltonian which specifies the corresponding problem

completely. In the case of an electronic structure problem it can be written in the form

$$H = T_e + T_N + V_{ee} + V_{eN} + V_{NN}. \quad (3.1)$$

T_e denotes the kinetic energy related to the electrons which are moving in the ionic potential. T_N denotes the kinetic energy related to the movement of the nuclei. The potential V_{ee} and V_{NN} denotes the repulsive electrostatic interaction between electrons and the nuclei respectively. The last term V_{eN} describes the attractive interaction between electrons and nuclei. The operators for those terms can be written like shown in equation (3.2) if one uses atomic units:

$$\hat{H} = \frac{1}{2} \sum_i^N \Delta_i + \frac{1}{2} \sum_n^M \Delta_n + \frac{1}{2} \sum_{i \neq j} \frac{1}{|r_i - r_j|} + \frac{1}{2} \sum_{i,n} \frac{Z}{r_i - R_n}. \quad (3.2)$$

In this equation, Δ_i denotes the Laplacian (second derivative) with respect to the electronic coordinates and Δ_n with respect to nuclear coordinates. Now one is able to apply the Born Oppenheimer approximation. This allows us to uncouple the movement of the electrons from those of the nuclei. This seems to be a good approximation because the electrons tend to move much faster than the nuclei and therefore the nuclei can be regarded as stationary while the electrons propagate fast in time. The Schrödinger equation can be seen in 3.3 for the coupled case. After application of the Born Oppenheimer approximation [6] and choosing a product ansatz for the wavefunction $\Psi(\mathbf{x}, \mathbf{X}) = \varphi(\mathbf{x}) \theta(\mathbf{X})$ one is able to write the Schrödinger equation like

$$\hat{H}\Psi(\mathbf{x}, \mathbf{X}) = E\Psi(\mathbf{x}, \mathbf{X}), \quad (3.3)$$

$$\hat{H}\varphi(\mathbf{x})\theta(\mathbf{X}) = E\varphi(\mathbf{x})\theta(\mathbf{X}). \quad (3.4)$$

In these formulas the coordinates \mathbf{x} and \mathbf{X} denote the coordinates of all the electrons and all the nuclei present in the considered system respectively. The last equation can be separated in a way that the equation is only dependent on electronic contributions and therefore one obtains the electronic Schrödinger equation.

$$(\hat{T}_e + \hat{V}_{ee} + \hat{V}_{eN})\varphi(\mathbf{x}) = \epsilon\varphi(\mathbf{x}). \quad (3.5)$$

Now we have an equation that will give us the electronic energy in the mean field of stationary nuclei which will be in general a good approximation for describing molecules or solids.

As already mentioned, the DFT method deals with electron densities. But the equations we have seen till now only deal with wavefunctions so we have to introduce the electron density in terms of the wavefunction:

$$n(\mathbf{r}) = \langle \varphi | \mathbf{r} \rangle \langle \mathbf{r} | \varphi \rangle \quad (3.6)$$

Now one is able to rewrite Schrödinger's equation in terms of the electron density and transform it in a way that we get a functional expression for the ground state energy. This was done by Hohenberg and Kohn:

$$E[n(\mathbf{r})] = \int v(\mathbf{r})n(\mathbf{r})d\mathbf{r} + \langle \Psi | \hat{T} + \hat{U} | \Psi \rangle. \quad (3.7)$$

Hohenberg and Kohn [24] postulated that the potential $v(\mathbf{r})$ is a unique functional of the electronic ground state density $n(\mathbf{r})$. This can be proven by reductio absurdum. Assume we have two potentials $v(\mathbf{r})$ with ground state wavefunction Ψ_0 (energy E_0) and a second potential $v'(\mathbf{r})$ with a wavefunction Ψ' which gives the same electron density $n(\mathbf{r})$. For sure the ground state wavefunction is the state with the lowest energy for the considered system and all the others must have higher energies which is in accordance with the variational principle.

$$E' = \langle \Psi' | \hat{H}' | \Psi' \rangle < \langle \Psi | \hat{H}' | \Psi \rangle = \langle \Psi | \hat{H} + \hat{V}' - \hat{V} | \Psi \rangle \quad (3.8)$$

This results in

$$E' < E + \int [v(\mathbf{r}) - v'(\mathbf{r})]n(\mathbf{r})d\mathbf{r} \quad (3.9)$$

Now one is able to interchange primed and unprimed terms and add these two equations which yields (3.11). This inequality can not be true and therefore $v(\mathbf{r})$ has to be a unique functional of $n(\mathbf{r})$.

$$E < E' + \int [v'(\mathbf{r}) - v(\mathbf{r})]n(\mathbf{r})d\mathbf{r} \quad (3.10)$$

$$E + E' < E' + E \quad (3.11)$$

The only exception to this situation would be if $v(\mathbf{r}) - v'(\mathbf{r}) = \text{const}$. This implies that the potentials can only be determined up to an additive constant. The wavefunction can be determined uniquely out of the electron density too. This will be clear if one takes the Schrödinger equation and inserts the uniquely defined external potential belonging to the ground state electron density. Now if one solves this differential equations one will obtain the wavefunctions associated with the ground state electron density. Therefore one can write the energy associated with the kinetic energy and the interaction of the electrons as follows:

$$F[n(\mathbf{r})] = \langle \Psi[n] | \hat{T} + \hat{U} | \Psi[n] \rangle. \quad (3.12)$$

The total energy functional used in DFT has to be a unique functional of $n(\mathbf{r})$ too which follows from the fact that all the contributions are unique. For the proof assume that one has a specific electron density $n^{(1)}(\mathbf{r})$ which corresponds to a certain external potential $v^1(\mathbf{r})$ and with a many body wavefunction $\Psi^{(1)}$. Now the energy can be expressed as shown:

$$E^1 = E_{HK}[n^{(1)}] = \langle \Psi^{(1)} | \hat{H} | \Psi^{(1)} \rangle. \quad (3.13)$$

Now assume you have another wavefunction which will be denoted by $\Psi^{(2)}$ which corresponds to an other electron density $n(\mathbf{r})$. Now inserting this equation into the energy functional yields:

$$E^{(1)} = \langle \Psi^{(1)} | \hat{H} | \Psi^{(1)} \rangle < \langle \Psi^{(2)} | \hat{H} | \Psi^{(2)} \rangle = E^{(2)} \quad (3.14)$$

It follows the ground state wavefunction is uniquely defined and hence the ground state electron density too. Now the functional for the total energy can be rewritten as follows:

$$E[n] = \int v(\mathbf{r})n(\mathbf{r})d\mathbf{r} + F[n]. \quad (3.15)$$

The Ritz-Rayleigh [4] variational principle states that the exact ground state energy has to be the minimum of this energy functional. This can be done by choosing a first trial density $\tilde{n}(\mathbf{r})$ which is in principle done by taking a first approximation of $\tilde{\Psi}$ and out of it one calculates the electron density. Now one has to minimize equation (3.15) with respect to the electron density. An important boundary condition to the problem is that the integral over the electron density has to yield the number of electrons $N = \int n(\mathbf{r})d\mathbf{r}$.

Now one is able to rewrite the functional $F[n(\mathbf{r})]$ shown in equation (3.12) as a sum of a kinetic energy term, a classical Coulomb energy term and last one adds the contributions due to quantum mechanical effects like correlation and exchange of the electrons. This results in this equation

$$F[n(\mathbf{r})] = T_s[n] + \frac{1}{2} \int \frac{n(\mathbf{r})n(\mathbf{r}')}{|\mathbf{r} - \mathbf{r}'|} d\mathbf{r}d\mathbf{r}' + E_{XC}[n], \quad (3.16)$$

where the effects of exchange and correlation are summarized in one single term ($E_{XC}[n(\mathbf{r})]$) called the exchange correlation functional [51].

3.1.2 Kohn- Sham self consistent field equations

In 1965 Hartree published his self consistent field equations in which one has to solve a set of single particle Schrödinger equations [50] [22]. Every electron moves in a potential arises from the nuclei and all the other electrons:

$$V(\mathbf{r}) = -\frac{Z}{|\mathbf{r}|} + \int \frac{n(\mathbf{r}')}{|\mathbf{r} - \mathbf{r}'|} d\mathbf{r}'. \quad (3.17)$$

One then has to solve the single particle Schrödinger equations in the Hartree approximation that is given by

$$\left[-\frac{1}{2} \Delta + V(\mathbf{r}) \right] \varphi_j(\mathbf{r}) = \epsilon_j \varphi_j(\mathbf{r}), \quad (3.18)$$

where the $\varphi_j(\mathbf{r})$ denote the single electron wavefunctions and the ϵ_j the corresponding energies. Kohn and Sham now used this Hartree approach for the derivation of a set of self consistent equations which are known as the Kohn-Sham equations. Therefore they used the Hartree system where no exchange correlation energies are included as a non interacting reference system and took the Hamiltonian out of equation (3.17) as the auxiliary Hamiltonian. Moreover the spin contributions which are very important for fermions are taken into account. One has to rewrite the electron density in terms of a density for the spin up particles and the spin down particles

$$n(\mathbf{r}, \sigma) = n(\mathbf{r}, \uparrow) + n(\mathbf{r}, \downarrow) = \sum_{\sigma} \sum_{i=1}^{N^{\sigma}} |\varphi_i^{\sigma}(\mathbf{r})|^2. \quad (3.19)$$

This spin contributions also have to be taken into account for the auxiliary system Hamiltonian which looks like

$$\hat{H}_{aux}^{\sigma} = -\frac{1}{2} \Delta + V^{\sigma}(\mathbf{r}) \quad (3.20)$$

Now we will write down the kinetic energy of this auxiliary system:

$$T_s = -\frac{1}{2} \sum_{\sigma} \sum_{i=1}^{N_{\sigma}} \int |\nabla \varphi_i^{\sigma}(\mathbf{r})|^2 d\mathbf{r} \quad (3.21)$$

Lets us also define the Hartree energy,

$$E_{\text{Hartree}}[n] = \frac{1}{2} \int \frac{n(\mathbf{r})n(\mathbf{r}')}{|\mathbf{r} - \mathbf{r}'|} d\mathbf{r} d\mathbf{r}' \quad (3.22)$$

We are now able to define the Kohn Sham functional for the electronic system in the ground state.

$$E_{\text{KS}}[n] = T_s[n] + \int V_{\text{ext}}(\mathbf{r})n(\mathbf{r})d\mathbf{r} + E_{\text{Hartree}}[n] + E_{\text{II}} + E_{\text{XC}}[n] \quad (3.23)$$

In equation 3.23 $T_s[n]$ denotes the kinetic energy of the non interacting electron gas. $V_{\text{ext}}(\mathbf{r})$ denotes the potential which arises due to the electron- nuclei attraction. E_{Hartree} is the Hartree energy of equation (3.22) and E_{II} denotes the contribution of the interaction between the nuclei. By comparing the Kohn- Sham equation (3.23) and the Hohenberg-Kohn equation one can write the exchange- correlation functional in terms of equation (3.16):

$$E_{\text{XC}}[n] = F_{\text{HK}}[n] - (T_s[n] + E_{\text{Hartree}}[n]). \quad (3.24)$$

One can see that this is just the difference in energy between the auxiliary system where only classical Coulomb interactions are present and the interacting electronic system. In other words, the exchange correlation energy takes into account all the exchange and correlation effects which are present in a many body system which were neglected in the system of the non interacting electrons [33].

The next step is to find the stationary condition of the the Kohn Sham equation which can be done by minimizing the functional with respect to the electronic density, i.e. finding the first deviation with respect to the density and setting this to zero. There is just one problem; the kinetic energy of T_s of the non interacting electron gas is defined in terms of the orbitals and not the electronic density. But this can be solved by taking the derivative of the functional with respect to the orbitals φ_i^{σ} and applying the chain rule. The result can be seen in the next equation

$$\frac{\partial E_{\text{KS}}}{\partial \varphi_i^{\sigma*}(\mathbf{r})} = \frac{\partial T_s}{\partial \varphi_i^{\sigma*}(\mathbf{r})} + \left[\frac{\partial E_{\text{ext}}}{\partial n(\mathbf{r}, \sigma)} + \frac{\partial E_{\text{Hartree}}}{\partial n(\mathbf{r}, \sigma)} + \frac{\partial E_{\text{XC}}}{\partial n(\mathbf{r}, \sigma)} \right] \frac{\partial n(\mathbf{r}, \sigma)}{\partial \varphi_i^{\sigma*}(\mathbf{r})} = 0 \quad (3.25)$$

The derivation of the kinetic energy term yields:

$$\frac{\partial T_s}{\partial \varphi_i^{\sigma*}(\mathbf{r})} = -\frac{1}{2} \Delta \varphi_i^{\sigma}(\mathbf{r}) \quad (3.26)$$

And the derivation of the density with respect to the wavefunction results in:

$$\frac{\partial n(\mathbf{r}, \sigma)}{\partial \varphi_i^{\sigma*}(\mathbf{r})} = \varphi_i^{\sigma}(\mathbf{r}) \quad (3.27)$$

First one introduces now the constraints which read as $\langle \varphi_i^{\sigma} | \varphi_j^{\sigma'} \rangle = \delta_{i,j} \delta_{\sigma, \sigma'}$. This is nothing than the ortho-normalization principle well known for one electron wavefunctions.

Finally, one can write down a Schrödinger like equation which is known as the Kohn-Sham variational equation where ϵ_i^σ denotes the Lagrange multiplier which takes into account the normalization constraint.

$$(\hat{H}_{KS}^\sigma - \epsilon_i^\sigma)\Psi_i^\sigma(\mathbf{r}) = 0 \quad (3.28)$$

The operator \hat{H}_{KS}^σ of equation (3.28) can be written in the following form:

$$H_{KS}^\sigma(\mathbf{r}) = -\frac{1}{2} \Delta + V_{\text{ext}}(\mathbf{r}) + V_{\text{Hartree}}(\mathbf{r}) + V_{\text{XC}}^\sigma(\mathbf{r}) \quad (3.29)$$

With this equation one is able to calculate the ground state of the considered electronic system with a self consistent field approach. It is important to mention that one has to solve a set of single particle equations one for every $\varphi_i^\sigma(\mathbf{r})$ and ϵ_i^σ . Now one is able to calculate the total energy of the system by the use of equation (3.23) and inserting the terms for the electron density (3.19), the expression for the kinetic energy given by (3.21) and the Hartree energy term (3.22). Here it is important to note that the Lagrange multipliers do not resemble the orbital energies of the considered system. Only the the multiplier with the highest energy reflects in “exact” DFT the negative ionization energy of the system. Nevertheless the remaining multipliers can be used to make perturbation approaches for the calculation of excitation energies. The ground state could be calculated, in principle, with arbitrary precision if the exchange correlation potential would be known exactly and therefore the Kohn Sham theory is an exact approach. But it has to be solved using an approximate exchange correlation potential. Some approaches for the determination of the exchange correlation energy will be discussed in the following chapters. There the LDA and the GGA method will be presented.

3.2 Local- density approximation

The easiest of the practical used exchange correlation functionals is maybe the LDA approach. This energy functional may in general be written in the following form [50]:

$$E_{XC}^{LDA}[n(\mathbf{r})] = \int e_{XC}(\mathbf{r}; [n(\tilde{\mathbf{r}})])n(\mathbf{r})d\mathbf{r} \quad (3.30)$$

In this equation $e_{XC}(\mathbf{r}; [n(\tilde{\mathbf{r}})])$ represents an exchange correlation energy density which has the units energy per particle and is dependent on the density distribution $n(\tilde{\mathbf{r}})$ around \mathbf{r} . As a cut off radius one uses the so called Fermi wavelength which is defined as $\lambda_F = [3\pi^2 n(\mathbf{r})]^{-\frac{1}{3}}$ [50]. An evaluation of the functional for exchange only was given in the paper of Kohn Sham [51] where they started with the Hartree-Fock exchange operator which can be seen in equation (3.31). This operator can be regarded as the potential on the k th orbital.

$$v_{xk}(\mathbf{r}) = - \sum_{k'=1}^N \int \frac{\Psi_k^*(\mathbf{r})\Psi_{k'}^*(\mathbf{r}')\Psi_{k'}(\mathbf{r})\Psi_k(\mathbf{r}')}{|\mathbf{r} - \mathbf{r}'| \Psi_k^*(\mathbf{r})\Psi_k(\mathbf{r})} \quad (3.31)$$

If the orbitals are now considered as plane waves ($e^{\pm i\mathbf{k}\mathbf{r}}$) one is able to evaluate the integral of equation (3.31) as:

$$v_{\mathbf{x}k} = -\frac{k_F(\mathbf{r})}{\pi} \left[1 + \frac{k_F^2(\mathbf{r}) - k^2}{2kk_F(\mathbf{r})} \ln \left| \frac{k + k_F(\mathbf{r})}{k - k_F(\mathbf{r})} \right| \right] \quad (3.32)$$

Now one is able to plug in the magnitude of the Fermi wave vector which is defined as $k_F = [3\pi^2 n(\mathbf{r})]^{1/3}$. By combining this with equation (3.32) one gets the Slater exchange correlation functional (3.33) and by setting k_F equal to k one gets the exchange potential which was derived by Kohn- Sham [51].

$$v_{xk}(\mathbf{r}) = -(3/2\pi)[3\pi^2 n(\mathbf{r})]^{1/3} \quad (3.33)$$

$$\mu_x(\mathbf{r}) = -(1/\pi)[3\pi^2 n(\mathbf{r})]^{1/3} \quad (3.34)$$

So equation (3.34) represents only the exchange correction to the potential but Slaters expression resembles both the exchange and the correlation contribution to the potential. Note these two potentials differ only by a factor of 3/2. The exchange correlation energy can also be written as a sum of the individual contributions $E_{XC}^{LDA} = E_X^{LDA} + E_C^{LDA}$. The exchange part was formulated by Kohn-Sham [51] and the correlation functional was first estimated by Paul Wigner in 1938 [50][55][54]:

$$\epsilon_x(n) = \frac{0.458}{r_s}, \quad (3.35)$$

$$\epsilon_c(n) = \frac{0.44}{r_s + 7.8}. \quad (3.36)$$

Here r_s denotes the Wigner Seitz radius which is defined as $r_s = \left(\frac{3}{4\pi\rho}\right)^{1/3}$ and therefore depending on the electron density. The Wigner Seitz radius is the radius of a sphere which contains one electron in the homogenous electron gas [33]. The LDA potential gives normally very good results for the determination of the bond lengths, but has some difficulties when calculating excitation or ionization energies [50]. The local spin density approximation (LSDA) can now be extended in a way that also spin contributions will be taken into account. The functional is now dependent on two different densities one for spin up and the other with spin down. The two different spin densities give in sum the total electronic density. Now one is able to rewrite the local density approximation in a form such that the spin densities are also taken into account

$$\begin{aligned} E_{XC}^{LSDA}[n_\uparrow, n_\downarrow] &= \int n(\mathbf{r}) \epsilon_{XC}^{hom}(n_\uparrow(\mathbf{r}), n_\downarrow(\mathbf{r})) d\mathbf{r} \\ &= \int n(\mathbf{r}) [\epsilon_X^{hom}(n_\uparrow(\mathbf{r}), n_\downarrow(\mathbf{r})) + \epsilon_C^{hom}(n_\uparrow(\mathbf{r}), n_\downarrow(\mathbf{r}))] d\mathbf{r}. \end{aligned} \quad (3.37)$$

The term $\epsilon_X^{hom}(n_\uparrow(\mathbf{r}), n_\downarrow(\mathbf{r}))$ which describes the exchange energy per particle of the homogenous electron gas can be written as a sum of the exchange energy per electron arising due to the spin densities $n_\uparrow(\mathbf{r})$ and $n_\downarrow(\mathbf{r})$ which is written as [33]

$$\epsilon_X^{hom}(n_\uparrow(\mathbf{r}), n_\downarrow(\mathbf{r})) = \epsilon_X^{hom}(n_\uparrow(\mathbf{r})) + \epsilon_X^{hom}(n_\downarrow(\mathbf{r})). \quad (3.38)$$

Now one defines the spin polarization [33] as

$$\xi(\mathbf{r}) = \frac{n_\uparrow(\mathbf{r}) - n_\downarrow(\mathbf{r})}{n(\mathbf{r})}. \quad (3.39)$$

Out of equation (3.38) and (3.39) one is able to formulate the exchange energy density in the LSDA approximation like it is shown in equation (3.40) and (3.41). This was carried

out first by Barth et. al. [49]. If the densities for the individual spin states are equal then equation (3.40) reduces to the exchange energy per electron for the spin unpolarized case which was already mentioned in equation (3.35).

$$\epsilon_X[n, \xi] = \epsilon_X(n, 0) + [\epsilon_X(n, 1) - \epsilon_X(n, 0)]f(\xi) \quad (3.40)$$

$$f(\xi) = \frac{1}{2} \frac{(1 + \xi)^{\frac{4}{3}} + (1 - \xi)^{\frac{4}{3}} - 2}{2^{\frac{1}{3}} - 1} \quad (3.41)$$

The correlation energy is much more complicated to determine. One is also able to take the correlation energy of equation (3.36) like it was proposed by Wigner [55][54] and make the same ansatz like in the case of the exchange energy. This can be seen in the next equation:

$$\epsilon_C[n, \xi] = \epsilon_C(n, 0) + [\epsilon_C(n, 1) - \epsilon_C(n, 0)]f(\xi). \quad (3.42)$$

An other much more accurate approach for the correlation energy was made by Ceperley and Alder. They performed a Monte Carlo approach to treat the correlation of the many body system [10]. The local density approximation and the local spin density approximation were developed for homogeneous electron systems and therefore they yield quite good results for slowly varying electron densities [50] like it would be expected for a local exchange and correlation ansatz. But one also has to consider systems which are not as homogeneous in a way that they could be treated with these local approximations are the reason why scientists developed the so called generalized gradient approximations which will be discussed in the next sections.

3.3 Generalized gradient approximation- PBE exchange correlation

Further development of LDA and LSD has lead to the formulation of generalized gradient approximations. When using GGA exchange correlation potentials one does not only deal with the different spin densities but also with the derivatives. This section will mainly be based on the paper of Perdew et.al. [40] and should show the principle in which they derived their exchange correlation potential. One can see the GGA functional as a generalization of the local spin density approximation and the functional can in general be written in the following form [40]:

$$E_{XC}^{GGA}[n_{\uparrow}, n_{\downarrow}] = \int f(n_{\uparrow}(\mathbf{r}), n_{\downarrow}(\mathbf{r}), \nabla n_{\uparrow}(\mathbf{r}), \nabla n_{\downarrow}(\mathbf{r})) \quad (3.43)$$

One starts derivating the correlation part of the GGA with the correlation energy density of the homogenous electron gas $n[\epsilon_C^{hom}(r_s, \xi)]$ like it was shown for the LSDA. But now one introduces a correction term $H(r_s, \xi, t)$ to the functional which is written as:

$$E_C^{GGA}[n_{\uparrow}, n_{\downarrow}] = \int d\mathbf{r} n[\epsilon_C^{hom}(r_s, \xi) + H(r_s, \xi, t)]. \quad (3.44)$$

In this equation t denotes a dimensionless density gradient which can be written as $t = |\nabla n|/(2\varphi k_s n(\mathbf{r}))$. Therefore the exchange correlation functional of (3.44) contains the changing in the electron density too. φ in turn describes a spin scaling factor which is defined in the following equation:

$$\varphi(\xi) = [1 + \xi]^{\frac{2}{3}} + \frac{[1 - \xi]^{\frac{2}{3}}}{2} \quad (3.45)$$

k_s is the well known Fermi screening wavenumber which is a measure for the electrostatic screening like it was derived in the Thomas-Fermi model. This wavenumber can be written as $k_s = \sqrt{(4k_F/\pi a_0)}$. Perdew et. al. derived the correction function H from three different limiting cases [40].

The first one is the case in which the electron density is very slowly varying and therefore t will approach zero. In this case H can be written in terms of its second order expansion [40] and reads as follows:

$$H \rightarrow (e^2/a_0)\beta\varphi^3t^2 \quad (3.46)$$

In equation (3.46) β was determined as a numerical and dimensionless parameter which should read as 0.066725. The next limiting case which was considered is the very rapidly varying electron density which means that the dimensionless gradient tends to infinity ($t \rightarrow \infty$). In this case H tends to be just the negative of the correlation energy of the homogeneous electron gas $H \rightarrow -\epsilon_C^{hom}$. This means that the electron correlation vanishes, which can be seen if one considers equation (3.44). The third considered case was a high density limit for which the Wigner-Seitz radius tends to zero $r_s \rightarrow 0$. In this limit $\epsilon_C^{hom}(r_s, \xi) \rightarrow (e^2/a_0)\varphi^3[\gamma \ln(r_s) - \omega_0]$ where γ and ω are functions which in this limiting case can be written as $\gamma = (1 - \ln(2))/\pi^2$ and $\omega = 0.046644$ [40]. So in this case they wrote $H \rightarrow (e^2/a_0)\gamma\varphi^3 \ln(t^2)$ which is very similar to the first case (3.46). Now they had to find a simple ansatz which satisfies all these conditions yielding equations (3.47) and (3.48).

$$H = (e^2/a_0) \ln \left\{ \frac{\beta}{\gamma} t^2 \frac{1 + At^2}{1 + At^2 + A^2t^4} \right\} \quad (3.47)$$

$$A = \frac{\beta}{\gamma} \left[e^{\frac{-\epsilon_C^{hom}}{\gamma\varphi^3e^2/a_0}} - 1 \right]^{-1}. \quad (3.48)$$

This equation starts at e^2/a_0 (which is the ratio of the quadratic elementary charge and the Bohr radius) for $t = 0$ and grows monotonically to $-\epsilon_C^{hom}$ the correlation energy of the homogeneous electron gas. Another approach for the correlation effects would be a Quantum Monte Carlo method like in the case of the correlation energy in the local spin density approximation. Then one fits an analytic function to the statistical results of the Monte Carlo approach [33].

Now one is able to derive the exchange energy in a similar manner by considering equation (3.49) and also dealing with some limiting cases. In the limit of the uniform electron gas $F_X(0)$ has to equal 1 to recover the correct results of the Thomas Fermi model. Like we have already seen there should be a linear response in the limit of the LSD approximation and so as $s \rightarrow 0$ the enhancement factor should tend to $F_x(s) \rightarrow 1 + 0.21951s^2$:

$$E_X^{GGA} = \int d\mathbf{r} n(\mathbf{r}) \epsilon_X^{hom}(n(\mathbf{r}), F_X(s)). \quad (3.49)$$

As another boundary Perdew et. al. chose the Lieb-Oxford lower limit boundary [29] for the exchange potential [40] which can be seen in equation (3.50).

$$E_X[n_\uparrow, n_\downarrow] \geq -1.679e^2 \int d\mathbf{r} n^{\frac{4}{3}}. \quad (3.50)$$

Now one is able to write an enhancement factor which satisfies both conditions and reads as (3.51) where $\kappa = 0.804$ and $\mu = \beta(\pi^2/3)$:

$$F_X(s) = 1 + \kappa - \frac{\kappa}{1 + \mu s^2 / \kappa}. \quad (3.51)$$

The GGA potentials improve, for example, the atomization energies, structural energy differences, they expand (soften) bonds and they also improve the total energies. This potential should also improve the results for inhomogeneities compared with the local density approximation, because it takes the gradients of the electronic densities into account [40]. In the next and last section about the exchange and correlation potentials, I want to discuss the principles of the PBEsol potential which is an improvement of the here mentioned potential for solids.

3.4 Perdew-Burke-Ernzerhof revised for solids

This functional was used for the calculation of the dipole moments of the considered organic molecules which were considered in our simulations. Moreover this functional was also used in our ab-initio molecular dynamics simulations which will be described in the next section. Like we have seen in the last section (3.3) of the GGA potential there were made a lot of approximations and a big contribution of non empirical functional development [42].

In this section I want to show an alternative GGA potential which was especially developed for solids by Perdew et.al. [42]. First of all, one has to look closely what are the advantages and the disadvantages of the PBE method of the foregoing section. One well known problem of the PBE method is the overestimation of the lattice constants by about 1% and therefore also those properties which are strongly dependent on the lattice constants like the bulk moduli, phonon frequencies, magnetism and ferroelectricity are therefore underestimated [42]. Another problem is the determination of the surface energies which are already very low in LSDA, but even lower in the PBE approach [42].

It would be advantageous to find an approach that gets rid of these deficiencies. However, one problem when improving the GGA approximation. If one increases the dependency of the functional on the gradient then one improves atomization energies and also total energies, but lattice parameters worsen. On the other hand, if one decreases the gradient dependence of the functional then one improves the lattice constants and surface energies but this will worsen atomization energies and total energies [56][23][42].

Therefore, Perdew et. al. took the well known exchange energy of the PBE approach which can be seen in equation (3.52) in a general form. Then they started their approach by adjusting two parameters μ and s which can be seen in equation (3.54) which is known as the enhancement factor of the exchange energy [42]. This enhancement factor is written as a potential series where the first two terms are shown below:

$$E_X^{GGA}[n] = \int d\mathbf{r} e_X^{unif}(n(\mathbf{r})) F_X(s(\mathbf{r})) \quad (3.52)$$

$$F_X(s) = 1 + \mu s^2 + \dots \quad (s \rightarrow 0). \quad (3.53)$$

Now one has to discuss the different parameters. $n(\mathbf{r})$ denotes the electron density and e_X^{unif} denotes the exchange energy density of the jellium reference system. The parameter s is called the reduced density gradient which is dimensionless and should be adjusted in this method [42] to yield better results for solids like it was already mentioned. This parameter s can be written as $|\nabla n|/(2k_F n)$ where k_F denotes the Fermi wave vector which is well known and was already mentioned.

Now Perdew et. al. tried to find an appropriate value μ which describes the exchange energy in solids in a satisfactory manner. They started from the exchange energies of neutral atoms which should be described very well by the asymptotic behavior of $E_X = -0.2208Z^{5/3} - 0.196Z + ..$ where the first term was determined by LSDA and the second by the GGA method [42]. Thus the requirement for μ to describe the exchange energy of neutral atoms reads as $\mu \approx 2\mu_{GE}$. But as a consequence one has to contravene the gradient expansion [42] as it was reported in [41]. Now one has the following problem, if the gradient expansion for the exchange energy is written in the form $\mu = 2\mu_{GE}$ it violates the condition of the slowly varying electron density, although this improves atomization energies. So one can see that the gradient expansion is not perfect and is able to describe either one or the other case but not both at the same time [42]. But nevertheless the gradient expansion is very important for solids, and one has to find a value for μ which is suitable for the considered problem.

Now the correlation energy can be written as (3.54) where $\epsilon_C^{hom}(n)$ denotes the correlation energy of the homogeneous electron gas and β is a numerical coefficient. t denotes again a dimensionless density gradient which can be written as $|\nabla n|/[2k_{TF}n]$ and where k_{TF} is the Thomas-Fermi screening wave vector which can be written as $k_{TF} = \sqrt{4k_F/\pi}$. Equation (3.54) is also expressed as a power series and would be continued by a numerical factor and the third power of the dimensionless density gradient. For slowly varying electron gases β can be written as $\beta_{GE} = 0.0667$ which was proposed by [31][42]. There is also an equation which relates μ and β and reads as $\mu = \pi^2\beta/3$ [40].

$$E_C[n] = \int d\mathbf{r} n(\mathbf{r}) [\epsilon_C^{hom} n(\mathbf{r}) \beta t^2(\mathbf{r}) + ...] \quad (3.54)$$

But one is also able to consider neutral jellium clusters which are described in [5] and extract correlation energies for them. For these clusters the correlation energy can be written as $E_{XC} = e_{XC}^{hom}V + e_{XC}^{surf}A + ..$ where e_{XC}^{surf} denotes the exchange-correlation energy of the jellium surface and V and A denote the volume and the surface of the cluster, respectively. Now Perdew et. al. [42] tried to adapt the ϵ_{XC}^{surf} energy to their correlation functional. The problem was that the jellium surface energy is not known exactly and so they tested different methods relative to LSDA. The lower bound was made by PBE [12][13], then TPSS [47] and finally RPA+ [47]. The upper bound was made by the RPA like Pitarke Perdew potential [43]. Now they fitted the PBEsol potential to the curve of the TPSS [47] functional which seemed to satisfy the conditions of the jellium surface best [42].

Out of this calculations they choose the values for $\beta = 0.046$ and $\mu = \mu_{GE} = 10/81 = 0.1235$ which is in violation with equation $\mu = \beta\pi^2/3$.

Nevertheless, this exchange correlation functional should improve now surface effects compared to LSDA and GGA [42]. Moreover, if the considered solid will be compressed very strongly then this functional should become exact because their surfaces are slowly varying and the exchange then contribution dominates the correlation energy [42]. Last, one

is able to define $F_{XC}(\mathbf{r}_S, s(\mathbf{r}))$ by equation (3.55) where the high density limit is denoted by $r_s \rightarrow 0$ and then the functional is determined by the exchange contribution [42]:

$$E_{XC}^{PBEsol}[n] = \int d\mathbf{r} e_X^{hom} F_{XC}(\mathbf{r}_S, s(\mathbf{r})). \quad (3.55)$$

Finally, one is able to say that PBEsol will worsen atomization energies and total energies. However, it will be more appropriate for surface energies and also lattice constants will be determined in a satisfactory way. Because we want to use the ab initio molecular dynamics for the parametrization of the Monte Carlo code mentioned in section 4.3 we chose this method because we are interested in the lattice constants but also the correlation of dipoles with the cages and dipole- dipole correlations.

3.5 Generalized gradient approximation with included dispersion interactions

We would like to compare two different DFT approaches for the calculation of the perovskite system. One with and one without the inclusion of Van der Waals interactions. This section should give a principle overview of how such interactions will be included in a DFT approach. If one wants to include dispersion interactions one chooses a certain exchange correlation functional as a starting point which can in principle be any suitable LDA or GGA. In the current thesis this was the PBE method which was already described in section 3.3. We can rewrite the total energy of the system in the following way:

$$E_{\text{DFT-D}} = E_{\text{DFT}} + E_{\text{D}}. \quad (3.56)$$

Moreover, E_{DFT} denotes the energy which was calculated by the usual Kohn-Sham approach and E_{D} describes the interaction which arises due to the dispersion forces. The dispersion force is also known as London force and the energy which arises due to it behaves like R^{-6} where R is the distance between any two atoms. Now Grimme wrote the dispersion energy as follows [20]:

$$E_{\text{D}} = -s_6 \sum_{i=1}^{N_{\text{at}}-1} \sum_{j=i+1}^{N_{\text{at}}} \frac{C_{ij}^6}{R_{ij}^6} f_{\text{dmp}}(\mathbf{R}_{ij}), \quad (3.57)$$

where N_{at} denotes the number of atoms of the considered entity and C_{ij} is a coefficient which has to be determined for every atom pair. This coefficient can for example be calculated out of the polarizabilities of the considered atoms that form the interaction pairs. s_6 is a scaling factor which has to be determined according to the density functional one uses [20] and $f_{\text{dmp}}(\mathbf{R}_{ij})$ is the so called damping function. This function is very important because it determines the behavior of the dispersion correction in the near surroundings of certain atomic positions [21]. There exist different ways to express this damping function. Here the one which was introduced by Grimme [20] is shown:

$$f_{\text{damp}}(\mathbf{R}_{AB}) = \frac{1}{1 + e^{-\gamma \left(\frac{\mathbf{R}_{AB}}{s_{r,n} \mathbf{R}_0^{AB}} - 1 \right)}} \quad (3.58)$$

Here \mathbf{R}_0^{AB} can be considered as a cut off radius for a certain atom pair. This cut off can be different for different atom pairs. $s_{r,n}$ again is a scaling factor which depends

on the used energy functional. And last γ describes the steepness of the change of the damping function for small radii \mathbf{R}_{AB} [21]. One has to calculate a C_6^i value for every atom independently and then combining them with the formula for the geometric mean:

$$C_6^{ij} = \sqrt{C_6^i C_6^j}. \quad (3.59)$$

The individual C_6^a are calculated out of the ionization potentials I_p and dipole polarizabilities α which can be seen in the following relation [20]:

$$C_6^a = 0.05 N I_p^a \alpha^a. \quad (3.60)$$

N is an integer number and can take the values 2, 10, 18, 36, and 54 which is valid for atoms of the first five rows of the periodic table [20]. One can improve equation (3.57) by adding another term which can be written as follows:

$$E_D = -s_6 \sum_{i=1}^{N_{at}-1} \sum_{j=i+1}^{N_{at}} \frac{C_6^{ij}}{\mathbf{R}_{ij}^6} f_{dmp}(\mathbf{R}_{ij}) + \frac{C_8^{ij}}{\mathbf{R}_{ij}^8} f_{dmp}(\mathbf{R}_{ij}). \quad (3.61)$$

The additive \mathbf{R}_{ij}^8 term in equation (3.61) is used to improve the corrections to the energy due to dispersion interactions. The parameter C_8^{ij} is related to the other polarization constant C_6^{ij} via the cut off radius of a certain atom pair ($C_8^{ij} = (\mathbf{R}_0^{AB})^2 C_6^{ij}$). Moreover in the DFT-D3 method the coefficients C_6^{ij} is made geometry dependent. Therefore they have to be recalculated for every minimization step. This should improve the results because now the dispersion interaction is determined by the geometry of the system and not only out of a standard reference system (usually an isolated atom).

3.6 Molecular Dynamics

So in the foregoing sections a description of the Born- Oppenheimer approximation [6] the DFT method [24][51] and also the used PBEsol [42] potential was shown. We now have all ingredients needed for doing ab- initio molecular dynamics simulations except for the propagation algorithm for the nuclei which will be described in this section. For the propagation of the ions we need the force acting on this certain ion. Therefore, one has to write down the energy contributions which are important. The next equation shows the contribution to the total energy which arises due to the electrons within the Born Oppenheimer approximation i.e with the nuclei held at fixed positions:

$$\left[\hat{T}_e + \hat{V}_{ee} + \hat{V}_{eN} \right] \Psi(\mathbf{x}, \mathbf{X}) = \epsilon(\mathbf{X}) \Psi(\mathbf{x}, \mathbf{X}). \quad (3.62)$$

The coordinates \mathbf{x} denote all the electronic coordinates ($\mathbf{x} \equiv \mathbf{r}_1, \mathbf{r}_2, \mathbf{r}_3, \dots, \mathbf{r}_{N_e}$) and \mathbf{X} denotes all the nuclear coordinates ($\mathbf{X} \equiv \mathbf{R}_1, \mathbf{R}_2, \mathbf{R}_3, \dots, \mathbf{R}_{N_N}$). Next one introduces the total energy which is just the sum of the electronic energy and the nuclear repulsion. This can be seen in the following equation:

$$E_{\text{tot}} = \epsilon(\mathbf{X}) + V_{NN}(\mathbf{X}). \quad (3.63)$$

The calculation of the force acting on a certain nuclei is described as follows:

$$\mathbf{F}_i = -\nabla_i E_{\text{tot}} = -\nabla_i [\epsilon(\mathbf{X}) + V_{NN}(\mathbf{X})] \quad (3.64)$$

The symbol ∇_i denotes that the operator is only acting on the coordinates of the i^{th} nuclei (\mathbf{R}_i). For the calculation of the derivative with respect to electronic energy contribution one is able to use the Hellmann-Feynmann theorem which is written as [33]:

$$\nabla_i \epsilon(\mathbf{X}) = \langle \Psi | \nabla_i \hat{H}(\mathbf{X}) | \Psi \rangle \quad (3.65)$$

This is true for any hermitian operator acting on an ortho-normalized wavefunction. To maintain the temperature at a constant value we use the Langevin thermostat [36] where additional forces are added to those caused by the internal potential shown in equation (3.64). The net force acting on a certain nuclei is shown in the next equation [36]:

$$\dot{\mathbf{p}}_i = \mathbf{F}_i + \gamma_i \mathbf{p}_i + \mathbf{f}_i. \quad (3.66)$$

In that equation $\dot{\mathbf{p}}$ denotes the derivative of momentum with respect to time, γ_i denotes the friction coefficient of atomic species i and \mathbf{f}_i is an additional random force which is added to maintain the temperature within the threshold values. The friction coefficient and the variance of the random force are related by the following equation:

$$\sigma_i^2 = \frac{2m_i \gamma_i k_b T}{\Delta t}. \quad (3.67)$$

Δt denotes the time step of the molecular dynamics simulation, k_b Boltzmann's constant, m_i is the mass of the considered ion and σ_i^2 is the variance of the random force distribution. Note, with increasing temperature the distribution of the random force which is centered around 0 gets broader and therefore forces with higher magnitude are permitted. On the other hand with increasing time step the distribution gets narrower and therefore smaller random forces are applied because otherwise the jumps of the ions will be too big.

Last we need an appropriate integration algorithm like Verlet or a Runge-Kutta method. The ab-initio molecular dynamics simulations in this thesis were carried out with the Verlet algorithm [48][25]. The Verlet algorithm is derived by describing the position of the foregoing $n - 1$ and the following time step $n + 1$ as a Taylor expansion. Then taking the sum of the two series and doing little algebra yields a stable algorithm for the propagation of the ions which is shown in this equation:

$$\mathbf{R}_i^{n+1} = (2\mathbf{R}_i^n - \mathbf{R}_i^{n-1}) + \ddot{\mathbf{R}}_i^n \Delta t^2. \quad (3.68)$$

The superscripts in this equation denote the time steps and the subscripts denote the propagated ion. Note that the acceleration of the considered ion is calculated out of equation (3.66) as $\ddot{\mathbf{R}}_i^n = \dot{\mathbf{p}}_i / m_i$. With equation (3.68) one has now a very suitable algorithm for ab initio molecular dynamics. This technique was used in this thesis to determine the dynamics of the atoms.

3.7 Monte Carlo Metropolis-Rosenbluth algorithm

For our Monte Carlo approach we used the Metropolis-Rosenbluth algorithm which was invented in 1953 [37][35]. In this algorithms one chooses a starting configuration and out of this one determines new configuration under the use of a transition probability [35]. The probability of the n^{th} configuration is given by:

$$P_n = \frac{e^{-\frac{E_n}{k_b T}}}{Z}. \quad (3.69)$$

In this equation E_n denotes the energy of the n^{th} configuration, k_b is Boltzmann's constant, T is the absolute temperature and Z is the partition function which is usually unknown. Therefore the probability of a certain state is unknown too. Like already mentioned one always generates the new state out of the foregoing state which can be considered as a Markov chain [35]. Now one is able to calculate a transition probability for the transition from the state n to state m by dividing the probabilities of the corresponding states. This can be seen in the next relation,

$$\frac{P_m}{P_n} = e^{\frac{-E_n - E_m}{k_B T}} = e^{-\frac{\Delta E}{k_B T}}. \quad (3.70)$$

E_n and E_m describe the energies of the considered states and $\Delta E = E_n - E_m$. So one is able to calculate the transition probability from configuration n to m . If the change in energy is negative the new configuration is accepted automatically. If the step is endothermic i.e. the difference in energy is positive then one chooses a random number. This random number has to be within the interval $[0, 1]$. It is very important that the random numbers are uncorrelated [37][35]. The condition for an endothermic step to be accepted is shown in the following relation:

$$r < e^{-\frac{\Delta E}{k_B T}}. \quad (3.71)$$

r denotes the uniformly chosen random number. The scheme below shows the here presented Monte Carlo procedure.

1. Choose initial configuration (can be a random configuration)
2. Calculate energy of this configuration
3. Choose a site of the lattice
4. Calculate the energy of the configuration with the changed chosen site
5. Calculate Boltzmann factor shown in equation (3.71)
6. Accept new configuration if step is exothermic otherwise use relation (3.71) to test if structure new configuration is taken
7. Begin procedure at step 3

The Metropolis-Rosenbluth algorithm can now be used for minimization problems like the geometry optimization of a physical system.

4 Computational Details

4.1 Considered Organo-Halide Perovskite Systems

The system which will be considered in this thesis is the methylammonium lead iodide system. The structure is built up of lead and iodine atoms which form the perovskite structure. In the cubic cavities of this perovskite structure methylammonium ions are inserted. This is schematically represented in figure 4.1. The methylammonium molecules deliver one electron the perovskite framework and therefore the cage is negatively charged

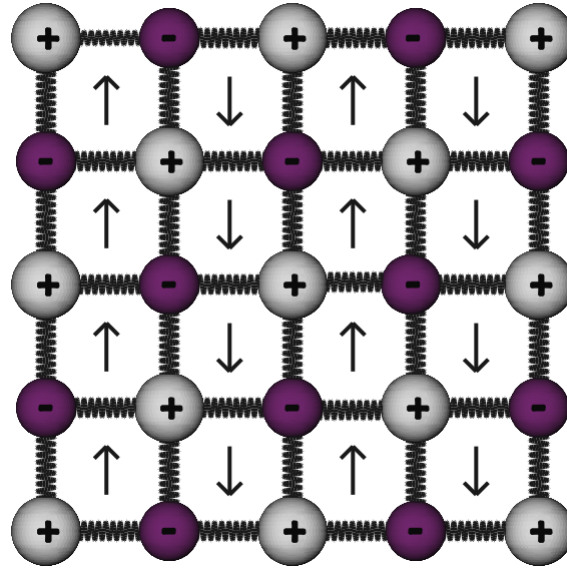


Figure 4.1: Schematic representation of $4 \times 4 \times 4$ organo-halide perovskite system (lead atoms grey, iodine atoms purple)

and the methylammonium exists in its cationic state. Therefore the cage is in total negatively charged. Next the methylammonium ion possesses a permanent dipole molecule which arises due to the different electro-negativities of the carbon and the nitrogen atoms. According to the Pauling electronegativity, carbon possesses a electro-negativity of 2.55 and nitrogen of 3.04. It follows, the electron cloud will be shifted to the nitrogen atom which results in a permanent dipole moment. The dipole vector of this species is directing from the carbon atom to the nitrogen atom. This is the reason why the organic molecules are represented as arrows (figure 4.1) which represent the dipole vectors of the molecules. The inorganic framework too consists of atoms with different electro-negativities which also causes a net dipole moment. The electronegativity of lead reads as 1.87 and the one of iodine is written as 2.66 according to Pauling's scale too and hence the dipole vector will be oriented from the lead atom towards the iodine atom. For an ideal cubic structure the net dipole moment which is the sum of the single dipole vectors of the whole system cancel which is a reason of the cubic symmetry. Because the charge is not equally distributed over the iodine and lead atoms we will consider the lead atoms as positively charged and the iodine atoms as negatively charged. This is the reason for the plus and minus signs on top of the lead and iodine atoms in figure 4.1. The forces which bind the lead and iodine atoms are represented by springs. The reason for this is the inorganic framework spanned by the iodine and lead atoms is in principle rigid. There exists only thermal motion which causes the atoms of the perovskite framework to fluctuate around their equilibrium positions. This thermal vibrations can be approximated as harmonic oscillators which is the reason for using springs as a representation for the binding forces between the iodine and lead atoms. The lattice parameters for the ab-initio simulations shown in the next chapters are gained from X-ray diffraction experiments carried out by Stoumpos et. al. The parameters read as $\mathbf{a} = \mathbf{b} = 6.3115\text{\AA}$ and $\mathbf{c} = 6.3161\text{\AA}$. Therefore, the cubic symmetry is distorted and hence if one looks closely the system will be tetragonal. Because the deviation from the cubic symmetry is very low we will consider the system as cubic during this thesis.

4.2 Ab-initio Molecular Dynamics Simulation

To execute the ab-initio molecular dynamics simulation we used Langevin dynamics which were already described in section 3.6. To do this one has to set the MDALGO tag to 3 (MDALGO=3) in the VASP INCAR file. For the friction coefficient which occurs in the Langevin dynamics (see equations (3.66) and (3.67)) [36] we used a value of 60 which is defined by the LANGEVIN_GAMMA tag in vasp. The ionic positions were updated under the use of a Verlet algorithm which is done by setting the IBRION tag to zero. The temperature of the ab-initio molecular dynamics simulation is defined by the tags TEBEG and TEEND which define the upper and the lower temperature bound respectively. Both values were set to 300K. The last parameter which is very important for the molecular dynamics simulation is the used time step which will be defined by the POTIM tag. For the time step we used 3fs for the bigger $6 \times 6 \times 6$ simulation and 2fs for both $4 \times 4 \times 4$ simulations. The bigger time step in the $6 \times 6 \times 6$ simulation originates from the heavier hydrogen masses which were used. The hydrogen masses were set to 4a.u. in the case of the $4 \times 4 \times 4$ simulations and to 6a.u. for the $6 \times 6 \times 6$ simulations. The different hydrogen masses will not influence the results presented in this thesis which will be shown in section 5.2.8 in detail.

Next one has to define how VASP minimizes the electronic structure for every molecular dynamics time step. Therefore one first chooses an appropriate potential for the exchange correlation contribution where we used the PBEsol potential which was described in section 3.4. Now one defines an energy cut off which defines the number of plane waves which are taken for the plane wave basis of VASP. This is done with the ENMAX tag which was adjusted to 250meV. In a solid the different states are occupied according to the Fermi-Dirac distribution which would be a step function. If one would take this step function the states would not be variational and therefore one would get no forces. This is the reason why one uses Gaussian smearing which is done by setting the ISMEAR tag to zero. The SIGMA tag now defines the width of the Gaussian function and was set to 0.05. For the stopping criterion of the electronic minimization we used an energy difference of 0.001meV which is done by the EDIFF tag. To give VASP a minimum number of electronic minimization steps which will be carried out for every molecular dynamics step one is able to use the NELMIN tag which was adjusted to 5 in the here shown simulations. Last it should be mentioned the calculations were performed with the Γ point only version of VASP which means there was only a single k point used, namely the Γ point. This is acceptable since large supercells were used.

4.3 Monte Carlo approach

To study the behaviour of the organic molecules which are located in the cubic cages of the PbI_3 framework we used a Monte Carlo Metropolis approach [37]. Especially we were interested in the relative orientation of molecules. Because out of this one is able to determine if the organo-halide perovskite has ferroelectric or anti-ferroelectric domains (or any other ordering structure) or if there is no ordering at least and the properties of the system are at least determined by the inorganic framework. By the parametrization of the Monte Carlo approach one is able to determine the importance of the different interactions. But this will be discussed later in more detail. Moreover, with the Monte Carlo approach one is able to calculate very big systems and hence one is able to exclude size effects on the ordering behaviour of the considered molecules.

Before starting we made some assumptions to make the calculations as easy and fast as

possible. The organic molecules which are taken for organo-halide perovskite systems possess a permanent dipole moment and therefore we included dipole-dipole interactions in the model Hamiltonian. The dipole-dipole interactions were described as point dipole interactions. This approximation is shown in figures 4.2 and 4.3. Like one is able to see the electrostatic fields of the point dipole and the dipole differ if one is very close to them but at larger distances the two fields become the same and therefore their interaction energies.

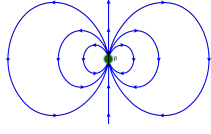


Figure 4.2: Electrical field of a point dipole [1]

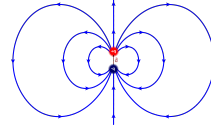


Figure 4.3: \vec{E} field of a physical dipole [1]

The organic molecules transfer one electron to the inorganic framework and therefore they are positively charged. It follows, there is electrostatic repulsion between neighbouring molecules. This contribution is neglected in the Hamiltonian because this would only influence the distance between the organic molecules and not their relative orientations. The molecules are locked inside the inorganic framework formed by the PbI_3 units and therefore they are not able to move except of fluctuations around their equilibrium position. This results in our next approximation, we kept the positions of the dipoles fixed in the Monte Carlo approach and therefore neglected the fluctuations in position because they will not influence the relative orientations of the dipoles. The next assumption we needed was the mean field approach. Therefore the energy of a certain molecule is determined by its orientation and the electrostatic field which arises due to the neighbouring dipoles. Last we have to take into account the interactions of the dipoles with the inorganic framework which we will do implicitly by adding interaction terms to the Hamiltonian. These terms will be gained out of ab-initio molecular dynamics simulations. As a result starting Hamiltonian which was chosen can be written as:

$$\hat{H} = \sum_{i, E\text{-field}}^N (\mathbf{p}_i \cdot \mathbf{E}_0) + \sum_{i,j}^{N,M} \left(\frac{\mathbf{p}_i \cdot \mathbf{p}_j}{r^3} - \frac{(\hat{\mathbf{n}} \cdot \mathbf{p}_i)(\hat{\mathbf{n}} \cdot \mathbf{p}_j)}{r^3} \right) + \text{cage interactions}. \quad (4.1)$$

In this equation \mathbf{E}_0 denotes an applied electric field, \mathbf{p} denote the dipole vectors, $\hat{\mathbf{n}}$ describes a unit vector which connects the considered dipole pair and r is the distance between the considered dipole pair. The first term describes the interaction energy of a certain dipole with an applied electric field. The second term describes the point dipole point dipole interaction [19] energy and last we have to include the dipole interaction energy with the atoms of the inorganic framework. This will be shown in section 5.4. Moreover, from this equation it can be seen the nature of the organic molecule or more clearly the dipole species in this formulae is just determined by the dipole vector. Therefore the choice of the dipole vector determines which organic molecule is located inside the PbI_3 framework. Frost et. al. used a very similar Hamiltonian for their Monte Carlo approach which is shown in the following equation [28]:

$$\hat{H} = \sum_{i, E\text{-field}}^N (\mathbf{p}_i \cdot \mathbf{E}_0) + \sum_{i,j}^{N,M} \left(\frac{\mathbf{p}_i \cdot \mathbf{p}_j}{r^3} - \frac{(\hat{\mathbf{n}} \cdot \mathbf{p}_i)(\hat{\mathbf{n}} \cdot \mathbf{p}_j)}{r^3} \right) + \sum_{i, \text{strain}}^N K(\hat{\mathbf{p}}_i \cdot \hat{\mathbf{p}}_j). \quad (4.2)$$

Like one can see they describe the interaction with the electric field and the dipole-dipole interaction in an ordinary way. But Frost et. al. added a third linear term which should describe the interactions of two dipoles locked in neighbouring cages.

If one has the correct terms for the cage interactions for the Hamiltonian shown in equation (4.1) one is able to find the minimum configuration of the considered system by the use of the Metropolis-Rosenbluth algorithm shown in section 3.7.

Now we had to write a Monte Carlo code for which we determine the cage interaction terms like shown in the schematic Hamiltonian (4.1) by comparing the results of this code with ab-initio molecular dynamics simulations. The used code was written in *FORTRAN90*. The next lines should show the main parts of this code and how it works in principal. First the code generate a desired number of grid points and on every grid point there will be a randomly oriented dipole. Then the code determines a list which contains the interaction partners for every dipole and simultaneously a distance list is calculated. Like already mentioned the positions of the dipoles will be kept fixed and therefore also the distances. So this distance list has the same shape as the interaction partner list but contains the distances between the two interaction partners. Then the energy of the initial configuration is calculated which is done in accordance with equation (4.1). The next step is a simulated annealing procedure. Therefore one starts at a higher temperature as the one for which one is looking for the minimum configuration. So in the beginning of the minimization there are a lot of accessible structures because the temperature is high. Then one cooles the system slowly to the desired temperature to find the global minimum. This procedure is a trick not to get trapped in local minima so easily. The shape of the temperature curve does not effect the results in general [27][9].

Last the program contains a very special energy calculation for each minimization step. Beacuse in every single minimization step only one dipole changes its orientation it is sufficient to only update the energy terms where this dipole is involved. The energy field was build in a way that it has two entries for the interaction energy of every dipole pair. One entry belongs to the interaction a-b and one to the interaction energy of b-a. For this we determined a list which contains the positions of the energy field that have to be updated if the orientation of a certain dipole was changed. The loop which does this energy calculation was finally parallelized with OPENMP to make the code even faster. The result of this was a Monte Carlo code which relaxes the orientation of dipoles on a fixed grid with a model Hamiltonian which only contained the dipole-dipole interactions and the dipole interaction with an applied electric field. The next step is now to determine the terms which will describe the interactions of the dipoles with the inorganic framework.

5 Results

5.1 Dipole moments of organic molecules

The intrinsic dipole moments of the organic CH_3NH_3 molecules were to our knowledge always taken as those from the neutral organic species. But in the perovskite cells one deals with the organic cation and therefore one should take into account the dipole moment of the cation. We calculated the dipole moments of two species. The methylammonium molecule like it was used in our simulation and the formamidine molecule. For the calculation we compared two approaches for the neutral species. One time, we applied a dipole layer with the LDIPOL tag, and in the other case, we performed the calculation without this dipole layer. This layer is applied to avoid self-interaction energies. The dipoles were

positioned in the cell to have the net dipole moment only in one special direction of space. From this it follows we only had to calculate the dipole moment in this certain direction which was carried out by the IDIPOL tag. The next important thing to consider was the system size and hence we performed several calculations with increasing cell sizes. Finally we extrapolated the dipole moments to infinitely large cells because in this case we will not have any self interactions of the dipoles with their periodic images left. The extrapolated values were the same for the calculations with and without the applied dipole correction layer. The results are summarized in table 1. The values for the neutral molecules from table 1 coincide very well with those published by Frost et. al. They reported a value of 2.29D for the methyl- ammonium and 0.21D for the formamidinium.

Table 1: Dipole moments

species	dipole vector \mathbf{p} in [$e^*\text{\AA}$]	$ \mathbf{p} $ in [$e^*\text{\AA}$]	$ \mathbf{p} $ in [D]
CH_3NH_2	$[-0.110530, 0.439401, 0.107614]$	0.465694	2.236821
HNCHNH_2	$[-0.015979, 0.007990, 0.033563]$	0.038022	0.182629

We also tried calculating the dipole moment of the ions but this turned out to be a very complicated procedure. The reason for this is the resulting dipole moment of the charged species depends on the choice of the origin of the taken super cell. We think this has something to do with the applied background charge which VASP adds to the considered super cell. We were not able to deal with this problem and this is the reason for the following calculations to be performed with the neutral molecule's dipole moment. Figure 5.1 shows the inhomogeneous electron distribution of methyl-ammonium ion. Like one can see the colour changes from blue, green over yellow to red which is associated with an increase in the electron density. The carbon atom is located at the green ellipse at the left part of the figure and the nitrogen is situated at the red spot in the figure. Therefore the charge density is higher around the nitrogen atom than it is around the carbon atom. The origin for this behaviour is the higher electro-negativity of the nitrogen atom compared to the carbon atom. This behaviour will have an influence on the interaction of the negatively charged framework which possesses a dipole moment too and the organic cations which are locked inside it. The dipole moment of the PbI_3 framework also arises due to the different electro-negativities of the involved atoms. The lead atoms are more electro-positive than the iodine atoms and as a result the electrons will be more likely located around the iodine atoms. This results in a permanent dipole moment. The dipole-dipole interactions should play a significant role in this system and the resulting effects will be discussed in more detail in section 5.2.3

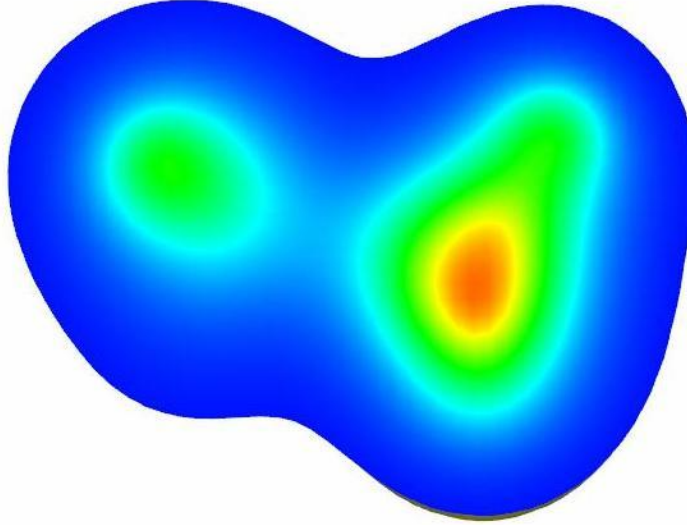


Figure 5.1: Electron charge density of a methylammonium cation (nitrogen on right side)

5.2 Molecular Dynamics

5.2.1 Heat capacity from of ab-initio molecular dynamics simulations

We have calculated the heat capacities out of the variance of the energy fluctuations. The heat capacity is defined as:

$$c_V = \frac{\delta E^2}{k_B T^2}, \quad (5.1)$$

where δE^2 denotes the variance of the energy in time, k_B the Boltzmann constant and T is the absolute temperature. The subscript V in c_V denotes that this value describes the heat capacity at constant volume. This originates from our simulation conditions which were done in the canonical ensemble and therefore the volume was kept constant. To calculate the heat capacity with equation 5.1 we first determined the variation of our energy curve. Next the variance of the energy was normalized to a single unit cell by division through the number of cells present in the simulated system. Next we specified the number of mols present in a single unit cell which reads as $1.6605e^{-24} \frac{\text{mol}}{\text{unit cell}}$. From this we determined the heat capacity per mole for the considered perovskite system, as presented in table 2.

The heat capacities in table 2 are all around $300 \frac{\text{J}}{\text{mol} \cdot \text{K}}$ except of the $2 \times 2 \times 2$ system which was calculated with the PBEsol potential and included dispersion interaction. For comparison the heat capacity of a monoatomic classical gas reads as $12.5 \frac{\text{J}}{\text{mol} \cdot \text{K}}$ according to the equipartition theorem for the heat capacity shown in the next equation:

$$C_{V,\text{mol}} = \frac{f}{2} * R, \quad (5.2)$$

where R denotes the ideal gas constant and f are the degrees of freedom which enter quadratically into the Hamilton function. As argued before the additional dispersion interaction will apply an extra constraint to the motion of the dipole. Therefore the rotation barrier of the dipole is higher from which follows the organic molecule will be confined longer to certain regions during the simulation. While locked to a certain orientation the

CH_3NH_3^+ ion will wobble around this position and as a result some of the degrees of freedom of the molecule will be frozen during this process. The difference in the number of degrees of freedom can be estimated according to the following relation:

$$\frac{fC_{V,\text{mol,perovskite}}}{C_{V,\text{mol,classical-gas}}} = N, \quad (5.3)$$

where N denotes the number of degrees of freedom in the perovskite system, $C_{V,\text{mol,perovskite}}$ which is the molar heat capacity at constant volume for the perovskite, $C_{V,\text{mol,classical-gas}}$ is the molar heat capacity at constant volume of a monoatomic classical ideal gas and f denotes the number of degrees of freedom of the classical gas which can be written as 3. With equation (5.3) one is able to determine the number of degrees of freedom for the considered perovskite system. The ratios $\frac{C_{V,\text{mol,perovskite}}}{C_{V,\text{mol,classical-gas}}}$ can be seen in table 2 in the last column. If one follows this procedure one gains approximately $N = 73$ for the $2 \times 2 \times 2$ system calculated with the PBEsol potential and roughly $N = 59$ for the simulation with included dispersion interactions. It follows there are around 13 degrees of freedom frozen when comparing the PBEsol potential with the PBEsol potential with included dispersion interaction. Nevertheless the dipole is able to overcome this rotational barriers and will be able to even make full rotations in the cell. However in sum, the variance in the energy will be lower and it follows the heat capacity will also be less than in the case of the PBEsol potential were the rotational barrier is lower and the organic molecule is more flexible. The heat capacity of the $6 \times 6 \times 6$ structure shows a slightly higher heat capacity. This is a result of the much fewer steps which are available for this structure (2440). On the one hand, one has to use a satisfactory large time interval for calculating an appropriate variance of the energy vs time curve and on the other hand, one has to chose a preferably long equilibration time intervall. This was hard to realize for this simulation and therefore it follows the variance of the energy vs time curve depends stronger on the starting step from where one begins with the sampling procedure. The more data points the more independent the variance will be on the starting step. The starting step was chosen for all simulations in a way that there is enough time for energy equilibration of the considered system. Cause of division by the before mentioned number of mols which are contained in a single unit cell small deviations in the variance will result in variations of the heat capacity like they can be seen in table 2. There is no special reason why the value of the $6 \times 6 \times 6$ cell should be slightly higher than the other values besides insufficient equilibration time and bad statistics.

Table 2: Heat capacities

system name	system size	heat capacity [$\frac{J}{molK}$]	$\frac{C_{V,mol,perovskite}}{C_{V,mol,classical-gas}}$
1x1x1	1	303.2	24.3
2x2x2 PBEsol	8	301.3	24.2
2x2x2 PBEsol+dispersion interaction	8	245.4	19.7
4x4x4- aligned	64	304.9	24.4
4x4x4- random	64	303.6	24.3
6x6x6	216	312.4	25.1

5.2.2 Autocorrelation functions of ab-initio molecular dynamics

In this section, we will show how the system size correlates with the relaxation time and also how the two different potentials will affect this behaviour. The autocorrelation function will be a measure of how much a certain structure (or geometry of a certain time step) will differ from the initial geometry. It is also possible to not choose the initial geometry for comparison but any other reference structure of the simulation at any chosen time step. If one chooses the initial structure to compare with, the autocorrelation function will have its maximum at the beginning and the more the geometry will differ from the initial the lower the autocorrelation function will become. The autocorrelation functions show a exponentially decaying behaviour as will be shown later on. In this thesis we used the following autocorrelation function:

$$r(t) = \langle \hat{\mathbf{p}}(0) \bullet \hat{\mathbf{p}}(t) \rangle, \quad (5.4)$$

where the vectors $\hat{\mathbf{p}}(0)$ and $\hat{\mathbf{p}}(t)$ denote the dipole vectors at $t = 0$ and at time step t . Therefore, the autocorrelation functions will be calculated by comparing the dot product of the initial structure with a structure at time step t . This can be seen in equation 5.4 and the brackets denote a mean over all dipoles. If the actual structure matches the initial one perfectly this results in a value of one. The more the two structures differ from each other the more the dot product will approach zero. For the smaller systems this curves were very jagged and therefore we determined the following autocorrelation function to improve statistics:

$$r(\tau) = \langle \hat{\mathbf{p}}(\tau) \bullet \hat{\mathbf{p}}(\tau, t) \rangle. \quad (5.5)$$

Here $\hat{\mathbf{p}}(\tau)$ denotes the initially chosen geometry and $\hat{\mathbf{p}}(\tau, t)$ denotes the values of the time signal following after the delay time τ . Therefore, equation (5.5) represents the correlation of the time signal lagged by a time of τ with itself. Hence τ denotes the time which has elapsed from the beginning of the simulation to the time step for which one starts to calculate the autocorrelation functions. In formula (5.5) the brackets denote the average over the dipoles of the whole cell but also an averaging over all the different time steps t following after the delay time τ . For this curve the same is true as for the autocorrelation function of equation (5.4). But with relation (5.5) one not only calculates the mean over the dipoles in the considered system but also a mean over all the different delay times what improves statistics and therefore results in smoother autocorrelation functions. Values equal one denote perfect agreement with the initial structure and the smaller the value the bigger the deviation from the starting structure. These functions

are therefore a measure for the relaxation of the system and by fitting an exponential function to the autocorrelation function one is able to determine the characteristic time of the exponential decay. The characteristic time of an exponential is the time at which the function decayed to a value of e^{-1} . To determine this time one has to gain the coefficient T in the function $e^{-\frac{t}{T}}$ which denotes the characteristic time. The characteristic times for different system sizes and starting structures are shown in table 3 and the corresponding autocorrelation functions are given in figure 5.2.

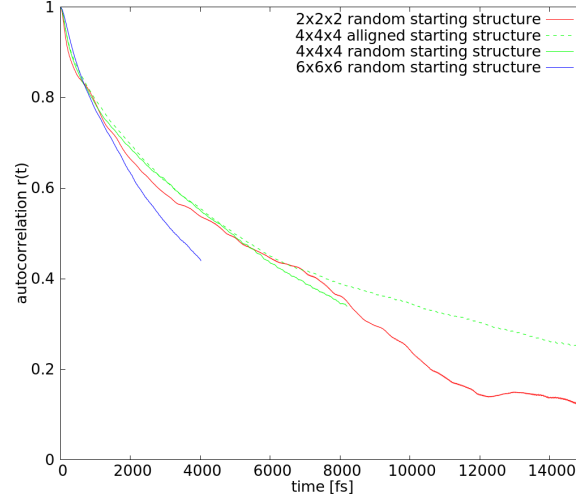


Figure 5.2: Autocorrelation functions of different systems sizes and starting structures

Table 3: Relaxation times

system size	T in [ps]
2x2x2 random PBEsol	6.9
2x2x2 random PBEsol + dispersion interaction	22.1
4x4x4 aligned PBEsol	8.7
4x4x4 random PBEsol	6.8
6x6x6 random PBEsol	4.5

But when considering these values one should mention the exponential function describes the behaviour of the self correlation functions only rather approximately, if a single coefficient is used. Either one is able to fit the behaviour in the beginning with a satisfactory precision or at the end of the function. But one is in principle not able to describe the whole relaxation with a single exponential function in a satisfactory range. Nevertheless we fitted the exponential functions to the whole curve to gain a mean characteristic time since our present calculations are too short to deduce the long time behaviour accurately. In figure 5.3 one is able to see the exponential function is not able to describe the decay for the curve with included dispersion interactions. But in this figure it looks like the exponential function would describe the autocorrelation function for the simulations without included dispersion interactions in a satisfactory way. But this is only coincidence for the $2 \times 2 \times 2$ structure calculated with the PBEsol potential. We examined the accordance of the exponential function and the gained autocorrelation functions for the larger systems too, where the exponential approach is not able to give satisfactory results. But nevertheless, the characteristic time of the fitted exponentials is nice to get a feeling how the

different systems relax. Now looking at the characteristic times for the $4 \times 4 \times 4$ systems. We see T is nearly the same for the random and the aligned starting structure. They differ only by 1.9ps which is very little because we used a single parameter exponential function for the curve fitting and therefore by reasons of statistics these two values can be regarded as the same. Nevertheless if one considers the two curves for the $4 \times 4 \times 4$ geometries they start differing at about 5ps. So the long range correlation is smaller in the case with the aligned starting structure. So the random starting structure will be a better guess for the initial geometry. Next if one compares the characteristic times of the different systems sizes but only those calculated with the PBEsol potential one can see the aligned starting structure of the $4 \times 4 \times 4$ systems has the highest value T . This again indicates that the random starting structures will be a better starting point. The systems with random starting structures show a slight decrease of T from $2 \times 2 \times 2$ to $6 \times 6 \times 6$. The deviation of those values is again very low and is therefore not considered as insignificant. If one looks at the red curve in figure 5.2 which indicates the $2 \times 2 \times 2$ system one is able to see this graph reaches a plateau value at around 12ps where the autocorrelation remains at a certain value. This is interpreted as there is self correlation throughout the whole simulation, with the initial structure. For the simulations of the larger systems it can not yet be seen if there exists such a plateau value too because the simulation times are too short until now. The $2 \times 2 \times 2$ unit cell which was calculated with included dispersion interactions relaxes the slowest which is denoted by the high value of τ shown in table 3. Figure 5.3 shows exponential functions which were fitted to the data of $2 \times 2 \times 2$ which were calculated with two different potentials. The vertical lines in the plot denote the characteristic times of the exponential functions. These times are very often used as a measure for the relaxation of a system. But this has to be done very carefully because one is able to see the system is still correlated with the initial structures at these times (figure 5.3).

Now we want to compare the autocorrelation functions of the PBEsol potential and the Grimme potential. This is done for the $2 \times 2 \times 2$ cells. From the results for the characteristic times one would expect the autocorrelation function should decay slower in the case of the Grimme potential because the dipole should not be as flexible as for the PBEsol potential. As it is shown in figure 5.3 the structure with included dispersion interactions relaxes slower than the one which is calculated with the PBEsol functional. The slower relaxation of the system is understandable if one thinks of the dispersion interaction as an additional contribution which hinders the dipoles at leaving their positions. This caused by the attractive nature of this additional interaction contribution which cause the dipoles stick to their inorganic framework. These dispersion interactions are additional to the interactions described by the PBEsol functional. The inorganic framework is negatively charged it carries an additional electron which will be confined less to a certain region because it is shielded by the other electrons present on the Pb and I atoms. As a result this, electron should be highly polarizable. Next one has the positive charged organic ion in the center of the PbI_3 cages which will influence the inorganic framework by polarizing it. Therefore the dispersion interaction should play an important role when considering organohalide perovskite systems. But one has to be very careful to find an appropriate description of the VdW interaction to describe the behaviour of the cell correctly. This will be discussed in section 5.2.5. Moreover the self- correlation function of the simulation with the included dispersion interaction decays with a certain rate in the beginning but with increasing simulation time the curve gets essentially constant. The $2 \times 2 \times 2$ system simulated without dispersion interactions shows a similar behaviour although it is not so

pronounced. As a result it is very difficult to get structures which won't correlate with the initial one any more.

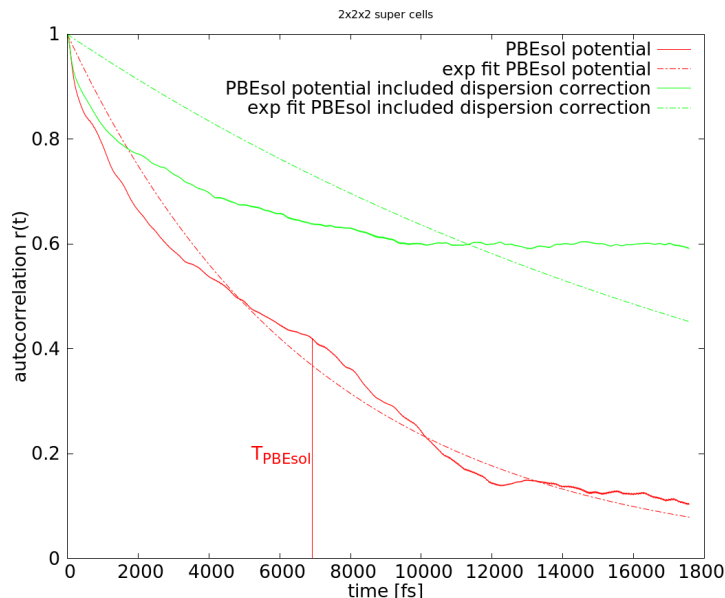


Figure 5.3: Comparing self- correlation of 2x2x2 PBEsol with 2x2x2 PBEsol+dispersion interaction and the corresponding exponential fit functions

5.2.3 Comparing $CH_3NH_3^+$ orientations for different starting structures and system sizes

In this section the orientation of dipoles will be discussed. We choose a spherical coordinate system like it can be seen in figure 5.4. In this figure the convention for of the angles as used in all the following polar plots is shown. φ is the angle in the \mathbf{xy} plane and is called the azimuthal angle. The interval for the azimuthal angle $[0, 2\pi]$, corresponds to a complete rotation in the \mathbf{xy} plane. It is defined in a way that $\varphi = 0$ denote the direction of the positive \mathbf{x} - axis. $\varphi = \frac{\pi}{4}$ denotes the alignment to the positive \mathbf{y} - axis, $\varphi = \frac{\pi}{2}$ the negative \mathbf{x} - axis, and $\varphi = \frac{3\pi}{4}$ the negative \mathbf{y} - axis respectively. θ is the angle between the \mathbf{z} axes and the considered vector. This angle is also called the polar angle of the spherical coordinate system. θ was chosen in a way that it spans $[0, \pi]$. The 0 angle denotes perfect alignment with the \mathbf{z} axes and π describes antialignment with the \mathbf{z} axes and hence an angle θ of $\frac{\pi}{2}$ describes a vector in the \mathbf{xy} plane. The distance of the vector from the origin is denoted by r . Because we are not interested in the distance of the organic molecules from the origin but only in their orientations we are able to neglect this coordinate in the following plots. As a results we are able to map a three dimensional problem into a two dimensional map. This is how all the following polar plots are built up. All angles which will be mentioned in the following sections will be based on this description and on figure 5.4. It is very important to mention that all the plots which will be shown in this work have a sinus correction in the spherical angle θ included to conserve the area of the individual bins. This behaviour can be derived very easily by derivating the surface of a sphere in spherical coordinates where one gets a sinusoidal dependence of the area element on the spherical angle θ .

First we will show the polar plots of the starting configurations to discuss which effects could be a bias of the initial structure and which effects really originate from the

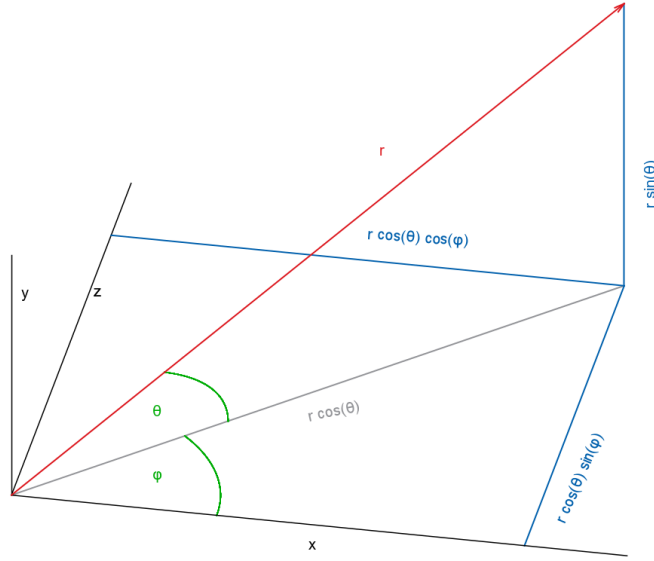


Figure 5.4: Angles how they are chosen for polar plots [53]

$\text{CH}_3\text{NH}_3^+ - \text{CH}_3\text{NH}_3^+$ interactions or the $\text{CH}_3\text{NH}_3^+ - \text{PbI}_3$ interactions.

In figure 5.5 the starting structure of a $4 \times 4 \times 4$ super cell is shown. Like one can see all the spots of the plot are located at the bottom left or at the bottom right of the plot. This denotes all the dipoles where initially chosen with perfect alignment to the \mathbf{z} axes. This structure was pre-equilibrated and taken as the starting structure for one of our ab-initio molecular dynamics simulations.

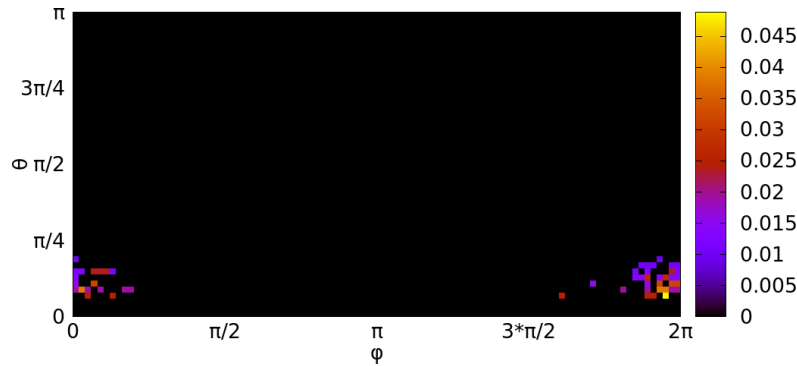


Figure 5.5: Aligned starting orientations of the CH_3NH_3 molecules in a $4 \times 4 \times 4$ super cell

For the second considered cell which is also a $4 \times 4 \times 4$ super cell we used a randomly chosen initial structure of the CH_3NH_3^+ molecules which can be seen in figure 5.6. Like one can see, the spots that denote the orientations of the organic molecules are now distributed over the entire region of the area.

The third cell was chosen now as a $6 \times 6 \times 6$ super cell which contained 378 organic molecules. This system again shows a random starting distribution of the organic molecules and once more the dipoles or more clearly their orientations are distributed over the whole range of the θ and φ area.

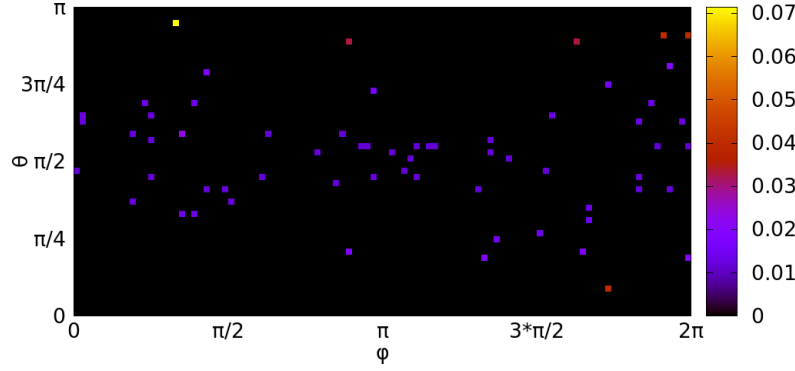


Figure 5.6: Random starting orientations of the CH_3NH_3 molecules in a $4 \times 4 \times 4$ super cell

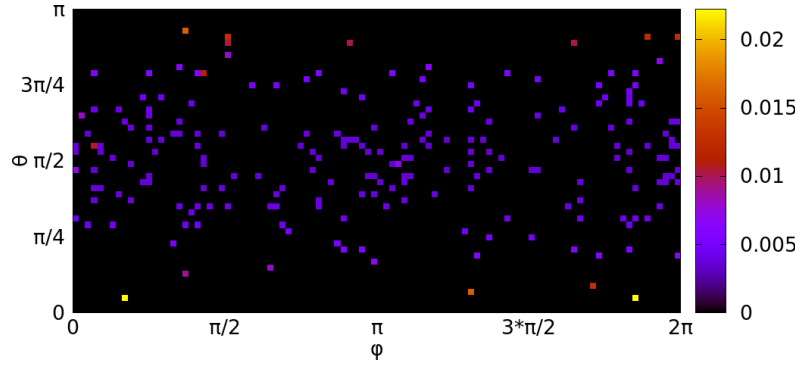


Figure 5.7: Random starting orientations of the CH_3NH_3 molecules in a $6 \times 6 \times 6$ super cell

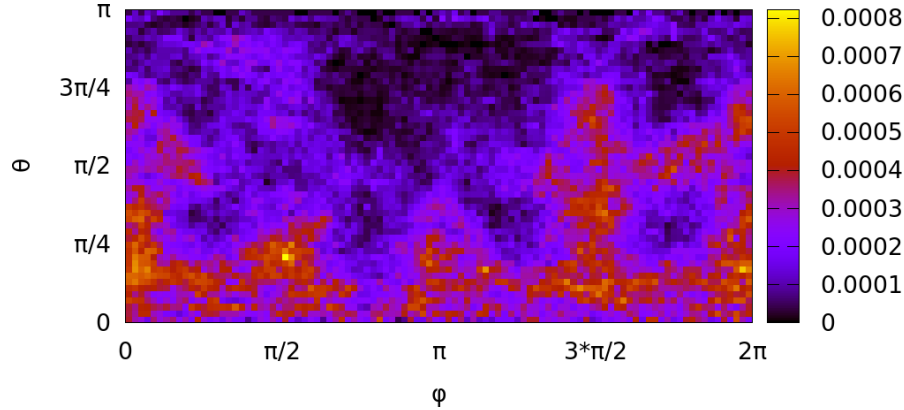


Figure 5.8: Average orientation of organic molecules during the simulation from 160ps – 320ps of a $4 \times 4 \times 4$ super cell with an aligned starting structure

Comparing the initial structures with the structures gained from the molecular dynamics there are some properties that are the same in all systems. With a close look one is able to see four denser stripes along φ in the polar plots (5.8 to 5.10). The first stripe is located around $\varphi = 0$, the second at $\varphi = \frac{\pi}{4}$, the third about $\varphi = \pi$ and the last in the area of $\varphi = \frac{3\pi}{2}$.

A similar behaviour is observed along θ in figures 5.9 and 5.10. Here there are three maxima, the first at $\frac{\pi}{8}$, the second around $\frac{\pi}{2}$ and the last about $\frac{7\pi}{8}$. In the case of the aligned structure (figure 5.8), this behaviour is only present in the lower part of the plot. This is obviously caused by the chosen starting structure. Comparing figure 5.5 and 5.8,

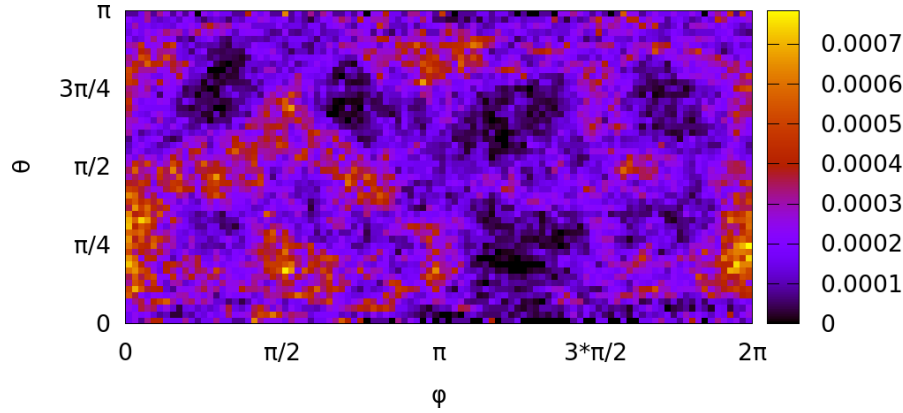


Figure 5.9: Average orientation of organic molecules during the simulation from 80ps – 160ps of a $4 \times 4 \times 4$ super cell with a random starting structure

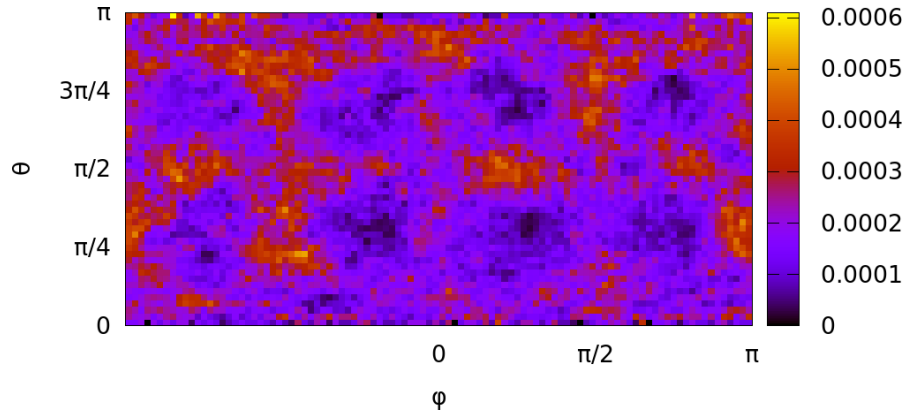


Figure 5.10: Average orientation of organic molecules during the simulation from 3000fs – 7323fs of a $6 \times 6 \times 6$ super cell with a random starting structure at 300K

the main maxima of both structures are located in the lower left and lower right region of the plots. It seems like the orientations of the organic molecules would still smear out from their initial orientations. Nevertheless one can see the arising maxima around $\frac{\pi}{2}$. The influence of the number of samples which are taken to describe a polar plot also influences the results. We compared polar plots which were calculated out of a different number of geometries. The behaviour which we observed can be described as follows, the plots show a mean value gained out of the number of different time steps considered and the number of dipoles present in the cell and a mean value will be more representative the more samples one has. Therefore the more samples one has the more the mean values will be pronounced because this is the most probable orientation for an organic molecule during a simulation. In the case of the polar plot for the $4 \times 4 \times 4$ with aligned starting structure we used 512000 samples, for the random $4 \times 4 \times 4$ we took 256000 and for the random $6 \times 6 \times 6$ structure we had 311040 samples at our disposal. This is the reason why, when comparing the figures 5.9 and 5.10 the maxima and minima are less pronounced in the case of the $4 \times 4 \times 4$ structure. But this does not mean they show a different behaviour they show the same behaviour but the $6 \times 6 \times 6$ structure is made out of twice as many points.

Next figure 5.11 and 5.12 show histograms for θ for the $4 \times 4 \times 4$ with the random starting structure and the $6 \times 6 \times 6$ as well with the random starting structure. These plots show

the relative frequencies of the various θ angles. This is in principle a one dimensional version of the polar plots. One does not consider the angle φ but is only interested in the relative orientations of the organic molecules along the spherical angle. These plots should make it more easy to see the minima and maxima which were discussed before according to the polar plots. If one inspects figures 5.11 and 5.12, one is able to see very clearly the three maxima which were mentioned above. It is also interesting to mention the $6 \times 6 \times 6$ super cell shows this three periodic maxima and a slight linear increase with increasing angle θ . The histogram for the $4 \times 4 \times 4$ random starting structure too shows the periodic maxima and a slight linear growth. But in this case the linear growth is pointing in the opposite direction (from π to 0). The slopes which increasing in direction $\theta = \pi$ or $\theta = 0$ should be equivalently because we consider a cubic cell and therefore it should not matter whether the organic molecules are oriented more likely along the positive \mathbf{z} or the negative \mathbf{z} axis, because these directions are equal by the symmetry of the cell. The histograms for the starting configurations which are not shown here would even suggest the opposite behaviour. Note that this effect is very small but there is still a slight preference for the CH_3NH_3^+ cation to align into a particular direction as a whole.

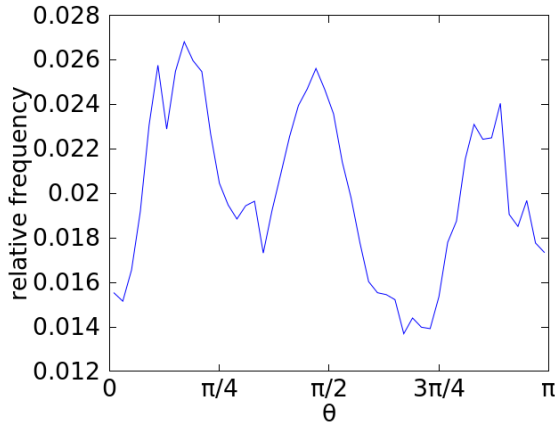


Figure 5.11: Histogram of angle θ for $4 \times 4 \times 4$ random starting structure

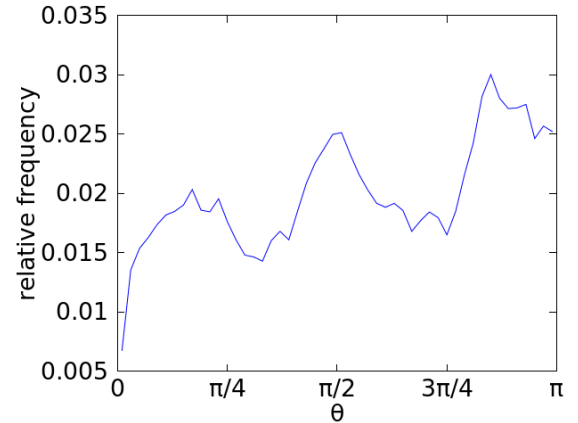


Figure 5.12: Histogram of angle θ for $6 \times 6 \times 6$ random starting structure

The histograms of the polar angle φ for the $4 \times 4 \times 4$ and $6 \times 6 \times 6$ simulations with random starting structures shown in figures 5.13 and 5.14. They are calculated in the same way as the histograms for the spherical angle. First consider the plot for the $4 \times 4 \times 4$ structure. Like mentioned above there should be at least 4 maxima but they are not easy to discern. The maxima at $\frac{\pi}{2}$ and π are overlapping. The maximum at 0 or π which is the same is slightly higher than the other maxima. The histogram for the $6 \times 6 \times 6$ structure shows a very similar behaviour. But there is a difference, like in the case of the angle θ the two histograms for φ are somehow mirrored. In this case the maxima of the π and $\frac{3\pi}{2}$ are connected. There is again a peak which is slightly higher than the others. Again the different directions 0 or 2π , $\frac{\pi}{2}$, π and last $\frac{3\pi}{2}$ are the same for symmetry. But again for both simulations there is a certain angle that is a little bit more pronounced compared to the other maxima. We also calculated the mean polarization for the two systems with random starting structure to compare if there are any differences in the ferroelectric ordering. It should be noted the mean value is taken over all the time steps and all the organic molecules present in the cell. The mean polarization for the $4 \times 4 \times 4$ simulation reads as $(0.09, 0.09, 0.05)^T$ and $(0.03, 0.02, -0.05)^T$ for the $6 \times 6 \times 6$ simulation. One can see the polarizations in the z direction is directly opposed in the two simulations. This

behaviour is also reflected by figures 5.11 and 5.12 where the histograms show an linear increase of the peak heights in opposed directions. The direction of this linear increase coincides with the values of the mean polarization. The x and y components are less in the case of the $6 \times 6 \times 6$ simulation which can be seen out of the histograms for φ if one compares the height and the width of the peaks in the x , y and z direction. In the case of the $6 \times 6 \times 6$ simulation the area under the peaks is nearly equal for the $-x$, x directions and the $-y$, y direction. In the case of the $4 \times 4 \times 4$ simulations the difference between the positive and the negative direction is more pronounced and therefore this results in a higher mean polarization in x and y than in the case of the $6 \times 6 \times 6$ simulation.

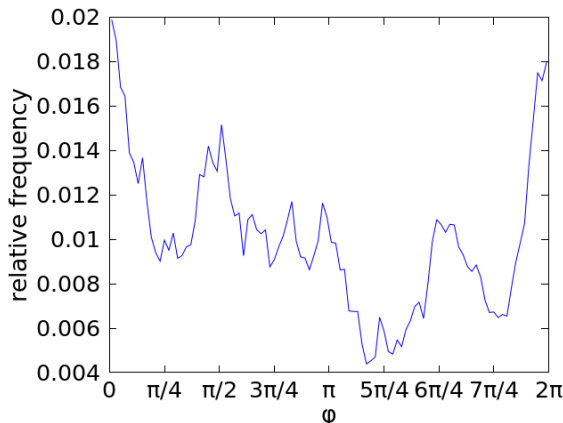


Figure 5.13: Histogram of angle φ $4 \times 4 \times 4$ random starting structure

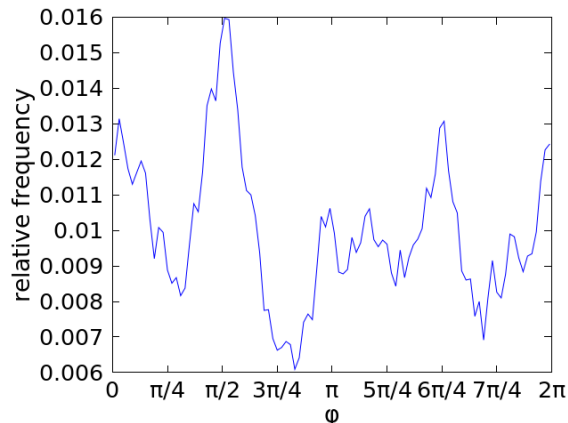


Figure 5.14: Histogram of angle φ $6 \times 6 \times 6$ random starting structure

Next we downfolded the map plots (figures 5.8 to 5.10) to an area which extends from 0 to $\frac{\pi}{2}$ in the azimuthal angle θ and the polar angle φ . These plots can be seen for the $6 \times 6 \times 6$ and the $4 \times 4 \times 4$ simulations, both with a random starting structure in figures 5.15 and 5.16. At a first glance these plots look very different but this is caused by the number of samples taken for each plot. The downfolding of the plots was done to improve statistics under the use of the symmetry elements of the cubic system. Therefore we used the facts that the directions x and $-x$ are the same which is also true for the y and z directions. Like one can see there is a blueish elliptical space in both plots. It should be mentioned the orientations of the major axes enclose an angle of about $\frac{\pi}{2}$. Nevertheless the preferred orientations of the two simulation are the same which can be seen much better in these condensed plots compared to the map plots which show the whole range. Now if one looks carefully one is able to see there is a more favourable triangle at the lower left hand side of the ellipse in figure 5.15 and on the other hand if one looks at figure 5.16 there is also a more pronounced triangle but this time it located on the opposite side of the ellipse. Therefore these two plots are related to each other by mirroring the figure under the use of a mirror plane perpendicular to the page and located at $\varphi = \frac{\pi}{4}$. The same was observed in the cases for the histograms for θ and φ .

Next unit cells for the most likely orientations of the organic ions should be shown. These structures were extracted from the ab-initio molecular dynamics simulation of the $6 \times 6 \times 6$ system. Figure 5.17 and 5.18 show the orientation of the dipoles along the principal axis y . Through symmetry it is equally likely to find the organic molecule oriented along any other of the principal axes. The location of the organic molecule is chosen in a way that it is surrounded by four iodine atoms. This is very favourable because the methyl-ammonium molecule is positively charged and the iodine atoms are negatively

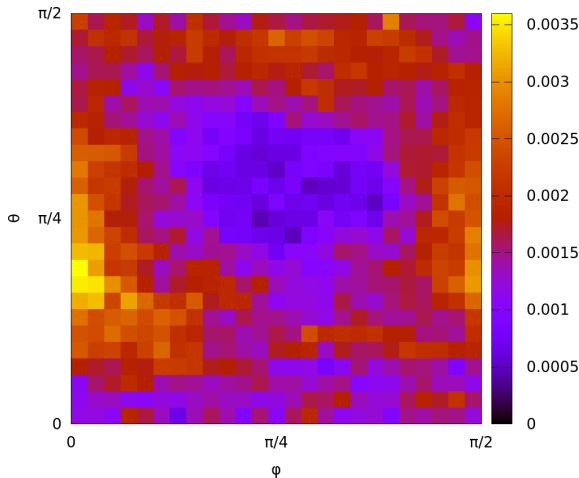


Figure 5.15: Condensed map plot of the $4 \times 4 \times 4$ simulation with random starting structure

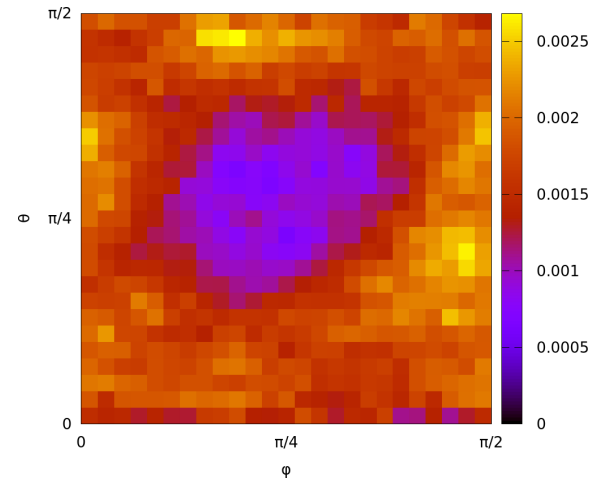


Figure 5.16: Condensed map plot of the $6 \times 6 \times 6$ simulation with random starting structure

charged. The distance to the lead atoms is maximal in this arrangement which is also very favourable because the lead atoms are positively charged and so are the organic molecules and therefore they try to diminish the electrostatic repulsion between them. Therefore it looks like the organic molecule attempts to compensate its positive charge trough the iodine atoms.

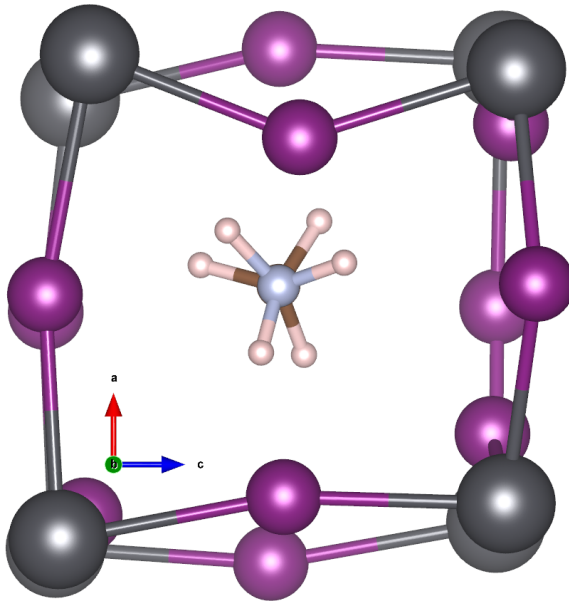


Figure 5.17: CH_3NH_3^+ oriented along the **y** axis (view along **y**)

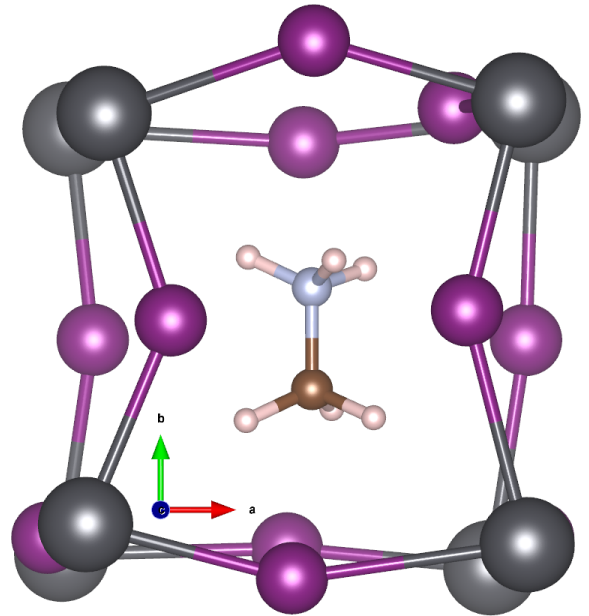


Figure 5.18: CH_3NH_3^+ oriented along the **y** axis (view along **z**)

The next very favourable structure which was extracted from the molecular dynamics simulations was the orientation of the dipole along the face diagonals of the cubic unit cell. This behaviour is shown in figures 5.19 and 5.20. The methyl-ammonium cations are not aligned perfectly along the phase diagonals but are slightly tilted towards the **xy** plane. This can be seen best in the condensed map plot of the $6 \times 6 \times 6$ simulation (figure 5.16) where slightly brighter spots arise where the dipoles are shifted from the face

diagonal by 10° towards the **xy** plane or the **z** axis. In these figures the organic molecules are again located such that they are surrounded by four iodine atoms in the centre of the cage. This time the dipole points towards iodine atoms located on top and bottom of the cage which can best be seen in figure 5.20. Hence also in this configuration the dipole tries to avoid the partially positively charged lead atoms. Again it is very important to mention orientations which are related to the here shown by symmetry are equally likely. Therefore not only the tilting from the face diagonal of the **yz** plane but also the configurations belonging to the face diagonals of the **xy** and **xz** are of great importance.

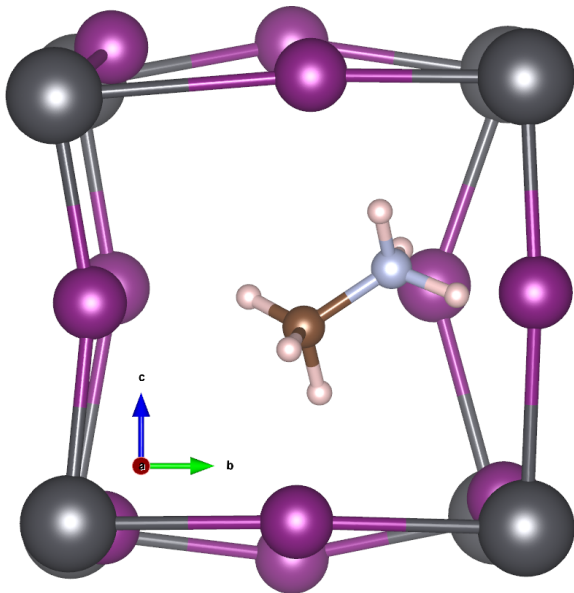


Figure 5.19: CH_3NH_3^+ oriented along the diagonal of **yz** area but tilted about 10° towards the **y** axis (view along **x**)

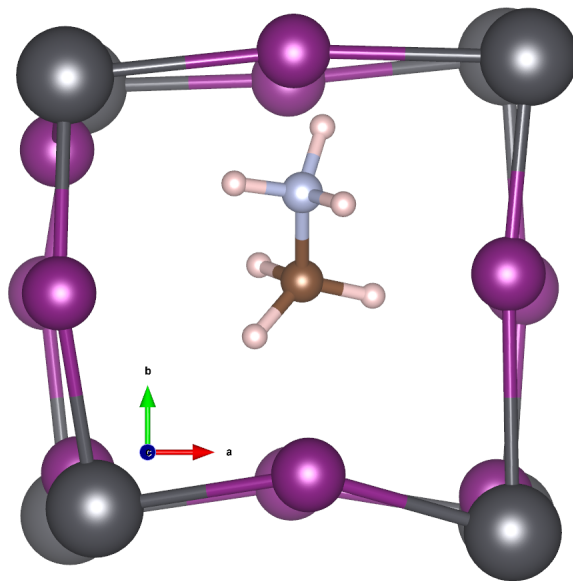
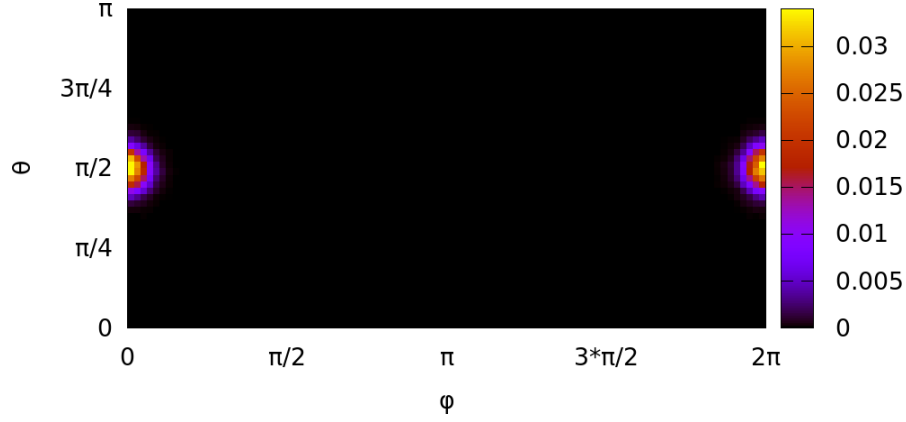
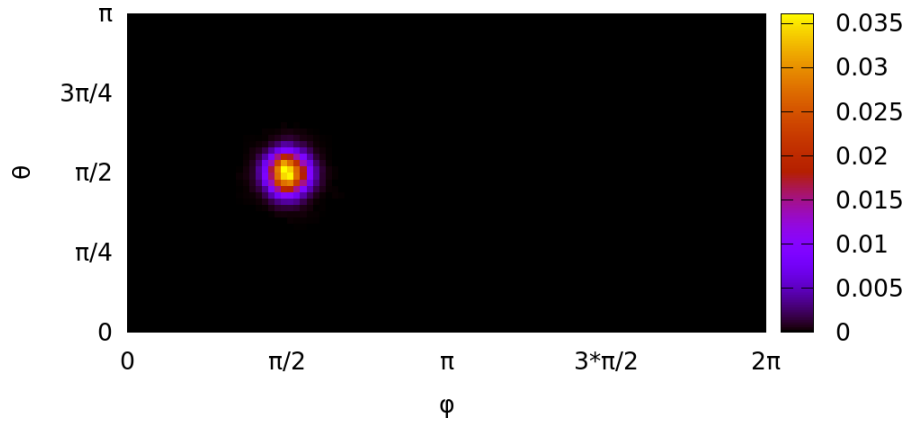
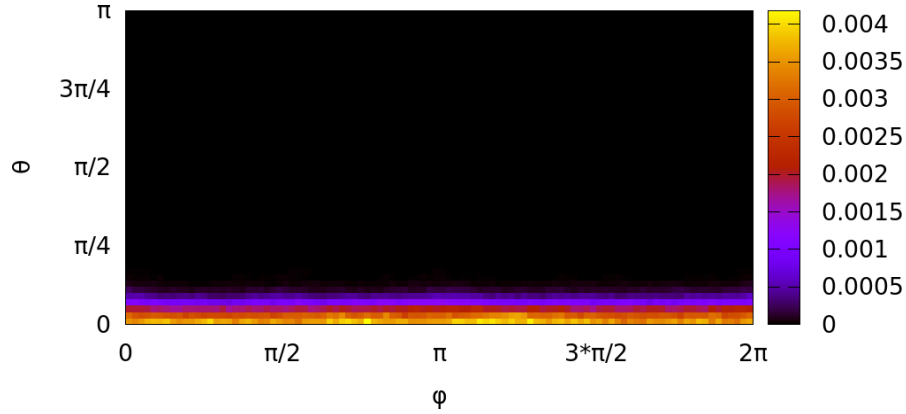


Figure 5.20: CH_3NH_3^+ oriented along the diagonal of **yz** area but tilted about 10° towards the **y** axis (view along **c**)

5.2.4 Behaviour of the inorganic framework

Figures 5.21 to 5.23 show polar plots of the vectors defined by a certain lead atom and a single iodine atom covalently bonded to it. To get the bonding vectors from lead to iodine, first of all one has to determine the iodine atoms which are next to the considered lead atom. Next we determined which vectors are directed along the positive principal axes **x**, **y** and **z**. Afterwards this bonding vectors were transformed to spherical coordinates again and the distribution of the corresponding angles is shown in the following plots. The first plot (figure 5.21) for example shows the binding vector between lead and iodine atoms (in spherical coordinates) in the positive **x** direction, the second plot is the same for the **y** direction and so on. The cages are defined in a way that the lead iodine bonds always align with certain Cartesian coordinate axes. The interesting point to mention is that there are no equilibration steps before we started the recording of this plots. Nevertheless the bonds are very rigid and only fluctuate around their equilibrium positions. In the case of the lead iodine bond in **z** direction this is true too. The smearing of this bond along the whole range φ is caused by the use of spherical coordinates in this plots. If θ equals zero the bond (or the vector) is pointing towards the pole of the sphere. What one can see here is also just a fluctuation around an equilibrium position but it is smeared over the whole range of φ caused by using spherical coordinates.

Figure 5.21: *PbI* bond pointing in **x** directionFigure 5.22: *PbI* bond pointing in **y** directionFigure 5.23: *PbI* bond pointing in **z** direction

As a result one is able to consider the motions of the lead and iodine atoms as negligible small for the parametrization of the Monte Carlo code. In other words, one is now able to model the potential energy which arises due to the cage as approximately independent of the orientations of the surrounding dipoles.

Like mentioned before we will use fixed positions for the dipoles in the Monte Carlo model. It was important to know how well this approximation is observed in molecular dynamics simulations. Therefore we monitored the center of mass positions of every single

organic molecule during the whole simulation. From this we calculated the meansquare displacement which reads as:

$$var(x) = E[X - E[X]] = \frac{1}{N} \sum_{i=1}^N (\mathbf{x}_i - \bar{\mathbf{x}})^2, \quad (5.6)$$

where N denotes the number of time steps, \mathbf{x}_i denotes the actual position and $\bar{\mathbf{x}}$ the mean position during the whole simulation. The mean square displacement for a single organic molecule fluctuated between values of about 0.05\AA^2 to 0.26\AA^2 . Out of this one was able to calculate a mean variance were all organic molecules were considered, which resulted in a value of 0.14\AA^2 . For comparison the diameter of a unit cell is about 6.35\AA . As a result it will be a good approximation to consider the positions of the methyl-ammonium molecules as fixed in the Monte Carlo approximation which sounds also very reasonable if one thinks of them as dipoles which are locked in cages build by the lead and iodine atoms.

5.2.5 Comparing ab- initio molecular dynamics of two different exchange correlation potentials

Now we compare two $2 \times 2 \times 2$ simulations but carried out with different exchange correlation potentials and determine their influence on the behaviour of the organic molecules in the cells. The first one was calculated with the standard PBEsol potential. The second one was calculated with PBEsol but we also included dispersion interactions as described in section 3.5. Figure 5.24 shows the polar plot for the structures which were propagated with the PBEsol potential without dispersion interactions. There are two maxima at 0 and 2π in φ which should be considered as one single maxima because these two angles denote the same directions (positive \mathbf{x} direction). Another small reddish spot can be seen at $\theta = \frac{3\pi}{2}$ and $\varphi = \pi$ but the remaining area of the plot is nearly homogeneously populated expect some black spots. This is in agreement with the report of Wasylishen [52] who stated free rotations of the methyl- ammonium ions above $175K$ which is the transition temperature to the high temperature phase. On the other hand if one considers the $2 \times 2 \times 2$ cell which was calculated with the dispersion correction, see figure 5.25, the orientation of the dipole is more confined to particular regions of the plot. This is caused by the additional stabilization of the molecular orientation through the dispersion interactions. The bonds of the cages Pb—I were again oriented along the cartesian coordinate axes. The dipoles will align with the bonds of the inorganic framework. Like it is also the case for the $4 \times 4 \times 4$ and $6 \times 6 \times 6$ cell which were shown in section 5.2.3. The 8 minima which were present in the bigger cell don't arise in the small ones because one does not have 6 different nearest neighbours but only 3, the remaining 3 are only periodic images of the others. As a result the dipole correlation is different in this small cells which causes a different pattern for the polar plot. From this it follows that dipole-dipole correlations are present in the small system and that this influences the structural behaviour.

The alignment of the dipoles with the inorganic framework is also present in the case of the PBEsol potential calculated without dispersion interaction (figure 5.24), but not so pronounced. If one takes into account the experimental data where it was shown that the methyl- ammonium ions are able to freely rotate within 15ps it seems more reasonable to use the PBEsol potential which resembles this behaviour in a more satisfactory manner. Because here the methyl- ammonium ions are more able to rotate freely and they should show a rotational behaviour when considering the duration of 56ps of our simulations.

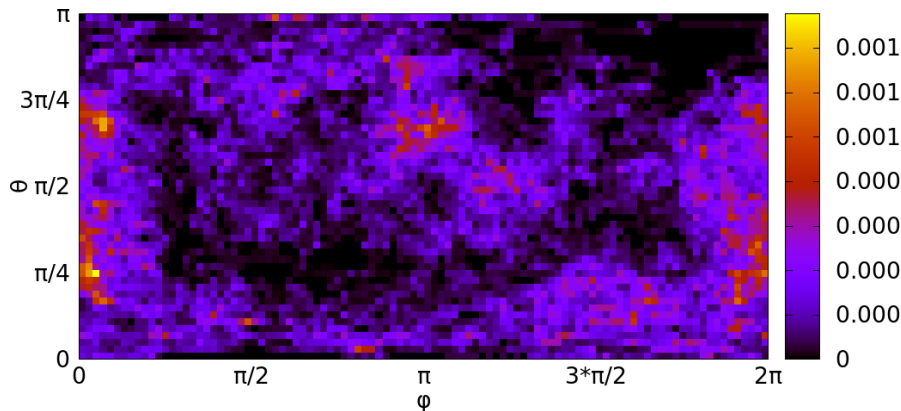


Figure 5.24: Polar plot of 2x2x2 structure calculated with PBEsol

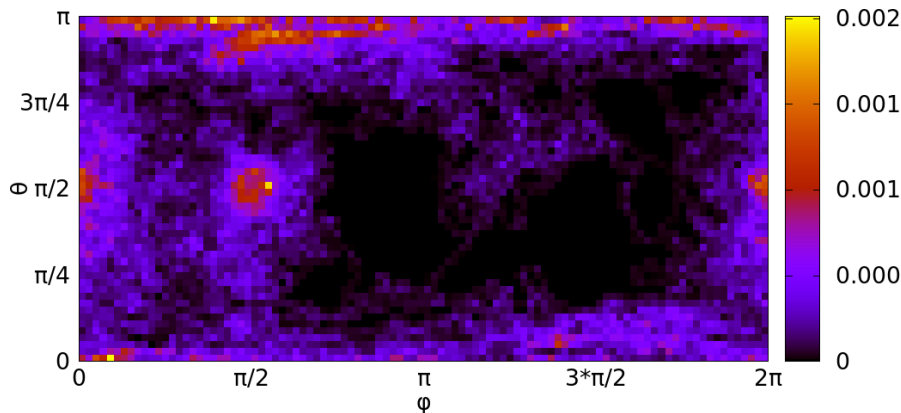


Figure 5.25: Polar plot of 2x2x2 structure calculated with PBEsol and included dispersion interactions

5.2.6 Considering different coordination spheres

This section will consider the relative orientation of the organic molecules in the first three coordination spheres to each other. Therefore one has to determine the organic molecules which are in the different coordination spheres relative to a chosen dipole. This is graphically depicted in figure 5.26 for two dimensions. If one is interested in the different coordination spheres of the green molecule (in figure 5.26) the nearest neighbours (first coordination sphere) are depicted in blue and the next-next nearest neighbours (second coordination sphere) are shown in red. If one remembers that we are dealing with a cubic system then the first coordination sphere is represented by the vectors $[\pm a, 0, 0]$, $[0, \pm a, 0]$ and $[0, 0, \pm a]$ which are the nearest neighbours along the principal axes. The symbol a denotes the lattice parameter of a cubic system. By building all the combinations of plus and minus signs of the before mentioned vector one finds six organic molecules in the first coordination sphere. The second coordination sphere in a cubic system is represented by the vectors $[\pm a, \pm a, 0]$, $[\pm a, 0, \pm a]$ and $[0, \pm a, \pm a]$ which are the interaction partners along the face diagonals. From this it follows, there 12 organic molecules in the second coordination sphere. The third coordination sphere for which there exists no satisfactory two dimensional analogue is represented by the vectors $[\pm a, \pm a, \pm a]$. Hence these organic molecules are located along the face diagonals and one has 8 molecules in this coordination sphere. The distances between the organic molecules in the different coordination spheres and the central organic molecule (green sphere in figure 5.26) are a , $\sqrt{2}a$ and $\sqrt{3}$ for the

first, second and third coordination sphere respectively.

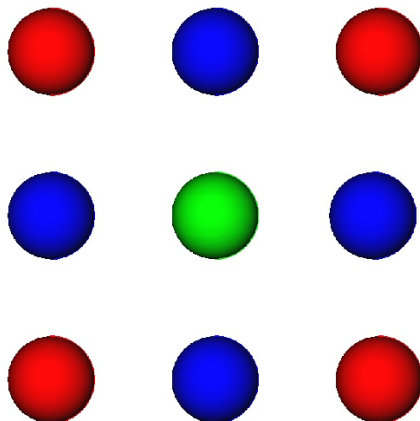


Figure 5.26: Schematic representation of first two coordination spheres in two dimensions, first coordination sphere shown in blue and the second in red

Now that we have defined the molecules which are located in the different coordination spheres we are interested in their relative orientations which will be described by the dot product:

$$\mathbf{p}_i \mathbf{p}_j = |\mathbf{p}_i| |\mathbf{p}_j| \cos(\alpha), \quad (5.7)$$

where \mathbf{p}_i describes the orientation of the central organic molecule, \mathbf{p}_j the orientation of the molecules located in one of the coordination spheres and $\cos(\alpha)$ is cosine of the angle between the two dipole vectors. By rearranging this equation one gets an expression for the relative orientation of the organic molecules:

$$\cos(\alpha) = \frac{\mathbf{p}_i \mathbf{p}_j}{|\mathbf{p}_i| |\mathbf{p}_j|}. \quad (5.8)$$

This equation was now taken to represent the relative orientations of the organic molecules by calculating the $\cos(\alpha)$ and assigning the calculated values to the bins of the histograms shown in figures 5.27 to 5.29. From this it follows a value of minus one denotes anti-alignment relative orientation of the considered organic molecules. A value $\cos(\alpha) = 0$ describes an orthogonal orientation of the considered molecule pair and last a value of one results in perfect alignment of the molecules. It should be noted every one of the shown histograms is normalized to one and are therefore independent of the number of dipoles in a certain coordination sphere. The relative orientations were considered for the $4 \times 4 \times 4$ simulation with aligned starting structure, the $4 \times 4 \times 4$ simulation with random starting structure and last the $6 \times 6 \times 6$ with a random starting structure too. First figure 5.27 shows the mean relative orientation of certain central organic molecules relative to the first coordination sphere. Like one can see the curves for the $4 \times 4 \times 4$ random starting structure and the $6 \times 6 \times 6$ simulation show a very similar result. They have a local maximum around 0.4 which belongs to an angle between the dipoles of about 66° and both show a preference for an anti-aligned configuration. In the case of the $4 \times 4 \times 4$ simulation with aligned starting structure the histogram shows a global maximum at 66° and only a very small peak for the anti-aligned configuration. If one thinks of the aligned starting configuration this could be interpreted as that the system

is still equilibrating and therefore the pronounced orientations are shifted towards more aligned configurations. This explains why the peak at 66° is more pronounced and the peak for the anti-aligned configuration is underestimated. If one would run the $4 \times 4 \times 4$ simulation for the aligned starting structure longer the histogram would transform to a shape like shown by the remaining simulations.

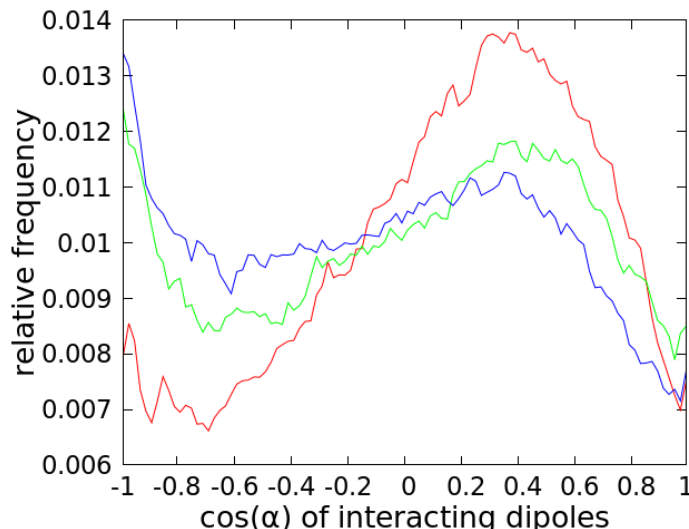


Figure 5.27: Relative dipole orientation of nearest neighbours of three different simulations. $4 \times 4 \times 4$ with aligned starting structure (—), $4 \times 4 \times 4$ with random starting structure (—), $6 \times 6 \times 6$ with random starting structure (—)

Figure 5.28 shows the histogram for the second coordination sphere. In this case all three simulations coincide very well although also here the $4 \times 4 \times 4$ simulation with aligned starting structure shows a slightly more pronounced peak for the aligned configuration. For the second coordination sphere all simulations show a local maximum at -0.4 which belongs to a relative angle between the molecules of 113° . For this coordination sphere the molecules show a preference for the aligned configuration which is the opposite of the first coordination sphere. If one compares the histograms of the $6 \times 6 \times 6$ simulations the histogram of the second coordination sphere is the mirror image of the histogram of the first coordination sphere. This can be visualized by thinking of a mirror plane orthogonal to the paper plane located at value of zero at the x -axis. The $4 \times 4 \times 4$ simulation too shows this image-mirror-image behaviour.

Last, figure 5.29 again looks very similar to the histograms of the first coordination spheres. The $4 \times 4 \times 4$ and $6 \times 6 \times 6$ simulations both with random starting structure again show a local maximum around 62° and a preferred anti-aligned orientation. For the $4 \times 4 \times 4$ simulation the third coordination sphere too shows the bias arising from the aligned starting configuration and therefore the right peak is over estimated and therefore the anti-aligned configuration is underestimated. Again it is very interesting to note if one mirrors the histograms of the second coordination sphere with the before mentioned mirror plane located at 0 one will get the histogram of the third coordination sphere.

From this it follows the organic molecules possess an alternating relative orientation to each other with respect to the different coordination spheres. To summarize the first coordination sphere shows a preference to the anti-aligned configuration, the second prefers the aligned configuration and the third coordination sphere shows a preference for the

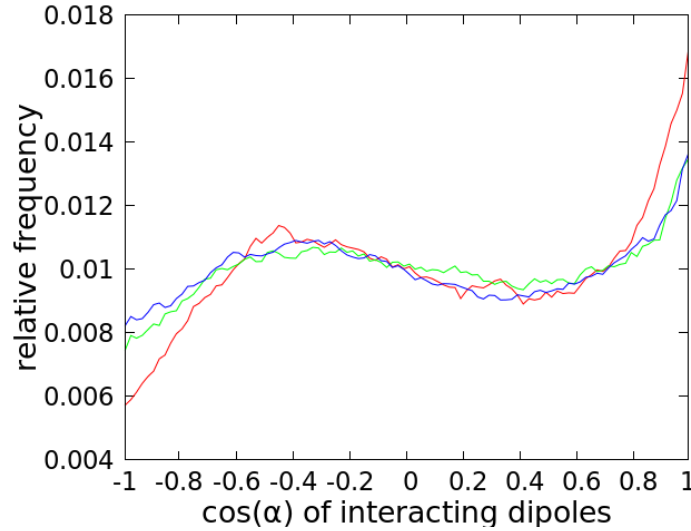


Figure 5.28: Relative dipole orientation of next-nearest neighbours of three different simulations. $4 \times 4 \times 4$ with aligned starting structure (—), $4 \times 4 \times 4$ with random starting structure (—), $6 \times 6 \times 6$ with random starting structure (—)

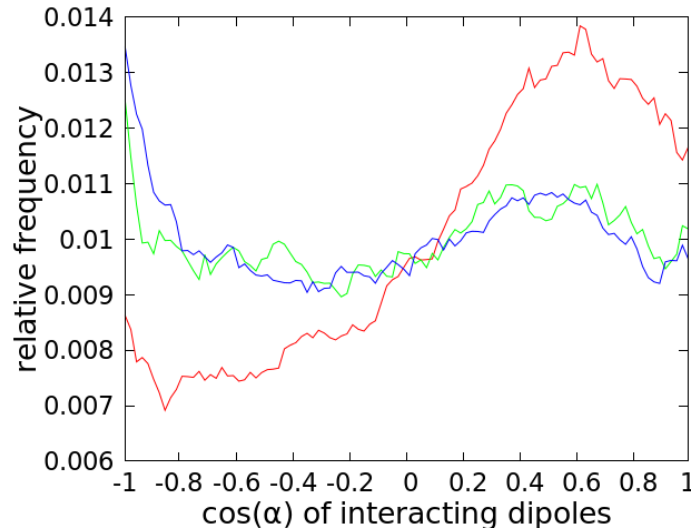


Figure 5.29: Relative dipole orientation of third-nearest neighbours of three different simulations. $4 \times 4 \times 4$ with aligned starting structure (—), $4 \times 4 \times 4$ with random starting structure (—), $6 \times 6 \times 6$ with random starting structure (—)

anti-aligned configuration. Additionally every coordination sphere possesses a local maximum at about 60° for the odd coordination spheres and 113° for the even coordination spheres. Moreover it is interesting to look at the differences of the peak heights for the simulations with random starting structures and to compare them for the first and third coordination sphere. The difference of the peak height is nearly the same for both simulations and therefore the preference for the certain configurations should be equally likely for both coordination spheres. In general one would have to use the areas under the peaks for comparison but because the shapes of the curves are so similar one is also able to use the peak heights as a first approximation.

5.2.7 Correlation of CH_3NH_3 – CH_3NH_3 and PbI_3 – CH_3NH_3 movement

Now we will consider how the rotation of the molecules will be influenced by each other and how the thermal fluctuations of the cage will influence the motion of the organic molecules. For the analysis of the correlated motion of the individual parts of the system the product-moment correlation coefficient was used which is either known as the Pearson or Bravais coefficient. This coefficient can be written as follows:

$$r(x, y) = \frac{1}{f} \sum_{i=1}^n \frac{(x_i - \bar{x})(y_i - \bar{y})}{\sigma_x \sigma_y}. \quad (5.9)$$

x_i and y_i are the different datasets respectively, \bar{x} and \bar{y} denote the mean value of the respective dataset. The terms σ_x and σ_y describe the variance of the two different datasets. f denotes the number of values which were considered and therefore it constitutes a normalization constant. The datasets will be the calculated spherical angles of the molecules vs time. For example if one desires to calculate the correlation between two neighbouring dipoles one takes the angle θ or φ from one molecule for the values x_i , and for the y_i one takes the corresponding angles of the second molecule. The sum in equation (5.9) runs over all the time steps available for the dataset. This measure of correlation is dimensionless, normalized and independent of the dataset [14]. The factor results in a value of +1 if there is positive total correlation, a value -1 for total anti correlation and a value of zero if there is no correlation between the two datasets. The coefficient was calculated with the *scipy* library of *python* [26]. This coefficient is a measure for the linear dependence of two individual datasets. In the corresponding case of the methyl-ammonium ions in the PbI_3 cages this will not be an exact linear dependence, because the net effect is a superposition of thermal motion, the jiggling and wiggling of the cages and the rotational motion of the organic dipoles. Additionally the temperature of the considered system is very high and fluctuates around 300K during the simulation so the thermal motion should have a strong influence on the collective behaviour of the system. But as a first approximation it should be okay to deal with this coefficient to see if there is any correlated movement present. To gain the datasets for the dipole-dipole correlation, we calculated the angles θ and φ vs time for every dipole present in the considered cell. For every organic molecule we determined its nearest neighbour in the positive **x**, **y** and **z** direction. Next we calculated the correlation coefficient according to equation (5.9) for all the gained dipole pairs. This resulted in a Pearson coefficient for θ and φ , for the three considered directions for every dipole pair. Next we took the values which belonged to the same angle (θ or φ) and to the same direction and calculated a mean of all dipole-dipole pairs. This procedure gave the values listed in table 4. At a first glance these values seem to be very low but if one considers published rotational barriers for methyl-ammonium which are 1.3kJ/mol [16] it is very reasonable that there is a big thermal influence present at 300K. It should be mentioned that the corresponding *p-values* which are a measure for the statistical significance of a hypothesis were lower than 0.00001 for a significance level of 0.01. Although these values seem to be very low they also mean that there is guaranteed correlated movement between the individual parts of the cell but it is small because it is overlapped by thermal fluctuations of the atoms. The values were examined to determine whether there is any dependence on distance present but this was not the case. But this was only tested for the first three coordination spheres which are depicted here. For higher coordination spheres the procedure was not possible. It follows that there exists correlated movement between neighbouring dipoles. This behaviour could have been seen in section 5.2.6 when

considering the relative orientations between the different coordination spheres, which showed an ordering behaviour for the first three nearest neighbour spheres. The values of table 4 correspond to the simulation of the $6 \times 6 \times 6$ super cell. This analysis was also carried out for the $4 \times 4 \times 4$ systems with random and aligned structures yielding comparable values.

Table 4: Pearson- correlation coefficient of dipoles in the first three coordination spheres at 300K

neighbour direction	$r(\theta_{\text{dipole}}, \theta_{\text{dipole}})$	$r(\varphi_{\text{dipole}}, \varphi_{\text{dipole}})$
x	-0.041	0.016
y	-0.045	-0.008
z	0.021	-0.019
xy	-0.006	-0.014
xz	0.026	-0.030
yz	-0.008	0.023
xyz	0.006	-0.063

Next we determined the correlation coefficients between the movement of PbI bonds forming the cage and the organic molecules which are locked inside them. For this, we took a certain dipole and again calculated its spherical angles with respect to time. Next we determined the lead atom which was next to this dipole and determined the vectors which connect this lead atom with the iodine atoms in the positive **x**, **y** and **z** direction. For these vectors the spherical angles were calculated with respect to time. Having the datasets that are needed for equation (5.9), we calculated the correlation between the dipoles and the cage atoms that are next to them. The resulting values are listed in table 5. In this case, we also calculated the influence whether the PbI bond is moving in the **xy** plane on the motion of the methyl- ammonium ion along θ (angle with respect to the **xy** plane). This is shown in the fourth column of table 5. This was also done for the opposite behaviour if the dipole moving in the **xy** plane and the PbI bond oscillating along the polar angle θ . It is remarkable that the magnitudes of values which describe the dipole-dipole correlation or the cage-dipole correlation are of the same size. This means that the motion of a certain dipole is influenced equally by the surrounding cage atoms (lead and iodine) and the dipoles that are located in the first three coordination spheres. This can related to a medium range order which is present in the considered system which is also suggested by the histograms for the relative orientation of the dipoles shown in section 5.2.6.

Table 5: Pearson- correlation coefficient of dipole cage interaction at 300K

PbI- bond direction	$r(\theta_{\text{dipole}}, \theta_{\text{cage}})$	$r(\varphi_{\text{dipole}}, \varphi_{\text{cage}})$	$r(\theta_{\text{dipole}}, \varphi_{\text{cage}})$	$r(\varphi_{\text{dipole}}, \theta_{\text{cage}})$
x	0.054	0.025	0.017	0.027
y	0.011	0.019	0.024	0.022
z	0.006	0.016	0.007	0.001

What one can deduce from these values is that the correlation between the dipoles and the cage atoms is slightly higher than the correlation between neighbouring dipoles. Confirmation can be gained by comparing the values of table 4 and 5. From this analysis we are able to say that the cage will play a very important role

5.2.8 Comparing two simulations with different hydrogen masses

In the ab-initio simulations we adjusted the hydrogen mass to be 4 a.u. because this allowed us to use a larger time step and the energy difference for the stopping criterion has not to be chosen that small. Therefore we were able to perform simulations for a longer simulation time with the same computational cost. We calculated the moment of inertia by equation (5.10) for both the organic molecule with a hydrogen mass of 1a.u. and for the second species with a hydrogen mass of 4 a.u.. It should be mentioned for the simulations with the lighter hydrogen atoms we are not able to choose the time step bigger than 0.7 fs because otherwise the hydrogen atoms would fly away from the molecule to which they should be confined. In the case of the higher mass hydrogen atoms we were able to choose time steps up to 2.0 fs without observing any problems during the simulations. This was used for the simulations of the $4 \times 4 \times 4$ simulations. In the case of the $6 \times 6 \times 6$ simulations we even used hydrogen masses of 6a.u. and hence we were able to use a time step of 3fs. This is caused by the fact that the maximum time step of a simulation is proportional to $\sqrt{\frac{1}{m}}$. In the following equation r_i denotes the coordinates of a certain atom and m_i is its associated mass.

$$I = \sum_{i=1}^N m_i r_i^2 \quad (5.10)$$

The moment of inertia (I) for the organic molecule with hydrogen masses of 1a.u. reads as 23.99 a.u. \AA^2 and for the species with the heavier hydrogen masses as 36.97 a.u. \AA^2 an increase of 35.1%. Therefore the moment of inertia is much higher in the case of the higher hydrogen mass. It follows the dynamics of the two systems will be different but this does not matter for analysis because we are only interested in the spatial distributions of the dipoles which will not be affected by a change in the atomic masses. This can be shown under the use of the partition function which reads as follows:

$$\begin{aligned} Z &= \sum_{i=1}^N e^{-\beta H(\mathbf{p}_i, \mathbf{x}_i)} \\ &= \sum_{i=1}^N e^{-\beta \left(\frac{\mathbf{p}_i^2}{2m_i} + V(\mathbf{x}_i) \right)} \\ &= \sum_{i=1}^N e^{-\beta \frac{\mathbf{p}_i^2}{2m_i}} e^{-\beta V(\mathbf{x}_i)} \end{aligned} \quad (5.11)$$

In this equation β denotes the inverse temperature $k_b T$, $H(\mathbf{p}_i, \mathbf{x}_i)$ denotes the energy depending on the momentum of particle i , \mathbf{p}_i and its potential $V(\mathbf{x}_i)$, N is the total number of particles in the system, m_i are the masses of the considered particles and last \mathbf{x}_i denotes the position of the particle. Like one can see the partition function which contains all information about a certain system can be split into a part depending on momentum and a part coupled to space. During this thesis we will consider only spatial distributions of the organic molecules and therefore this will not be affected by a change in mass. The reason for this is the the spatial part of the partition function is independent of the atomic masses and so will be our results.

Now to be completely sure we compared two simulations where the simulation parameters were the same except of the hydrogen masses. Like already mentioned the first simulation

was carried out with hydrogen masses of 1 a.u. and the second with hydrogen masses of 4 a.u.. To keep computational costs as low as possible for this simulations we considered single unit cells. The time step of both simulations were taken as 0.7fs and we performed 600000 steps corresponding to a total simulation time of 42 ps. Figure 5.30 shows the distributions for the azimuthal angles φ . At the top one is able to see the simulation with 1 a.u. and at the bottom one is able to see the simulation carried out with a hydrogen mass of 4 a.u.. Like one can see both simulations show peaks at the same positions. The peaks only differ slightly in height and width. If one remembers that we are considering cubic cells the \mathbf{x} , \mathbf{y} and \mathbf{z} directions are equivalent. And because the peaks are arising on the angles φ which belong to the same direction in Cartesian coordinates the simulations with different hydrogen masses show a very similar result.

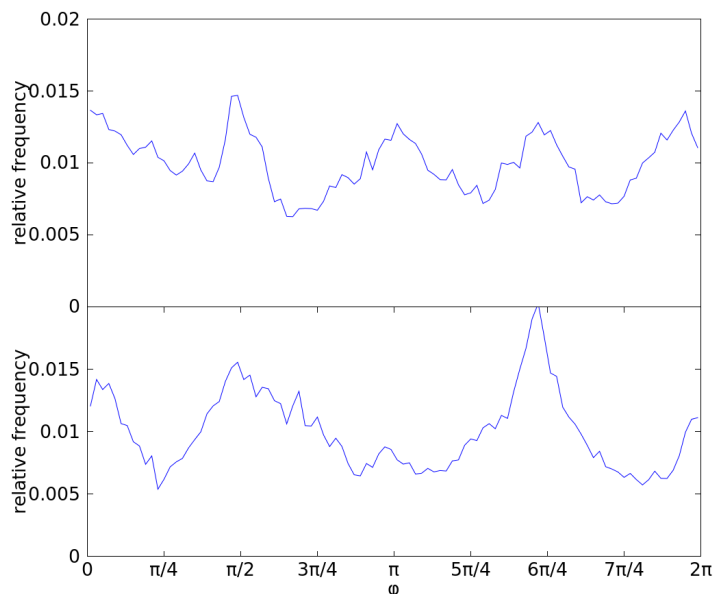


Figure 5.30: φ histogram for CH_3NH_3 . **top:** hydrogen masses of 1 a.u.; **bottom:** hydrogen masses of 4 a.u.

Next figure 5.31 shows the probability distributions for the polar angles θ of the two simulations. There is a small peak located at $\frac{\pi}{2}$ which looks different in the two simulations at a first glance. But if one compares the values written on the y axis the difference is very small and therefore again the graphs can be considered as the same within the range of statistical uncertainty. It follows if we consider the spatial distributions of the dipoles it does not matter which hydrogen masses are used.

For completeness also the dynamical behaviour of the two systems was considered. Figure 5.32 shows the absolute deviation of the angle φ from the mean value at any time step t . The mean value corresponds to the mean value over all the time steps. Like one is able to see at a first glance the upper curve representing the simulation with an hydrogen mass of 1 a.u. shows a much more diffuse behaviour than it is the case in the simulation with higher hydrogen mass. The same is true for the polar angle θ shown in figure 5.33. This is the result which we expected because a lighter atom should show a more pronounced dynamical behaviour. The results were additionally checked by Fourier transforming the results of figures 5.32 and 5.33 which clearly showed that the simulations with lighter hydrogen atoms had higher frequency contributions than in the case with higher hydrogen masses.

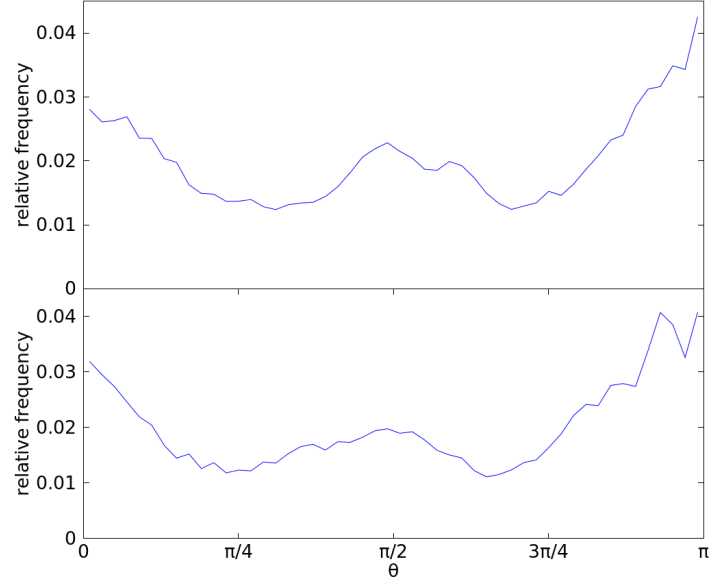


Figure 5.31: θ histogram for CH_3NH_3 . **top:** hydrogen masses of 1 a.u.; **bottom:** hydrogen masses of 4 a.u.

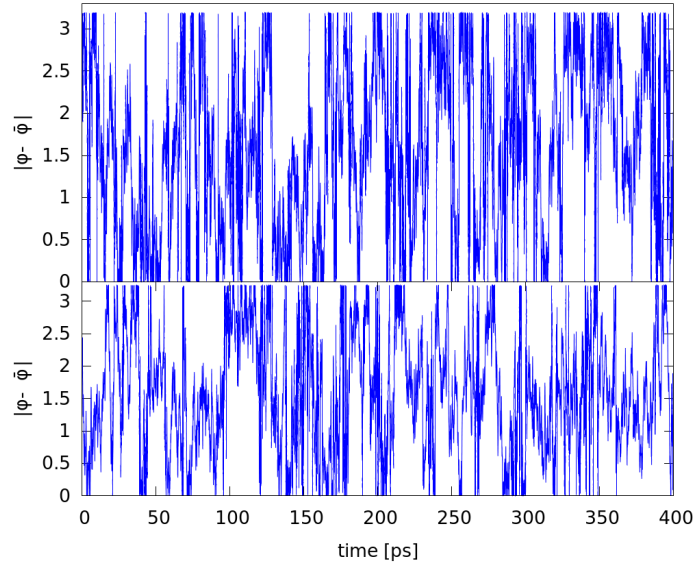


Figure 5.32: time dependence of φ for CH_3NH_3 . **top:** hydrogen masses of 1 a.u.; **bottom:** hydrogen masses of 4 a.u.

From this it follows with increasing the hydrogen masses we will change the dynamical behaviour of our methyl-ammonium molecules. On the other hand as long as we are only interested in properties which correspond to the spatial part of the partition function we are able to increase the hydrogen masses and save computational costs.

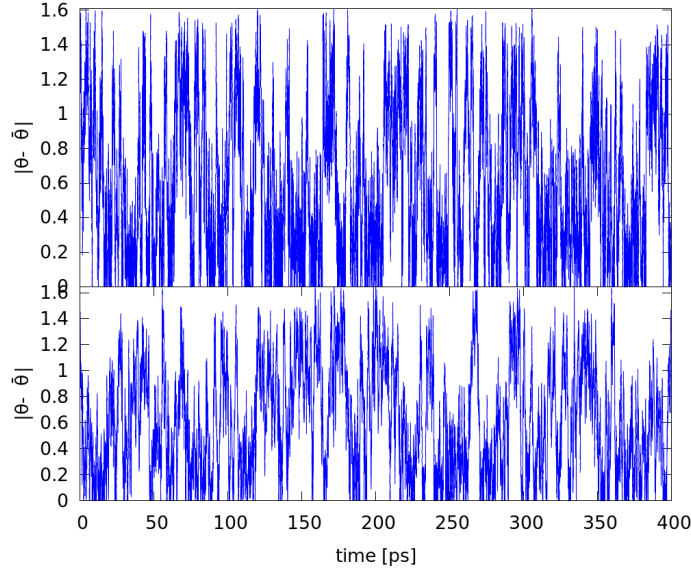


Figure 5.33: time dependence of θ for CH_3NH_3 . **top:** hydrogen masses of 1 a.u.; **bottom:** hydrogen masses of 4 a.u.

5.3 Comparing Polarization of different simulations

Next we calculated the normalized mean polarization of our ab-initio molecular dynamics simulations by the use of the following equation

$$P(t) = \left| \frac{1}{N} \sum_{i=1}^N \hat{\mathbf{p}}_i(t) \right|, \quad (5.12)$$

where $P(t)$ denotes the normalized mean polarisation for every time step, $|\hat{\mathbf{p}}_i(t)|$ denotes the L-2 norm of a single normalized dipole vector and N denotes the number of dipoles present in the cell. In this way the total polarisation is approximated by the sum of only the molecular dipoles. This will give data which is comparable to the one of the Monte Carlo approach. The value $P(t)$ lies in the interval from 0 to 1, where 1 denotes a maximal polarized system or in other words, all dipoles are aligned. The zero value reflects a system where all the different dipole contributions cancel each other and as a result there remains no net polarization.

Figure 5.34 shows the normalized mean polarisation functions for two different $2 \times 2 \times 2$ systems one calculated with the PBEsol potential (blue) and one for the PBEsol potential with included dispersion interaction (pink). For both simulations the same random starting structure was taken which can be seen by comparing the origins of the two curves which are the same. In table 6, the time mean values of the normalized mean polarisations and their corresponding variances are listed. Those values differ slightly for the two different potentials, where the value for the case of the PBEsol potential is slightly higher. The fluctuations of the net normalized mean polarization fluctuates slightly stronger in the case of the included dispersion interaction. If one remembers the comparison of the two potentials it is interesting that the rotational barrier is higher in the case of the included dispersion interaction but nevertheless the polarization varies more in this case. For both systems we took 15000fs before we took the samples for calculating the time mean value and the variance. Nevertheless, although both systems are still equilibrating and the

one with included dispersion interactions is farer away from its equilibrium structure and therefore there are stronger fluctuations in the normalized mean polarisation. Now if one compares the two curves of figure 5.34 one is able to see that the mean normalized polarisation raises at the beginning while leaving the random starting orientation and afterwards starts fluctuating between values of about 0.6 and 0.1 for the calculation with included dispersion interactions and between 0.05 and 0.7 for the PBEsol calculation.

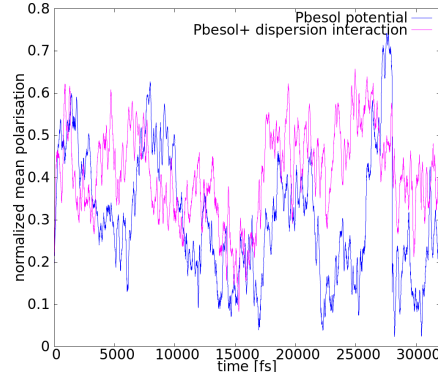


Figure 5.34: Normalized mean polarisation as a function of time for $2 \times 2 \times 2$ cells with different potentials

Next we will compare the two $4 \times 4 \times 4$ simulations with random and aligned starting structure which can be seen in figure 5.35. The aligned starting structure has a mean normalized polarization of about one.¹ As can be seen in the figure the starting mean normalized polarizations differ very strongly in their initial values. The aligned starting structure shows an exponential decay in the beginning and merges into a region where the polarization is fluctuating around a certain value which can be seen in table 6. The $4 \times 4 \times 4$ random structure has a much lower initial value. The mean normalized polarization raises slightly and after some equilibration it is fluctuating around a certain value. The values of the random and aligned starting structure are approaching each other with increasing simulation time. It should also be noted that the variances of the mean normalized polarization of the two systems, which can again be seen in table 6, are nearly equal and both are small compared to the $2 \times 2 \times 2$ systems.

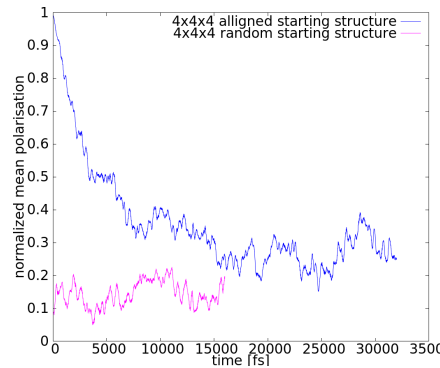


Figure 5.35: Normalized mean polarisation as a function of time for $4 \times 4 \times 4$ cells with different starting structures

¹The deviation from the exact value of one results from the fact that we made some pre-equilibration for this system which is not shown in those plots.

Now we consider the mean normalized polarization of the $6 \times 6 \times 6$ structure which can be seen in figure 5.36. If one compares the initial value to the one of the $4 \times 4 \times 4$ random starting structure one is able to see they are roughly equal. But contrary to the $4 \times 4 \times 4$ random structure, the polarization first decreases to a small plateau around 1000 fs. Afterwards the mean polarization is oscillating between values of about 0.1 and 0.03. The mean value for this simulation can again be seen in table 6. It is interesting to mention that the values for the mean normalized polarization decrease with increasing system size. This means that there is no net polarization for very big systems because if we would increase the system size further we would end at some point with a zero net polarization. We still are not hundred percent sure why the polarization decreases with increasing systems size. But a reason for this may be the formation of small ferroelectric domains in the for example **xy** plane. For bigger systems the small domains in the planes will cancel each other which is not possible for the $2 \times 2 \times 2$ systems because there are not enough dipoles present. But this assumptions has to be proven first or, corrected by a better idea.

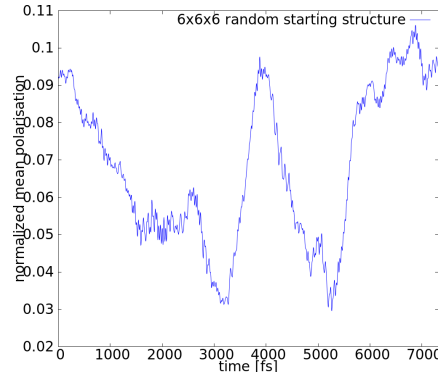


Figure 5.36: Normalized mean polarisation as a function of time for a $6 \times 6 \times 6$ cell

Table 6: Mean value and variance of normalized mean polarisation

Considered system	Mean value	variance
2x2x2 PBEsol	0.404	0.0110
2x2x2 PBEsol+ dispersion interaction	0.310	0.0259
4x4x4 random	0.154	0.0012
4x4x4 aligned	0.265	0.0021
6x6x6 random	0.069	0.0005

5.4 Parametrization of Monte Carlo Approach

To build our model Hamiltonian we started with an equation including only dipole-dipole interactions and dipole-external electric field interactions. This equation writes as:

$$\hat{H} = \sum_{i, E\text{-field}}^n (\mathbf{p}_i \cdot \mathbf{E}_0) + \sum_{i,j}^{n,m} \left(\frac{\mathbf{p}_i \cdot \mathbf{p}_j}{r^3} - \frac{(\hat{\mathbf{n}} \cdot \mathbf{p}_i)(\hat{\mathbf{n}} \cdot \mathbf{p}_j)}{r^3} \right), \quad (5.13)$$

where \mathbf{p}_i describe the dipole vectors, \mathbf{E}_0 the electric field applied, $\hat{\mathbf{n}}$ is a unit vector which points in direction of the connection vector of a certain interaction pair and r is the norm of the distance vector between the considered interaction pair. The first term describes

the interaction energy of a dipole with an external electric field, the second term describes the interaction energy of two point dipoles a distance r apart [19]. The next step is now to describe the interactions between the inorganic framework and the dipoles in a way that the cubic symmetry is not broken. To describe the cubic symmetry there exist spherical harmonics which were adapted to describe ferromagnetic effects in cubic systems [2][32]. This function can be written as follows:

$$E_{DC} = C_1 (\alpha_1^2 \alpha_2^2 + \alpha_2^2 \alpha_3^2 + \alpha_1^2 \alpha_3^2) + C_2 \alpha_1^2 \alpha_2^2 \alpha_3^2 \quad (5.14)$$

where E_{DC} describes the cage dipoles interaction, C_1 and C_2 are proportionality constants which have to be determined by parametrization and last the α_i describe the dot product of the dipole vector with a certain principal axis. For example α_1 describes the dot product of the unit dipole vector with the unit vector in \mathbf{x} direction. Therefore it is the cosine of the angle between the dipole vector and the \mathbf{x} axis. α_2 is the same but for the \mathbf{y} direction and last α_3 for the \mathbf{z} direction. Next figures 5.37 and 5.38 show the interaction terms of equation 5.14. The bright spots show regions where the function value is high and in black regions the the function value is zero. By comparing figure 5.37 and figure 5.10 one can see the spots where the spherical harmonics have their maxima the map plot gained from the molecular dynamics has its minima. This is true for both terms C_1 and C_2 of equation (5.14).

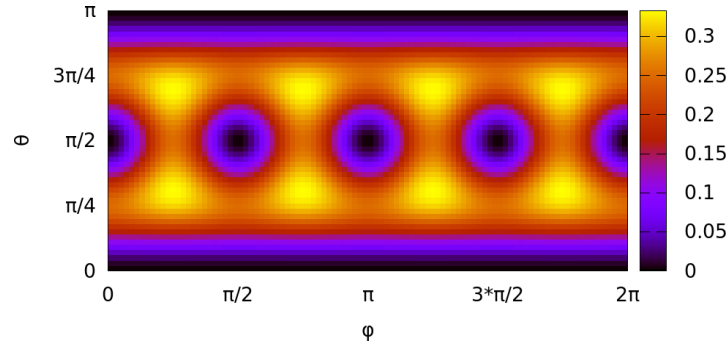


Figure 5.37: Polarplot of the C_1 term of equation (5.14)

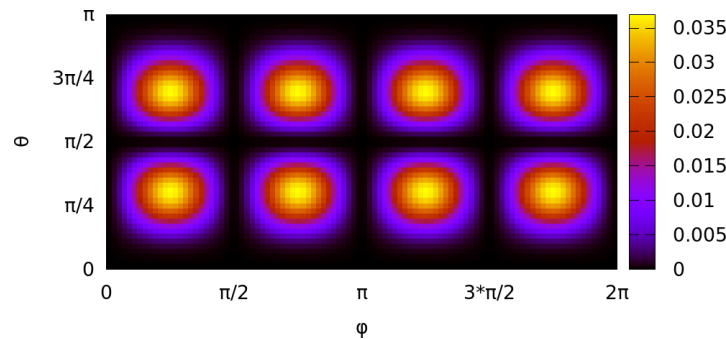


Figure 5.38: Polarplot of the C_2 term of equation (5.14)

To find appropriate values for the constants in front of each term we used the so called Boltzmann inversion. Therefore one starts with the equation for the probability of a given state which reads as:

$$\rho_i = \frac{e^{-\beta E_i}}{\sum_{i=1}^N e^{-\beta H(\mathbf{p}_i, \mathbf{x}_i)}} = \frac{e^{-\beta E_i}}{Z}, \quad (5.15)$$

here ρ_i denotes the probability that the system is in state i , Z again denotes the partition function and E_i is the energy for a given state. By taking the logarithm of this equation one is able to calculate the energy surface out of the polar plots shown earlier. It is important to have good statistics of the data if one likes to invert them and hence we used the condensed polar plots. The inversion can be written as follows:

$$\ln \rho_i = -\ln Z - k_b T E_i, \quad (5.16)$$

$$E_i = -\beta \ln \rho_i - \ln Z. \quad (5.17)$$

From this it follows, the in this way calculated energy surface is determined accurate to a constant $\ln Z$. The condensed energy surface for the $6 \times 6 \times 6$ ab-initio simulation is shown in figure 5.39. It does not matter if one knows this constant because one is able to use differences of energy values to determine the constants in equation 5.38.

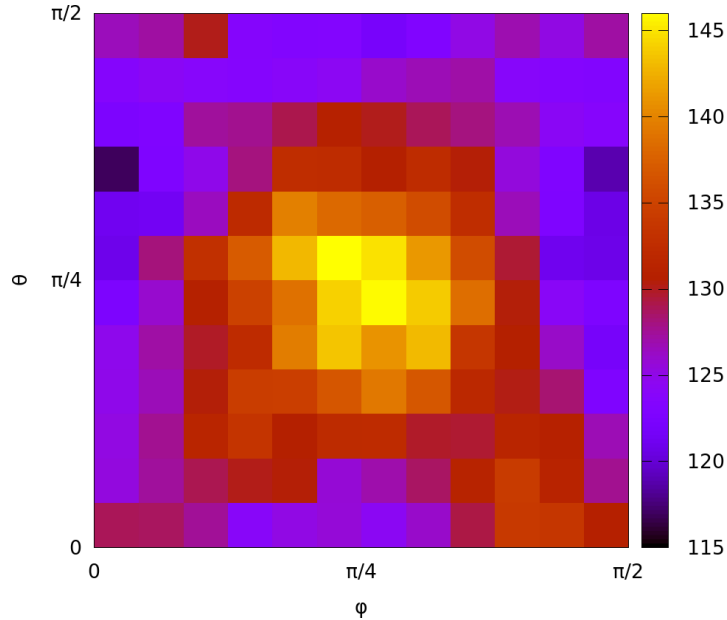


Figure 5.39: Condensed energy surface $E(\varphi, \theta)$ of $6 \times 6 \times 6$ simulation in [eV]

For the evaluation of the constants we picked certain orientations for the dipole vectors and assigned the corresponding energy of the energy surface to these orientations (figure 5.39). Next we made an Ansatz that this energy is equal to the energy calculated by equation (5.14), if the constants C_1 and C_2 would be known. Thereby we got an equation with two unknowns for every point. To overcome the fact that we do not know the additive constant $\ln Z$ we always took the energy difference between two points. This was done by setting up the equations for two points and then subtracting them. This resulted in a value of -45 meV for the C_1 term and a value of 1096 meV for the C_2 constant. With this parametrization we are able to describe the cubic symmetry which arises due to the inorganic framework dipole interactions.

What we are not able to model with this parametrization is the behaviour of the dipole-dipole arrangement for the nearest neighbours. So we had to find some term which will describe this interaction. This interaction can be considered as a mixture of dipole-dipole and cage dipole interactions. Because if a dipole rotates in his cage then this will influence the inorganic framework and therefore the dipoles which are near by. We considered the histograms for the nearest neighbours which are shown in figure 5.27. It is important to find a function that reproduces the behaviour of the $6 \times 6 \times 6$ and $4 \times 4 \times 4$ random starting structure simulations. Here we just want to consider the histograms for the nearest neighbours because these are the closest interaction partners and therefore dominate the interaction. We tried to find a function that can be seen in figure 5.40. This can be written as $u_{ij} = \frac{1}{2} \sin(\pi \cdot \hat{\mathbf{p}}_i \cdot \hat{\mathbf{p}}_j) - \hat{\mathbf{p}}_i \cdot \hat{\mathbf{p}}_j$.

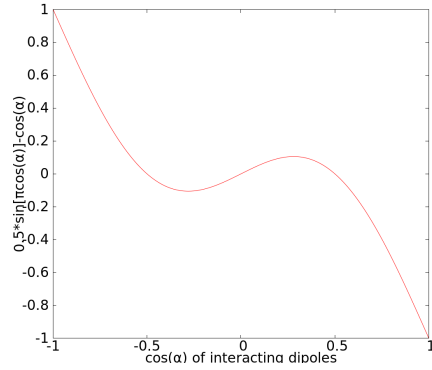


Figure 5.40: Function to describe histogram of $\cos(\alpha)$ (angle between dipoles)

Next one has to choose the appropriate dipole moment which we just took from the calculations which were presented in chapter 5.1. By changing the dipole moment in the Monte Carlo code one is able to model different organic ions or molecules, by just plugging in the desired value. For the relative epsilon ϵ_r we took an experimental value of 6.5 which was gained from optical measurements [30].

For the cell parameters, we relied on experimental values which were published by Stoumpos et. al. They performed single crystal X-ray analysis and determined the lattice parameters for several different organo halide perovskites [46]. The values that they reported and that are used in the Monte Carlo simulations can be seen in table 7. It should be noted, these lattice parameters were also taken for the geometry in the ab-initio molecular dynamics. We kept these parameters fixed during the all simulations. Now we are able to write our model Hamiltonian as follows:

$$\begin{aligned}
 \hat{H} = & \sum_{i, E-field}^n (\mathbf{p}_i \cdot \mathbf{E}_0) + \frac{1}{4\pi\epsilon_r} \sum_{i,j}^{n,m} \left[\frac{\mathbf{p}_i \cdot \mathbf{p}_j}{r^3} - \frac{(\hat{\mathbf{n}} \cdot \mathbf{p}_i)(\hat{\mathbf{n}} \cdot \mathbf{p}_j)}{r^3} \right] \\
 & + \sum_i^n [C_1 (\alpha_{1,i}^2 \alpha_{2,i}^2 + \alpha_{2,i}^2 \alpha_{3,i}^2 + \alpha_{1,i}^2 \alpha_{3,i}^2) + C_2 \alpha_{1,i}^2 \alpha_{2,i}^2 \alpha_{3,i}^2] \\
 & + C_3 \left[\sum_{i,j}^{n,nn} \frac{1}{2} \sin(\pi \cdot \hat{\mathbf{p}}_i \cdot \hat{\mathbf{p}}_j) - \hat{\mathbf{p}}_i \cdot \hat{\mathbf{p}}_j \right],
 \end{aligned} \tag{5.18}$$

where $\hat{\mathbf{p}}_i, \hat{\mathbf{p}}_j$ denote the normalized dipole vectors, the sum over i runs over all the dipoles present in the cell. The sum over j in the second term runs over all the dipoles

within the cut off radius of dipole i . In the last term the sum over j only runs over the nearest neighbours which is denoted as nn in the superscript of the sum.

Now we have all terms which are necessary to describe the considered system. Next one has to determine the constant C_3 in front of the third term. This constant was determined by a trial and error procedure. For example one tested a few different values for C_3 and considered which one satisfied the results of the molecular dynamics best. This was done by comparing the histogram of the relative dipole orientation and trying values from 0 to -50 for the constant C_3 . Then we used a least square routine to determine the deviation of the molecular dynamics and the Monte Carlo histogram. Next we took the the constant where the results agreed best with the molecular dynamics simulation. Out of this we gained the results which are summarized in table 7.

Table 7: Constants for the parametrization of the dipole code

parameter	numerical value
C_1	-45meV
C_2	1096meV
C_3	-9meV
ϵ_r	6.5
\mathbf{p}	2.23D
lattice parameters	
\mathbf{a}	$6.3115(2)\text{\AA}$
\mathbf{b}	$6.3115(2)\text{\AA}$
\mathbf{c}	$6.3161(2)\text{\AA}$

The lattice parameters can be varied if desired but in this thesis all the minimizations which were performed with the Monte Carlo approach were done with the lattice parameters of table 7. With this set of parameters one is able to describe the organo halide perovskite system at 300K in a satisfactory way. It should be noted the parametrization which is shown in table 7 is based solely on the $6 \times 6 \times 6$ ab-initio simulation. This was done like that beacuse the $6 \times 6 \times 6$ simulation shows the best statistics when considering the polarplot which is the basis for the Boltzmann inversion.

5.5 Monte Carlo model

5.5.1 Single Layer Simulations

In first tests of our Monte Carlo code we tried to reproduce the results from Frost et al [17]. They made a two dimensional Monte Carlo approach and calculated $10 \times 10 \times 1$ grids at temperatures of: $0K$, $100K$, $300K$, $1000K$. We tried to take a three dimensional Monte Carlo approach, with a single layer and check if the results differ from an approach that is purely two dimensional. The dipoles in our simulation will be able to rotate out of this plane, although our grid is two dimensional and we check how this influences the results. For this simulation we only took pure dipole-dipole interactions into account. This means all the cage interaction parameters were set to zero and therefore in the used Hamiltonian only the second sum of equation 5.18 was used.

First figure 5.41 shows a $10 \times 10 \times 1$ layer at $0K$. One can see that at $0K$ ferroelectric stripes form. Neighbouring stripes are always oriented anti-aligned because in this way every positive charge is surrounded directly only by negative charges and every negative charge is enclosed only by positive atoms. This behaviour is called anti-ferroelectric

ordering. It follows, this is the same result which one would expect for a two dimensional dipole grid at $0K$.

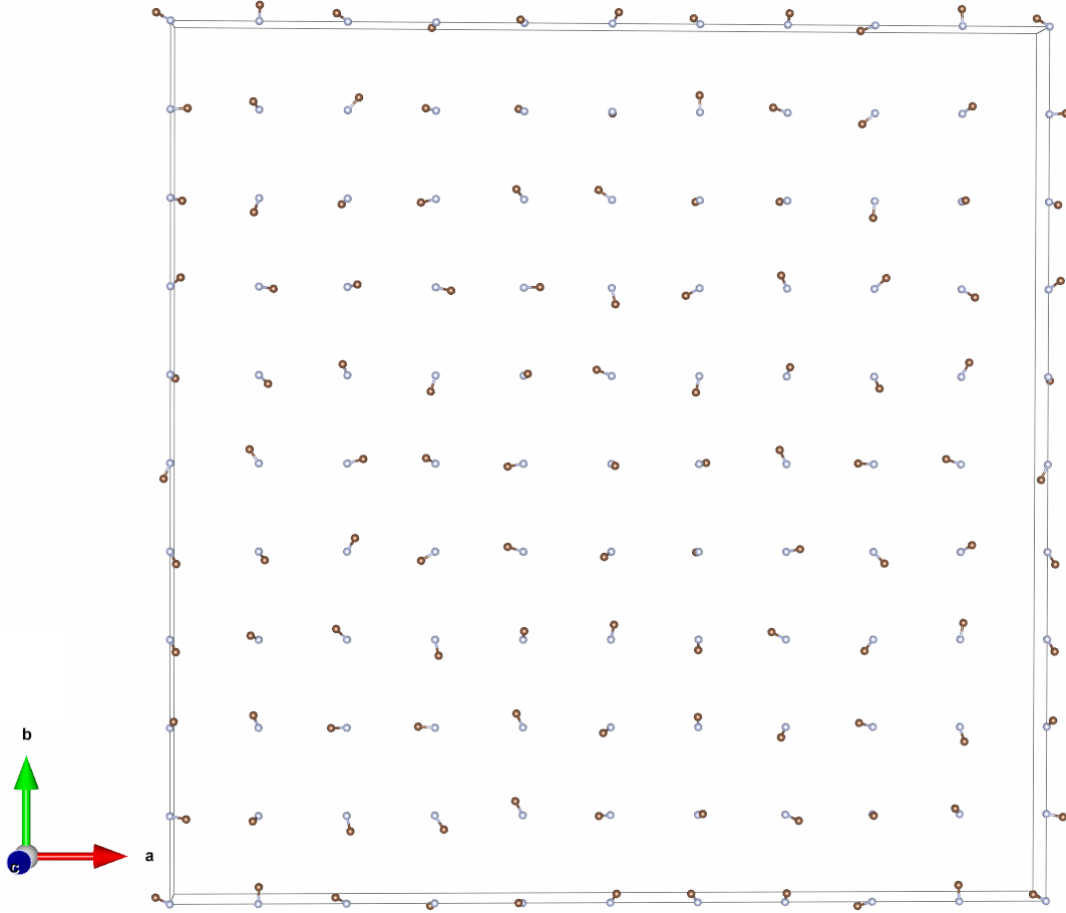
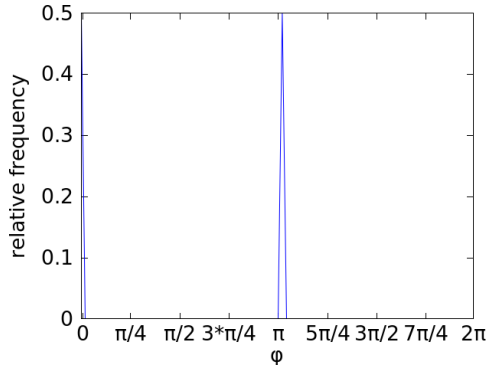
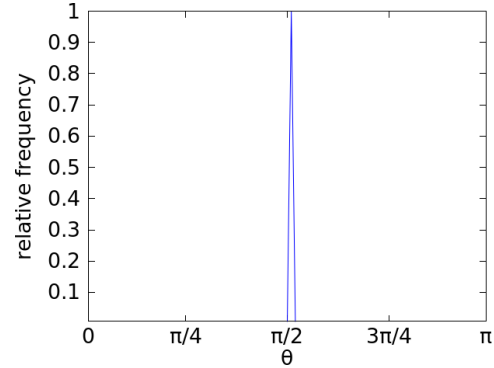


Figure 5.41: Single $10 \times 10 \times 1$ dipole layer at $0K$

Next in figure 5.42 the same grid but now at $300K$ is shown. As one can see the dipoles will not point only in the \mathbf{xy} plane but in \mathbf{z} direction as well. If the thermal energy is sufficient, the dipoles will not only orient parallel to the layer but they will rotate in the three dimensional space. This will be considered in more detail by the histograms for the spherical angles of the dipoles.

Figures 5.43 and 5.44 show the relative distribution of the angles in the considered systems. The distribution of angle φ shows the mean rotation of the dipoles in the \mathbf{xy} plane. Next figure 5.44 shows the distribution of the angle with respect to the \mathbf{z} axes. As one can see in the plot for the azimuthal angle φ the peaks at 0 and π represent alignment (0) or anti-alignment (π) with the \mathbf{x} axes. One is able to observe that at $0K$ layer a two dimensional approach is a very good approximation. The most favourable orientation for the dipoles is in the plane which is spanned by the \mathbf{x} and \mathbf{y} lattice vectors.

Next we will investigate the $100K$ structure shown in figures 5.45 and 5.46. We observe already at $100K$, the dipoles will not take the structure of aligned and anti-aligned stripes in the \mathbf{xy} plane. This is the case even if the thermal energy is still lower than the dipole-dipole interaction energy. The distribution of the azimuthal angle in figure 5.45 shows an equally likely probability for every orientation of the organic dipole in the \mathbf{xy} plane. Next considering the histogram θ which determines if the dipoles are located in the \mathbf{xy} plane or if they are more likely oriented along the \mathbf{z} axes. Like shown in figure 5.46 there

Figure 5.42: Single $10 \times 10 \times 1$ dipole layer at 300KFigure 5.43: φ histogram for a single layer 0K structureFigure 5.44: θ histogram for a single layer 0K structure

is no preferred orientation for the dipole in this direction too. Therefore the thermal energy is already at 100K sufficiently large to overcome the arrangement of the dipoles in the plane. We conclude, the two dimensional approach yields only reasonable results for temperatures of 0K and very slightly above, even if there are no interaction partners in the z direction; a two dimensional approach is not able to represent the behaviour of three dimensional dipole grids even if one considers a single layer.

By increasing the temperature further to 300K the distribution of both the azimuthal

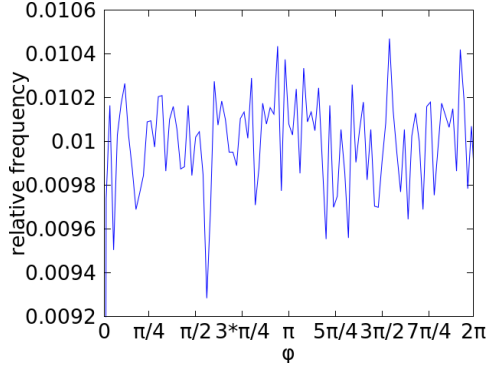


Figure 5.45: φ histogram for a single layer 100K structure

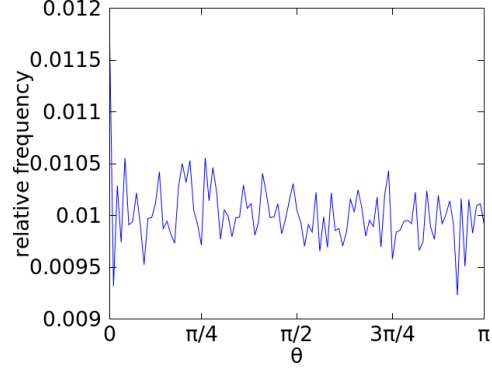


Figure 5.46: θ histogram for a single layer 100K structure

and the polar angle get flat too, as can be seen in figures 5.47 and 5.48. At 300K the interaction energy between the dipoles and the thermal energy are equal [17]. This means that all the different orientations are now accessible for the dipoles because the rotational barrier is now dominated by thermal energy. The same is true for the spherical angle θ . Again we conclude if the temperature is sufficiently high the dipole-dipole interaction will play a minor role for the system. One is able to say that already at very small temperatures of around 100K the thermal energy fluctuations (entropy) will be very important.

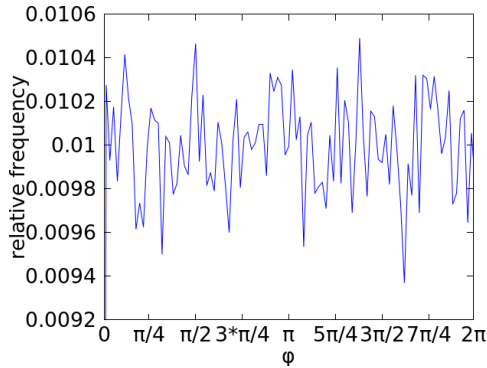


Figure 5.47: φ histogram for a single layer 300K structure

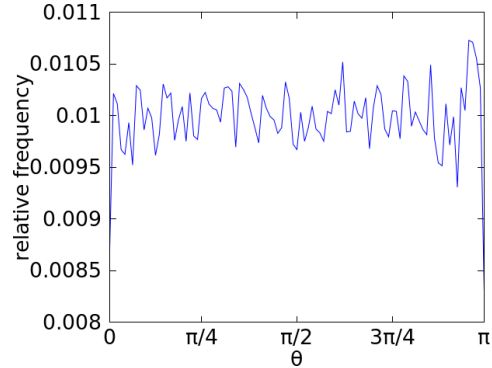


Figure 5.48: θ histogram for a single layer 300K structure

5.5.2 Comparing ab- initio molecular dynamics results with Monte Carlo results

For the comparison of the Monte Carlo code with the ab- initio molecular dynamics simulation, we equilibrated a $40 \times 40 \times 40$ cell with parameters from table 7. The system's temperature was set to 300K and the cut off radius was chosen in a way to only take into account the nearest neighbours.

Figure 5.49 shows the histogram for the results from the Monte Carlo approach (blue line) and for the ab-initio molecular dynamics (red line) in one plot. The curves do not coincide in a perfect way but the Monte Carlo code reproduces the periodicity in the direction of the spherical angle θ well. We did not try to model the linear slope because it has no physical origin. This slope is an artefact of the small cell and insufficient equilibration.

Figure 5.50 shows the histograms for the azimuthal angle φ including the Monte Carlo

approach (blue line) and the molecular dynamics (red line) in one single plot. One is able to see that the peaks at 0 and 2π are very similar and recall that this is the same peak because 0 and 2π denote the same angle (alignment with the positive \mathbf{x} axis). Moreover the peaks at $\frac{3\pi}{2}$ coincide very well too. But the two remaining peaks at $\frac{\pi}{2}$ and π describe the behaviour of the ab- initio molecular dynamics simulation not so well. The peak at the right hand side is larger in the case of the Monte Carlo approach and for the left peak the behaviour is vice versa. We expect that this is caused by additional cage dipole interactions which are not yet taken into account. It follows, with the cage-dipole interaction terms we are able to reproduce the symmetry of the considered perovskite system.

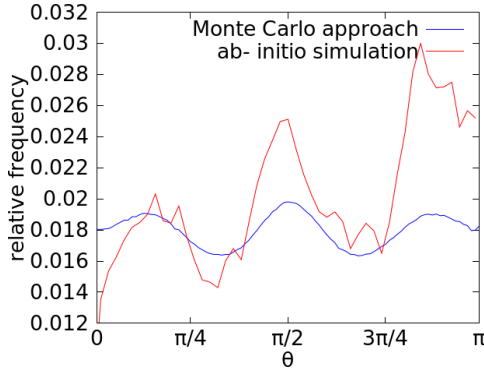


Figure 5.49: θ histogram for a $40 \times 40 \times 40$ cell and ab initio- molecular dynamics ($6 \times 6 \times 6$) at 300K

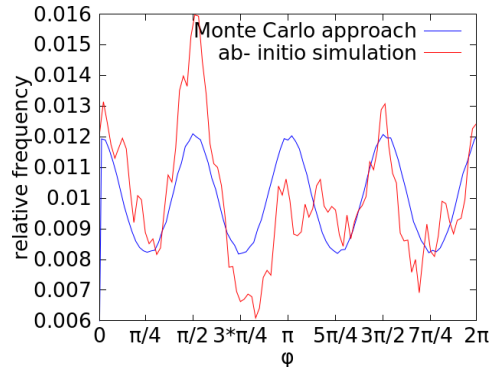


Figure 5.50: φ histogram for a $40 \times 40 \times 40$ cell and ab initio- molecular dynamics ($6 \times 6 \times 6$) at 300K

Next we want to show the agreement of the relative orientations of the dipoles with respect to their nearest neighbours. In figure 5.51 we see a histogram for the dot product of a certain dipole with its nearest neighbours as they were shown before. One is able to see that the two curves coincide very well. There is only a slight overestimation by the Monte Carlo approach for the anti aligned configuration of the nearest neighbours and on the other hand the Monte Carlo approach underestimates the region around 0.3 slightly which corresponds to an angle between the considered dipoles of approximately $\frac{\pi}{2}$. These shortcomings will also be caused by cage-dipole interactions which were neglected in the foregoing terms. The coordination spheres of higher order were also considered like described in section 5.2.6. Although if the first coordination sphere looks very similar to the one of the molecular dynamics simulation the second and the third coordination spheres show a largely random distribution. From this it follows we are able to regain the effects caused by the nearest neighbours but with the applied terms we are not yet able to describe the long range order of the perovskite system.

Last we want to show the collective behaviour of all these terms at 300K by presenting the polar plot of the considered $40 \times 40 \times 40$ system which can be seen in figure 5.52. At a first glance this plot seems to be different compared to the polar plots gained out from the molecular dynamics discussed before. But if one looks carefully one is able to see that we are able to reproduce the 8 minima in the area of the graph. From this it follows that we are able to reproduce the periodic interactions between the dipoles but also the interaction among an organic cation and the inorganic framework surrounding it in the spherical directions θ and φ reasonably well.

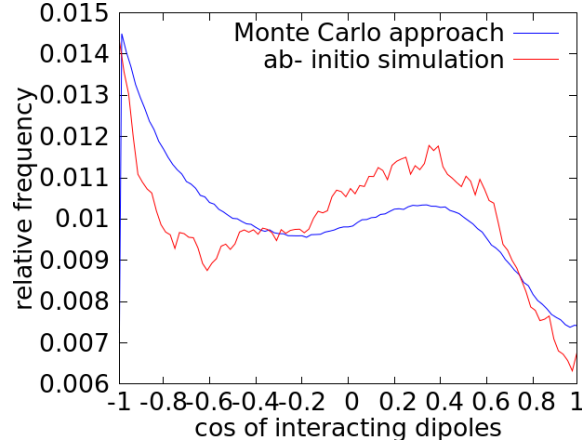


Figure 5.51: Histogram for the dot product of dipole vectors for a $40 \times 40 \times 40$ and ab initio- molecular dynamics ($6 \times 6 \times 6$) at 300K

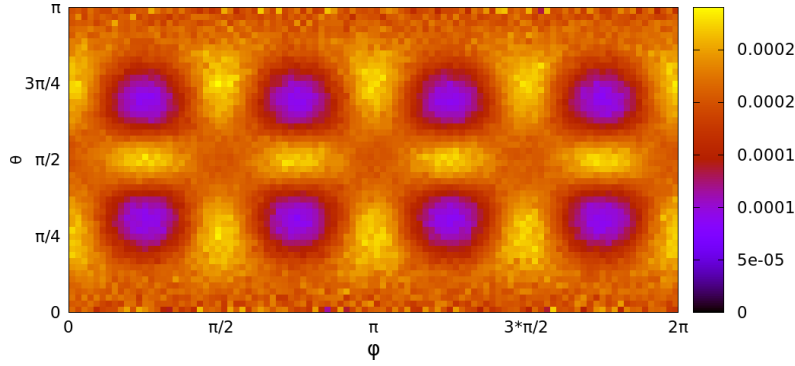


Figure 5.52: Polar plot of the orientation of the dipoles in the $40 \times 40 \times 40$ system in spherical coordinates at 300K using the full model Hamiltonian

Last we briefly show the result that one would get if there were no additional strains applied on the CH_3NH_3 molecules by the cage. The corresponding results are shown in figure 5.53. Here only the dipole-dipole interactions are considered. Some contributions of the cages are included implicitly by the dielectric constant though. As one can see, one obtains a homogeneous distribution of the orientations of the dipoles. This is caused by the very high temperature of 300K which dominates over the dipole-dipole interactions. This is the reason why this plot is smeared out over the entire layer. But out of this it follows that the interplay of the inorganic framework will be very important for the structural properties of the considered system. The inorganic framework will be essential to determine how the dipoles orient during the simulation.

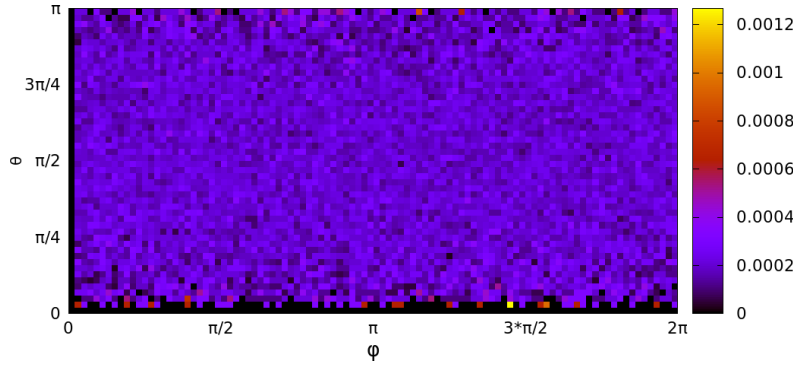


Figure 5.53: Polar plot of the orientation of the dipoles in the $40 \times 40 \times 40$ system in spherical coordinates without applied cage interactions

5.5.3 Comparing two $0K$ structures

In this section we are going to consider two $10 \times 10 \times 10$ simulations which were equilibrated at $0K$. The first simulation shows a structure with included dipole-dipole and cage-dipole interactions, the second simulation only takes dipole-dipole interactions into account. The parameters for both simulations were adjusted to the values shown in section 5.4. Figures 5.54 and 5.55 show the results of the simulation with included cage-dipole interactions. In the polar plot there are two spots, the first at $\varphi = \frac{\pi}{2}$ and $\theta = \frac{\pi}{4}$ which belongs to the face diagonal of the \mathbf{yz} plane. This spot therefore represents dipoles which are pointing in-between the positive \mathbf{y} and positive \mathbf{z} direction. Next there is a second spot at $\varphi = \frac{3\pi}{2}$ and $\theta = \frac{3\pi}{4}$. This spot represents dipoles which are too oriented in the \mathbf{yz} plane but pointing in the opposite direction. Therefore the dipoles which are causing this spot point in-between the negative \mathbf{y} and negative \mathbf{z} axes. Because we are using a cubic cell there are several symmetry equivalent configurations which belong to the remaining face diagonals. Figure 5.55 shows the relative orientations of the dipoles with their nearest neighbours. There exists only one peak at -1 which belong to an angle of π between the dipoles. Therefore every molecule is surrounded only by dipoles which are oriented in the opposite direction. Hence one gets an anti ferroelectric structure. This behaviour is schematically represented in figure 5.56. It should be noted that in this figure the dipoles are not oriented along the face diagonals but along the principal axes, because only a dipole surrounded by oppositely oriented nearest neighbours should be shown.

It should be noted the \mathbf{z} is slightly longer than the \mathbf{x} or the \mathbf{y} axes which was shown in table 7. Therefore those face diagonals which include a \mathbf{z} component are energetically slightly favoured compared to, for example a system where the dipoles would be oriented along the face diagonals of the \mathbf{xy} plane. Table 8 summarizes energies of $4 \times 4 \times 4$ cells where the dipoles align and anti-align to the direction which is shown in the left hand side column of the table. This simulations were also carried out with the parameter set of table 7 but in the perfect cubic case the \mathbf{z} axes was adjusted to the length of the \mathbf{x} and \mathbf{y} axes. Now considering the second column it makes no difference if the dipoles align and anti-align along the \mathbf{x} , \mathbf{y} or the \mathbf{z} axes. The same is true for the face diagonals. It follows, in the perfect cubic case the dipoles will always orient along any face diagonal and form an anti ferroelectric pattern. In the pseudo cubic case the degeneracy of the \mathbf{x} , \mathbf{y} and \mathbf{z} directions breaks because now the \mathbf{z} axes is slightly longer. As a result, the molecules will more likely align or anti align to one of the face diagonals which contain the \mathbf{z} axes. This behaviour is shown in table 8 in the third column, where the face diagonals

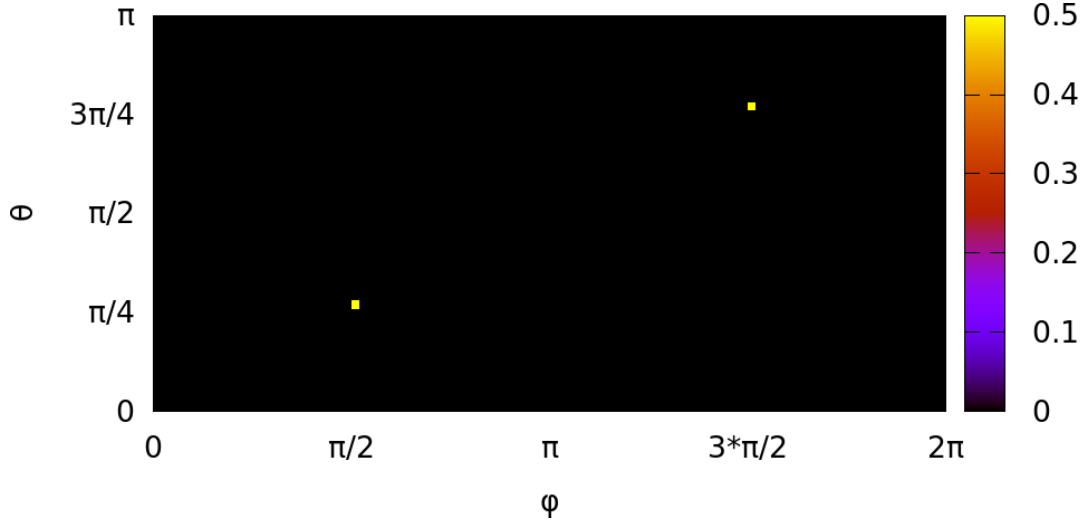


Figure 5.54: Polarplot of a $10 \times 10 \times 10$ structure at 0K, with included cage-dipole interactions

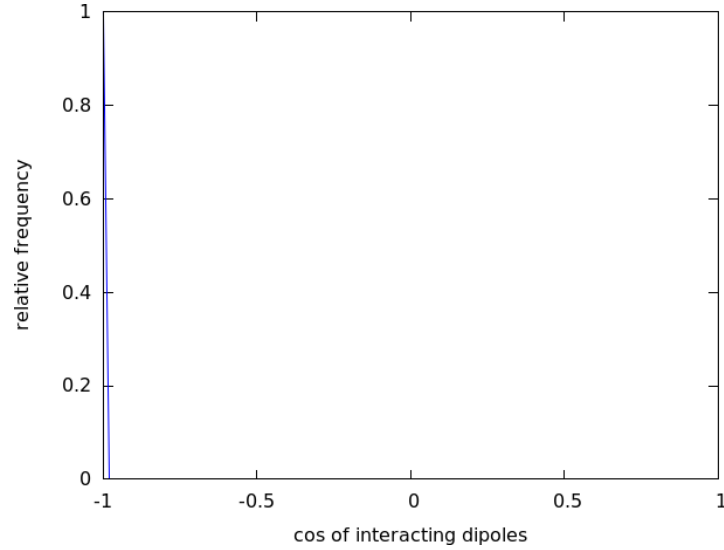


Figure 5.55: Relative orientations of organic molecules in a $10 \times 10 \times 10$ cell at 0K, with included cage-dipole interactions

that include the \mathbf{z} direction are lowered in energy about a value of 0.15meV. As a result the configurations with the lowest energies for this parametrization are point dipole grids where the organic molecules are oriented either along \mathbf{xz} and $-\mathbf{x} - \mathbf{z}$, $\mathbf{x} - \mathbf{z}$ and $-\mathbf{xz}, \mathbf{yz}$ and $-\mathbf{y} - \mathbf{z}$ or $\mathbf{y} - \mathbf{z}$ and $-\mathbf{yz}$.

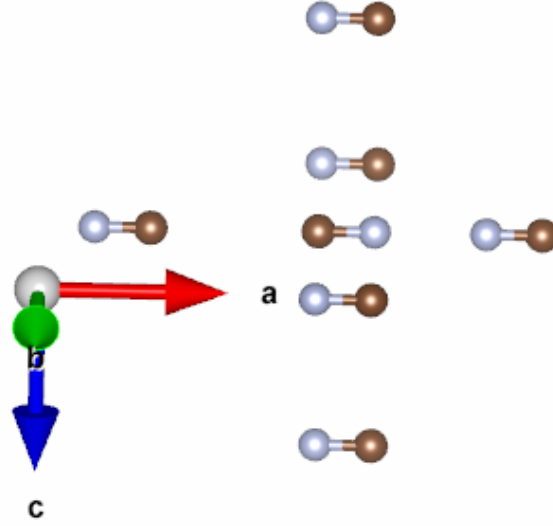


Figure 5.56: Dipole surrounded by anti-aligned nearest neighbours like it is the case in the 0K structure of the Monte Carlo model

Table 8: Energies of systems with different dipole orientations (cage-dipole interactions included)

orientation	perfect cubic [meV]	pseudo-cubic [meV]
x	-750.035	-749.937
y	-750.035	-749.937
z	-750.035	-749.838
xy	-2088.000	-2087.901
xz	-2088.000	-2088.049
yz	-2088.000	-2088.049
xyz	182.519	182.519

Next figures 5.57 and 5.58 show the results from the simulation where the cage-dipole interactions were not included. The polarplot shows two spots, one at $\varphi = \frac{\pi}{2}$ and $\theta = \frac{\pi}{2}$ which denotes the **y** direction in Cartesian coordinates and the other at, $\varphi = \frac{3\pi}{2}$ and $\theta = \frac{\pi}{2}$ which denotes the **-y** direction. Therefore the dipoles align and anti align according to one of the principal axes in the minimum energy structure at 0K. This arrangement results in relative dipole orientations like they are shown in the histogram of figure 5.58. There are two peaks one at -1 and the other at 1 . This belongs to relative angles between the dipoles of either π (anti aligned) or 0 (aligned). This behaviour was already shown for single layers in figure 5.5.1. Therefore a certain dipole is surrounded by four anti aligned nearest neighbours and two nearest neighbours which align with the dipole. This is a result of the anti ferroelectric stripes which form in a point dipole grid at 0K.

Last we also considered the difference of a perfectly cubic system and a pseudo-cubic system. The results of this analysis are shown in table 9. Like one can see in the perfectly cubic case it does not matter along which axes the stripe formation occurs. Without the parametrization the face diagonals are higher in energy than the principal axes. In this case also the room diagonal shows the same energy as the face diagonals which was not the case when considering the results with included cage-dipole interactions. Next we also calculated the results for the case when the **z** axes is slightly longer than the **x** or **y**. In this case the configurations where the stripes form along the principal axes are also the

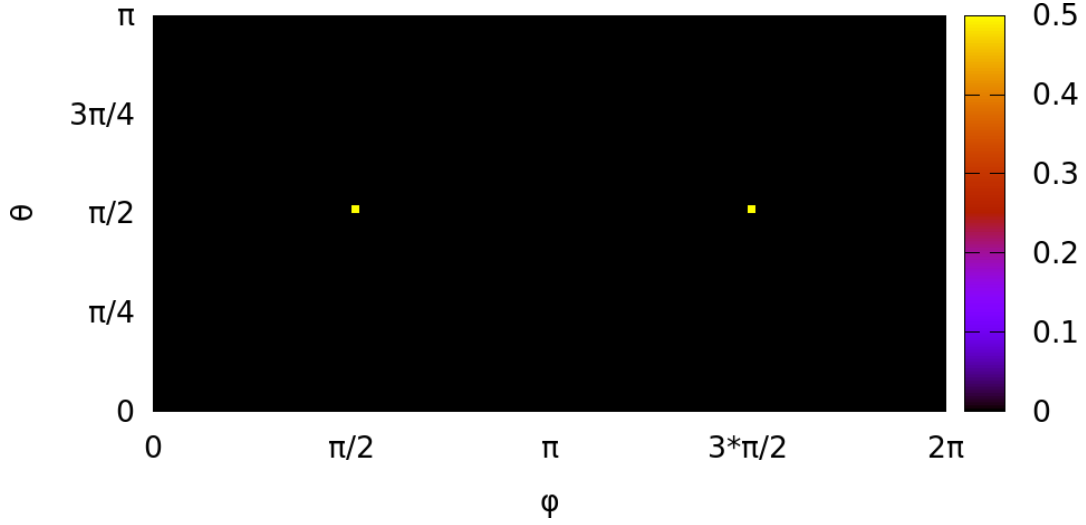


Figure 5.57: Polarplot of a $10 \times 10 \times 10$ structure at 0K, only dipole-dipole interactions included

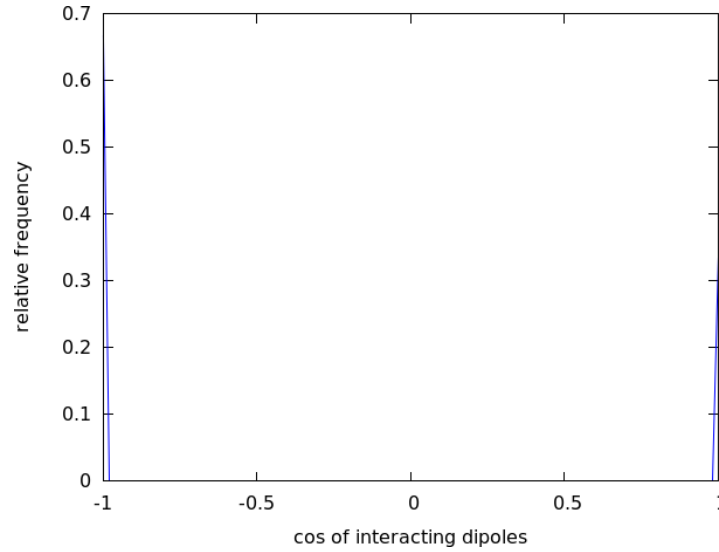


Figure 5.58: Relative orientations of organic molecules in a $10 \times 10 \times 10$ cell at 0K, only dipole-dipole interactions included

energetically most favourable. But now the configuration where the stripes form along the z axes is slightly higher in energy. Therefore the most favourable structures are those where the dipoles are oriented in the xy plane along the x and $-x$ or the y and $-y$

Table 9: Energies of systems with different dipole orientations (only dipole-dipole interactions included)

orientation	perfect cubic [meV]	pseudo-cubic [meV]
x	-174.035	-173.937
y	-174.035	-173.937
z	-174.035	-173.838
xy	0.000	0.098
xz	0.000	-0.049
yz	0.000	-0.049
xyz	0.000	-0.980

As a result the interactions of the cage atoms with the organic cations dominate the arrangement of the dipoles within the perovskite cell and the dipole-dipole interactions will only play a subordinated role.

5.5.4 Calculating hysteresis of polarization when applying an electric field

The simulation described in this section was done using the cage dipole interaction parameters like they were discussed in section 5.4. The size of the cell was taken as 35 dipoles in every direction and therefore a total number of 42875 dipoles. The temperature of the system was adjusted to 300K. First we relaxed a structure without applying any field to gain an appropriate starting structure. With this relaxed structure we applied an electric field stepwise in the negative \mathbf{x} direction until we reached the first turning point which is the maximal field applied in negative \mathbf{x} direction. At this point two sweeps over any dipole in the supercell were performed. Then the field was diminished until one reaches zero again. From this we invested now a field in the direction of the positive \mathbf{x} axes until we reached the turning point on the other side where we performed two sweeps over any dipole again. Next the field was diminished again until one reaches zero. These cycles were performed 20 times. The results can be seen in figures 5.59 to 5.62. The polarization which is shown in these figures is calculated according to equation (5.12). The figures show a decreasing width of the hysteresis curve which is caused by the number of minimization steps performed for every field strength. The first figure shows a curve where every dipole was flipped once per minimization step, the second figure shows a graph where every dipole was swept twice, the third figure shows a simulation where every dipole was able to change its orientation three times and in the last figure every dipole was allowed to flip four times. The first three hysteresis cycles are not included in the figures because they were not properly relaxed. It is interesting the hysteresis diminishes to nearly one single line already at 4 steps per dipole.

The upper part of the curve belongs to the part of the simulation when the field is decreased from the maximum electric field applied in negative \mathbf{x} direction. And the lower part of the curve is if one goes from the maximum applied field in positive \mathbf{x} direction towards the negative maximum field. The field strengths which are shown in these plots are very huge and do not correspond to the usual field strengths when operating perovskite systems. We also tried to obtain such curves for lower or moderate field strengths but then we did not obtain hysteresis curves. If the fields are that small the curve when increasing the field strength in the positive direction overlaps with the part of the curve when stepwise applying the field in the negative direction. The hysteresis of a material is very strongly influenced by the relaxation time at every step of the cycle. The longer the relaxation time for every step the smaller the distance between the two parts of the hysteresis curve. This is also true for the number of relaxation steps performed during the simulation for every field strength. If all the dipoles would be perfectly aligned the mean normalized polarization would result in a value of one which is not the case in any of the shown figures. To archive this perfectly aligned structures one would have to perform more minimization steps at the turning points of the hysteresis curve. Therefore in the case of the simulation where 4 Monte Carlo steps per dipoles per field strength were performed, every dipole has only 4 times the chance to reach the anti-aligned configuration with respect to the applied field. To obtain values comparable with experiment one has to multiply by the number of dipoles, multiply by the dipole moment of the considered species and last divide by the volume of the cell which reads as 9879273663 \AA^3 ($9.889 * 10^{21} \text{ m}^3$). Out of the hysteresis curve we are able to calculate the remanent polarisation which can be seen in table 10.

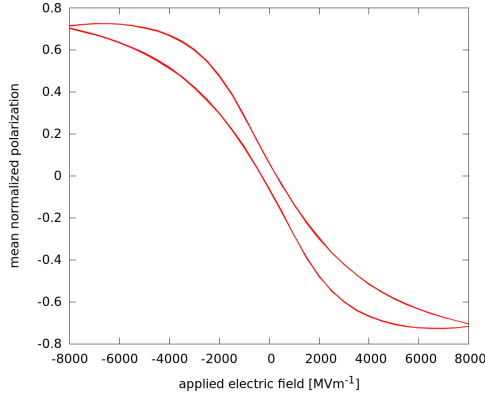


Figure 5.59: Mean normalized polarization of a $35 \times 35 \times 35$ cell vs applied electric field (1 minimization step per dipole)

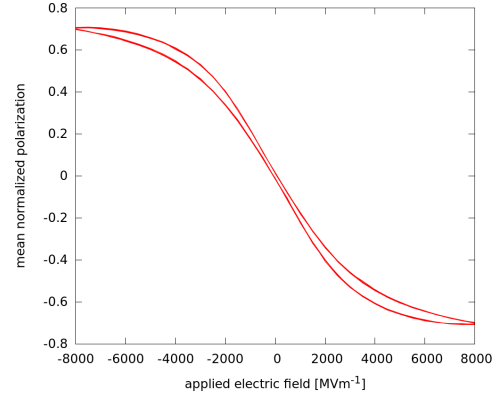


Figure 5.60: Mean normalized polarization of a $35 \times 35 \times 35$ cell vs applied electric field (2 minimization steps per dipole)

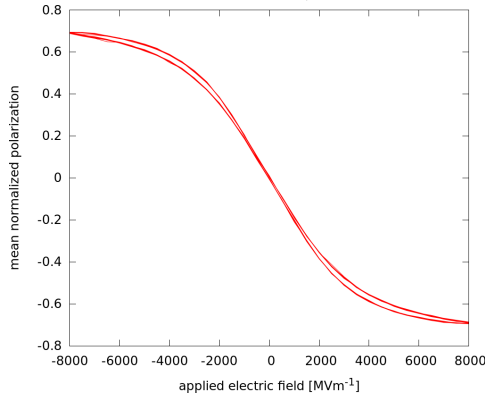


Figure 5.61: Mean normalized polarization of a $35 \times 35 \times 35$ cell vs applied electric field (3 minimization steps per dipole)

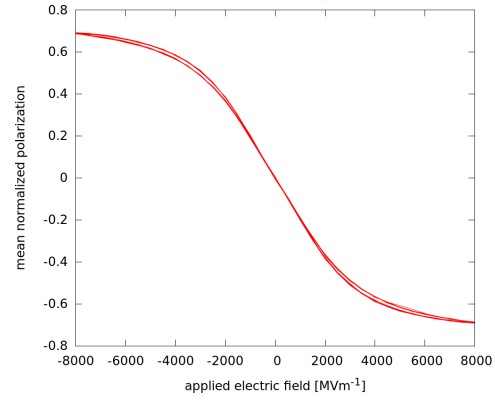


Figure 5.62: Mean normalized polarization of a $35 \times 35 \times 35$ cell vs applied electric field (4 minimization steps per dipole)

The values are decreasing with an increasing number of minimization steps per cycle and they are converging to a threshold value.

Table 10: Remanent polarization for different number of minimizations steps

number of minimization steps per dipole	remanent polarization [Cm^{-2}]
1	$1.978 * 10^{-09}$
2	$4.301 * 10^{-10}$
3	$1.787 * 10^{-10}$
4	$9.035 * 10^{-11}$
5	$5.398 * 10^{-11}$
6	$5.850 * 10^{-11}$

Next we calculated the polarizability of the considered perovskite system which is determined by the slope of the hysteresis loops. This slope was the same for all of the simulated hysteresis curves except for insignificant decimal places. The polarizability can be written as $6.232 * 10^{-12}[Cm^{-2}]$. Till now there were no experimental papers that are comparable with the values gained here. There exists a paper by Coll et.al. [11] where they determined hysteresis loops experimentally for methyl- ammonium lead iodine perovskite materials but unfortunately they only reported the applied voltage and no thickness of the sample and so one is not able to determine the electric field which was applied to the sample. However the hysteresis loops in the experimental paper look very similar to our shape.

5.5.5 Local Polarisation which arises due to the dipole contribution

To consider the local mean normalized polarization of the considered perovskite system a $30 \times 30 \times 30$ structure was equilibrated at 300K. To do this the cell was divided into subsystems and for each the mean normalised polarisation was calculated according to equation 5.12. The parameters for applying the cage interaction were taken as determined before. Then an algorithm was used to divide the system in any desired number of smaller subsystems. In this case the subsystems were chosen each with 25 organic molecules inside. The subsystems can be considered as cubic boxes with 5 dipoles in every space direction. Next the mean normalized polarization like it was shown in equation 5.12 was calculated for every subsystem. The large $30 \times 30 \times 30$ cell is therefore divided into 216 subsystems. Next we have cut this big $30 \times 30 \times 30$ cell in slices for example along the x axis and these slices are also 5 dipoles thick and one will obtain 6 slices along the whole cell. Every slice is now composed of 36 of the before mentioned sub cells and this can be done for every direction of space. The results are shown in figure 5.65 to figure 5.67 where the colour represents the net mean normalized polarization of the considered sub cell and the little white vectors on top of every sub cell show the associated polarization vector where the component orthogonal to the considered plane is neglected.

Out of these plots one is able to see that there are a lot of small polarized domains present in the perovskite system. Again we mention here that only the contributions due to the organic molecules are considered. The smallest of these domains are at least only one sub cell big. But there are also agglomerates of such sub cells present. The biggest of those accumulated polarization areas are at least 14 sub cells big. Remarkably, it seems like the domains with lower mean normalized polarization (those with a purple colour scale) accumulate more often than those with higher polarization. Therefore these are the sub cells with very low to nearly no net polarization.

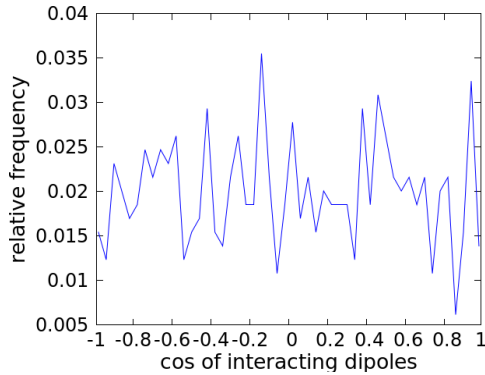


Figure 5.63: Histogram of dot product of a certain mean normalized polarization vector of a certain sub cell with the vectors of the adjoining sub cells

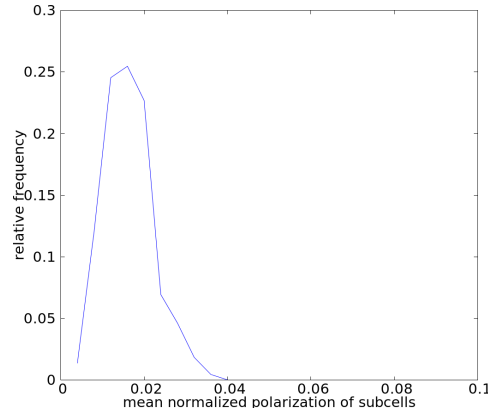


Figure 5.64: Histogram for the mean normalized polarization of all sub cells present in the considered system

To find some kind of dependence of the polarization vector of a certain sub cell on its neighbouring sub cells we calculated the dot product of the mean normalized polarization vector of a certain sub cell with polarization vectors of the nearest neighbour sub cells. Therefore every cell has 6 nearest neighbours because the sub cells were chosen cubic. As one can see in the graphic there is no favoured orientation between adjacent polarization vectors. The only exception would be the peak for the aligned vectors but it is too small

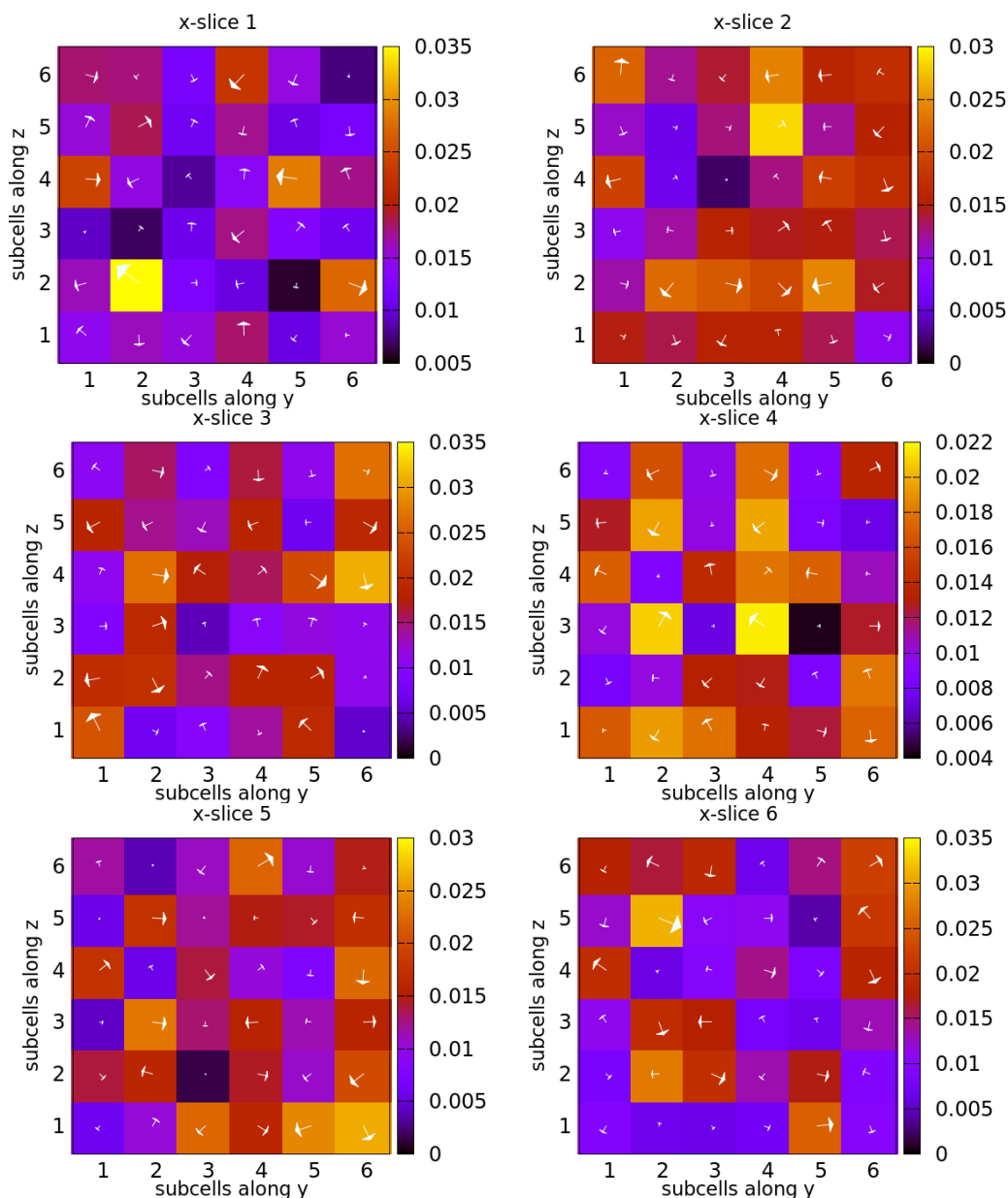


Figure 5.65: Colormap of mean normalized polarisation in the yz plane of a $30 \times 30 \times 30$ system which was cut in slices along x , the arrows denote the $2D$ polarization vectors where the x component is neglected

to be really taken into account. The reason for this is the high temperature of 300K at which this system has been considered because the thermal energy makes all rotational states of the organic molecules accessible. The last figure (5.64) of this chapter shows whether there is some kind of preferred polarization state of the considered sub systems. This was calculated by taking the mean normalized polarization vectors of the subsystems and counting them by binning. One is able to see the distribution peaks around 0.02. As mentioned before, if the mean normalized polarization vector has a value of one, the system is totally polarized and a value of zero suggests there is no net polarization present. It should also be mentioned that this peak is very narrow compared to the accessible values between zero and one the polarization could in principle take. So all the subsystems lie in

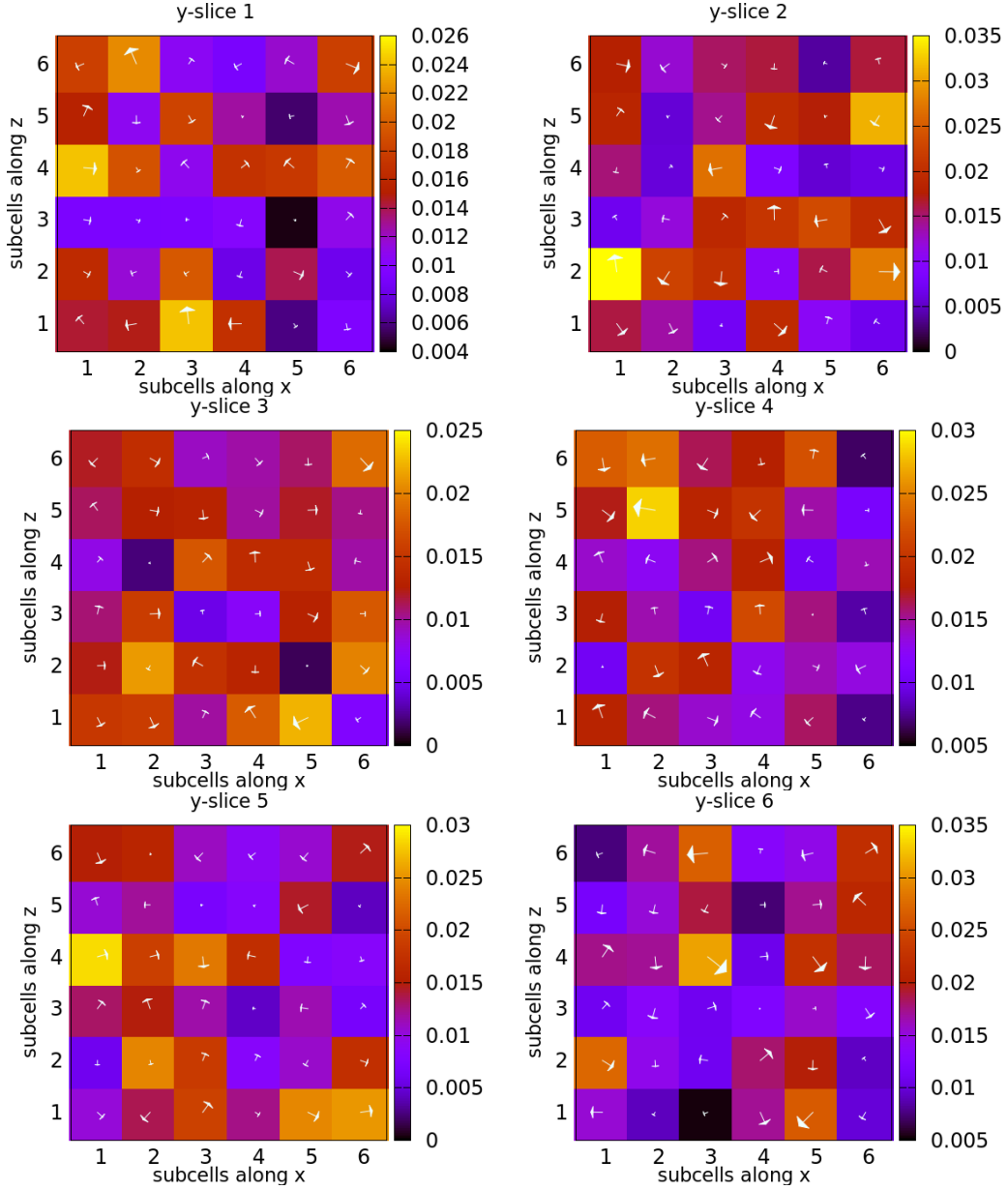


Figure 5.66: Colormap of mean normalized polarisation in the xz plane of a $30 \times 30 \times 30$ system which was cut in slices along y , the arrows denote the 2D polarization vectors where the y component is neglected

this certain range. This also explains why it seems that the purple areas would accumulate more often than others, but the reason is just they occur more often.

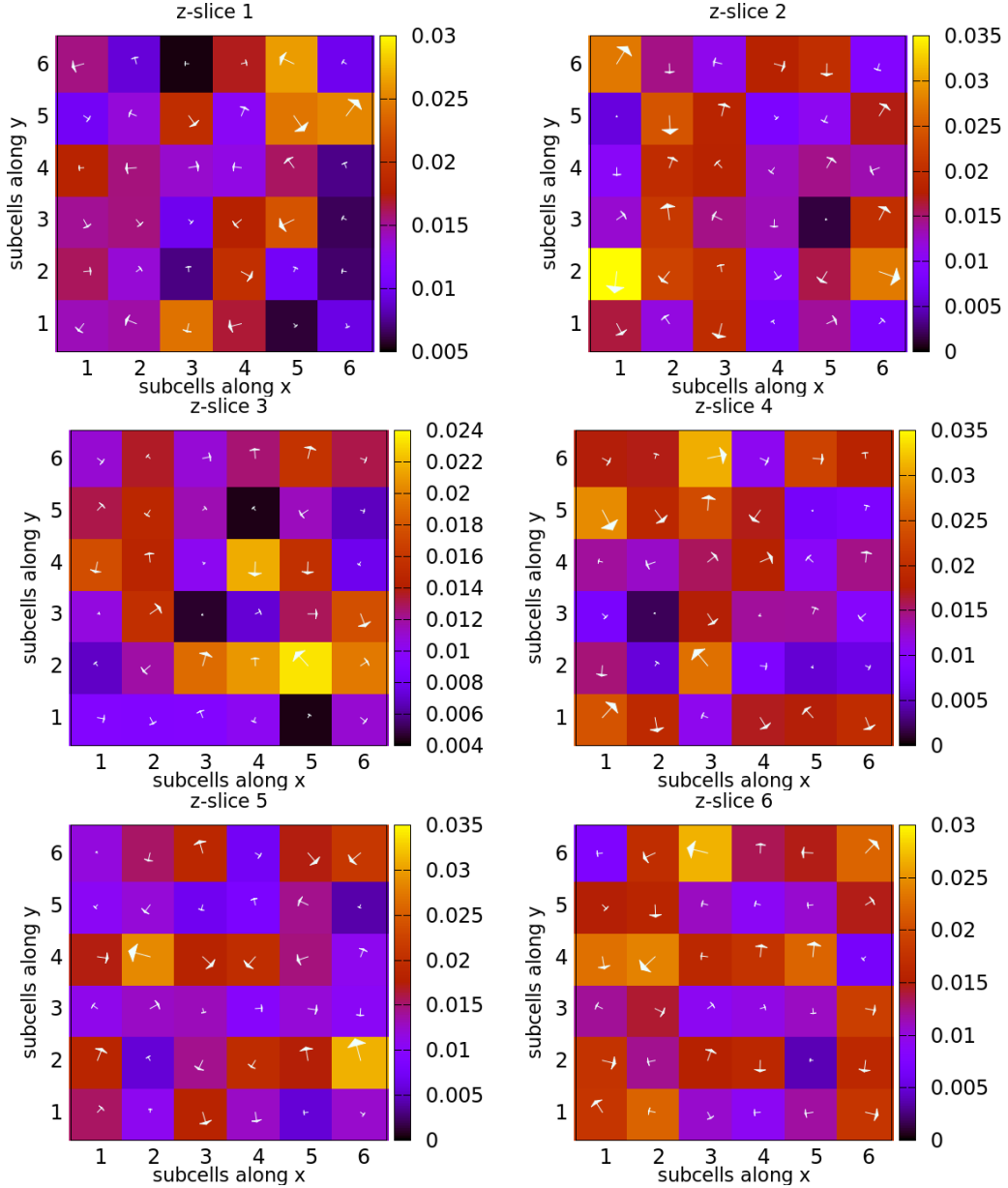


Figure 5.67: Colormap of mean normalized polarisation in the xy plane of a $30 \times 30 \times 30$ system which was cut in slices along z , the arrows denote the 2D polarization vectors where the z component is neglected

5.5.6 Temperature dependence of Polarization

The influence of the temperature on the mean normalized polarization was investigated by equilibrating $10 \times 10 \times 10$ once with the parameters to resemble the cage interactions and the other time without applying any cage interactions. For low temperatures up to about 50K it was no problem to calculate the mean normalized polarization. But for higher temperatures the values had a remarkably spread. To get appropriate mean values 1000 independent calculations were taken to calculate the mean normalized polarization for a certain temperature. This resulted in values which one is able to reproduce within a variance of $2 * 10^{-6}$. The variance is dimensionless because we calculated the mean

normalized polarization which is dimensionless (see equation (5.12)). The results of these calculations are summarized in figure 5.68. The temperature steps were 25K between 0K and 300K. The blue curve denotes the simulation with dipole-dipole interactions only and the green graph takes into account the cage-dipole interactions as well. First considering the graph where only dipole-dipole interactions were included. There is no net polarization at 0K because of the formation of the anti ferroelectric stripes which were shown in sections 5.5.1. By raising the temperature the dipoles gain thermal energy sufficient to leave the 0K minimum structure and possess configurations which show a net polarization as well. By considering figure 5.68 the mean normalized polarization slightly increases at the beginning (when leaving the anti ferroelectric minimum structure) and then starts fluctuating around a mean value of 0.0014 with a variance of 3.697×10^{-07} . Therefore one is able to say the polarization of a dipole grid only shows temperature dependence at very low temperatures and afterwards by raising the temperature further the polarization starts fluctuating around a certain value.

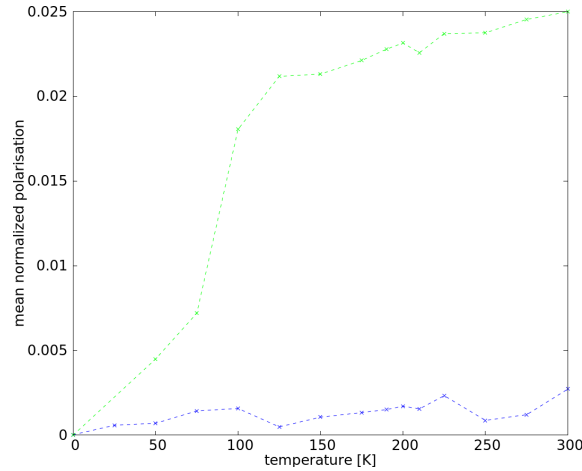


Figure 5.68: polarization vs temperature calculated by Monte Carlo approach (—) dipole-dipole interactions only and (—) cage-dipole interactions included as well

Next we are going to consider the dependence of the mean polarized polarisation on temperature for a simulation where the cage-dipole interactions are included as well. At 0K the 0K structure also possesses no net polarization because of the anti ferroelectric ordering which was shown in section 5.5.3. Again by raising the temperature the organic molecules will possess thermal energy and start to leave their global minimum at 0K which can be seen in figure 5.69. In this figure the dipoles are still in their minimum configuration but the thermal energy is already sufficient to smear the spot for the perfect orientation. This is the reason for the increasing mean normalized polarization at the beginning of the temperature curve shown in figure 5.68. At about 75K the curve shows a kink and the mean normalized polarization shows a stronger dependence on temperature. The reason for this stronger temperature dependence is because now the thermal energy is sufficient, so that the organic molecules are able to possess several of the minimum structures like they were shown in table 8. This means for example one has a certain cell where a certain part of the cell is in a configuration where the dipoles are oriented along the face diagonals $\mathbf{y} - \mathbf{z}$ and $-\mathbf{yz}$ and another part of the cell is in the configuration where the dipoles are oriented along $\mathbf{x} - \mathbf{z}$ and $-\mathbf{xz}$. Afterwards the the slope of the graph gets lower again which is caused by the fact that the thermal energy is now sufficient that the dipoles are able to smear out over the whole drawing layer expect for the area around the room

diagonals which are very unfavourable for the organic molecules. This behaviour of the organo-halide perovskite system is depicted by figure 5.70.

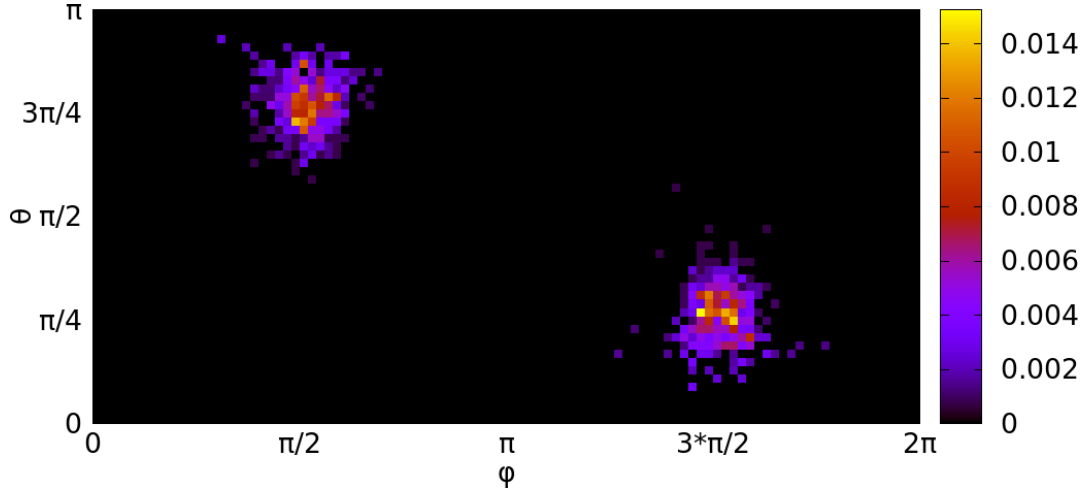


Figure 5.69: Polarplot of $10 \times 10 \times 10$ simulation with included cage-dipole interactions at 50K

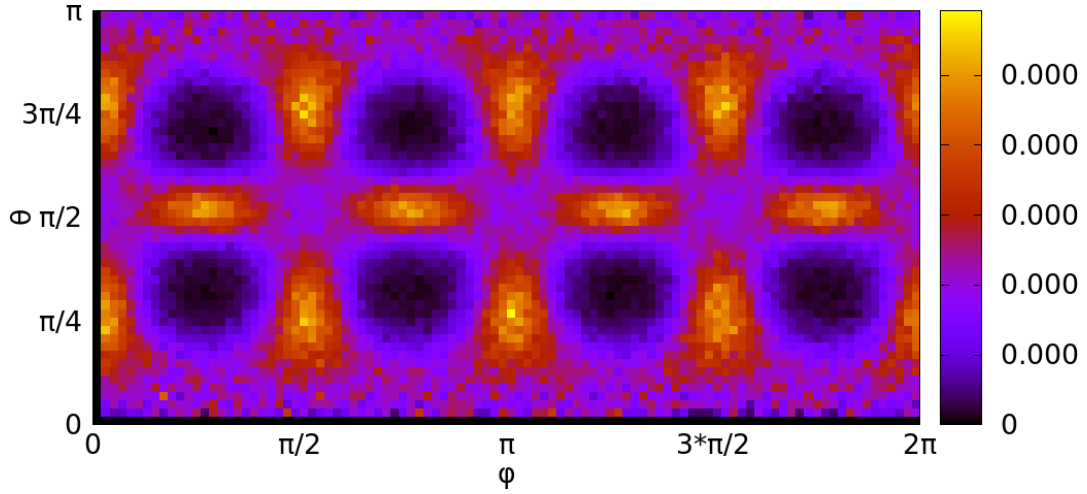


Figure 5.70: Polarplot of $10 \times 10 \times 10$ simulation with included cage-dipole interactions at 100K

6 Conclusion

The ab- initio molecular dynamics gave a direct insight on the dynamical behaviour of the considered organo- halide perovskite systems. One was able to see that the inorganic framework is very rigid during the whole simulation even at $300K$. It is only fluctuating around its equilibrium positions. On the other hand the dipoles are very flexible at $300K$ and nearly do not feel any rotational barrier because of the high thermal energy. Next we were able to see there exist special orientations which the dipoles will prefer compared to others. These orientations are chosen such that the positive charge of the organic cations is surrounded by the most accessible negatively charged iodine atoms. The orientation of the dipoles is therefore most likely chosen in a way that they are oriented along any of the face diagonals.

Next we tried to work out a model which is able to reproduce the mean results of the molecular dynamics simulations. This worked very nice and gave some insight in the structural behaviour of the dipoles. A very interesting feature of the perovskite solar cells which was shown by the Monte Carlo approach are the polarized domains which arise only due to the arrangement of the dipoles.

The problem with the Monte Carlo model is the inorganic framework which is only taken into account implicitly and therefore considered as completely rigid. This is a good approximation but the small fluctuations of the inorganic framework could influence the rotational state of the dipoles very strongly. The structures of the considered perovskites have some special properties: for example the ordering of the different coordination spheres which were discussed during this thesis. It is very important to consider the organo- halide perovskite system as a whole when considering its electronic behaviour. Because of the very special interplay between the cage atoms and the light organic molecules (cations). This special interaction of the framework with its locked dipoles has to be the reason for the special properties of the perovskite system. The next important thing is people are mostly interested in the high absorption efficiencies which may be described in terms of electronic structure which is not possible to describe by such a simple classical approach like the Monte Carlo ansatz shown here. Therefore the key to understand perovskite solar cells will be ab-initio calculations. The problem with those is that they are computationally very expensive and therefore it will be hard to calculate much bigger cells like than were already done. But it should be mentioned the properties of the system depend for small geometries very strong on the system size but if one reaches a certain volume of at least $4 \times 4 \times 4$ unit cells the properties do not change any more when going further to bigger systems which was seen in this thesis by comparing a $4 \times 4 \times 4$ and a $6 \times 6 \times 6$ super cell. Therefore it should be sufficient to deal with super cells in this size range.

Last the dependence of the mean normalized polarization on temperature gave also some interesting insight in the structural behaviour of the perovskite solar cells. This simulation suggested that there should be several different phases present in the cell at higher temperatures.

7 Outlook

There is still a lot of work to do in the field of the perovskite solar cells because the mechanism how the cell works exactly and why it absorbs light so effective is still not completely clear. It would also be very interesting to improve the Monte Carlo approximation further and determine temperature dependent parameters if necessary. This would give a fundamental insight in the ordering behaviour of the organic molecules at different temperatures. Further one would be able to develop more appropriate parameters for the interaction of the dipoles with their inorganic framework, maybe to model them in a way that thermal fluctuations of the cage atoms could be taken into account as well. This could maybe be implemented by applying parameters which fluctuate slightly by the use of random numbers. Finally it would be interesting to determine parameters which take into account the ordering behaviour of the second and third coordination spheres which could be carried out by using interaction terms which are only valid in a certain distance range from a certain dipole. Last it should be mentioned, it would be interesting to divide a huge system equilibrated under the use of the Monte Carlo ansatz at a moderate temperature in several subsystems and check if those subsystem possess their individual minimum configuration.

8 Appendix

8.1 Abstract

Perovskite solar cells have become very famous in the recent years within the photo voltaic community. The main reason for this is the high efficiencies that can be reached with those cells, the low costs and the ease in production. We investigated the behaviour of the organic cation to get a deeper understanding of those cells. Therefore we performed several ab-initio molecular dynamics simulations with varying cell sizes and two different exchange-correlation potentials. The used potentials were both PBEsol potentials one time with included dispersion interactions and the other without dispersion interactions. Out of these simulations the preferred mean orientations of the organic cations locked in the perovskite cages were extracted. From this one is able to see that the organic cations try to avoid the room diagonals within the perovskite cages. Next we determined a minimum cell size, which our analysis showed, should at least be $4 \times 4 \times 4$. This means that there should be 4 perovskite unit cells in every direction of space. In a smaller cell the characteristic pattern for the orientational distribution of the organic cations does not form. From this it follows the minimum cell size should at least contain 64 unit cells and hence 64 organic molecules. We considered autocorrelation functions for different cell sizes and different starting geometries. From this we concluded that random starting configurations equilibrate faster than aligned starting configurations. Additionally we also determined that the autocorrelation decreases slower for the potential with dispersion interactions included, because these increase the rotational barriers for the organic cations. Next we considered relative orientations of neighbouring organic molecules in different coordination spheres within the ab-initio molecular dynamics simulations. From this it follows that there exists a defined pattern for the dipoles relative to each other in the different coordination spheres. From this we deduce that there exists long range order in the considered halide organometal perovskite.

The second part of the ab-initio molecular dynamics simulations considered the behaviour of the inorganic framework during the simulations. Out of this we were able to conclude that the inorganic framework stays nearly rigid throughout the whole simulations. The only motion carried out by the inorganic framework are fluctuations around the equilibrium positions of the atoms. This behaviour is independent of the considered cell sizes and the considered potentials.

Out of these conclusions we tried to build up a Monte-Carlo model which should only take into account the organic cations. The parametrization for the energy calculation was carried out according to the Boltzmann inversion and the results obtained by the ab-initio molecular dynamics simulations. With this Monte-Carlo code we were able to simulate huge system sizes. With the Monte-Carlo approach we calculated local polarization effects, which showed small polarized domains in the system are present but the polarization of these domains is very small. Next we considered the dependence of the total polarization on temperature. Out of this we were able to see that there is a slight increase in the total polarization with increasing temperature.

8.2 Zusammenfassung

In den letzten Jahren ist das Interesse an Perowskit Solarzellen maßgeblich gestiegen. Die niedrigen Fabrikationskosten, die hohe Effizienz und die Leichtigkeit der Herstellung haben dazu wohl maßgeblich beigetragen. Daher haben wir in dieser Arbeit versucht das Verhalten der organischen Kationen aufzuklären. Dazu wurden ab-initio molekulare Dynamik Simulationen mit variierender Systemgrößen und unterschiedlichen Austausch-Korrelations-Potentialen durchgeführt. Aus diesen Simulationen konnten wir die bevorzugten mittleren Orientierungen der organischen Kationen, welche in den Perowskit Käfigen sitzen bestimmen. Daraus wird ersichtlich, dass die organischen Kationen die Raumdiagonalen der Perowskit Käfige vermeiden. Als nächstes haben wir versucht eine minimale Systemgröße festzulegen welche für die Simulationen benötigt wird. Die resultierende minimale Zellgröße sollte mindestens 4 Perowskit Einheitszellen in jede Raumrichtung enthalten und daher auch 4 organische Kationen. Ist dieser Sachverhalt nicht gegeben kann sich das Charakteristische Muster für die Räumliche Verteilung der organischen Kationen nicht ausbilden. Daraus folgt, dass die minimale Zelle mindestens 64 Einheitszellen und daher auch 64 organische Kationen enthalten muss. Als Maß für die Äquilibration wurden Autokorrelationsfunktionen der Simulationen mit verschiedenen Anfangsgeometrien, Zellgrößen und Potentialen herangezogen. Daraus wurde ersichtlich, dass Geometrien mit zufällig gewählten anfangs Orientierungen schneller äquilibrieren als jene Systeme wo zu Beginn alle Kationen in eine definierte Richtung zeigen. Bei dieser Analyse hat sich außerdem gezeigt, dass jene Simulationen mit berücksichtigten dispersen Interaktionen langsamer äquilibrieren als jene wo Wechselwirkungen dieser Art nicht berücksichtigt werden, was auf einen Anstieg der Rotationsbarrieren zurückzuführen ist.

Als nächstes haben wir die relative Orientierung der organischen Kationen in den verschiedenen koordinations Ebenen zu einander untersucht. Diese Untersuchung hat gezeigt, dass es ein wohldefiniertes Muster für die relative Orientierung der organischen Kationen zu einander gibt welches sich durch die verschiedenen Ebenen abwechselt. Aus dieser Beobachtung konnte des Weiteren gefolgert werden, dass es eine Fernordnung innerhalb der beobachteten Perowskit Systeme gibt.

Im zweiten Teil der ab-initio molekulare Dynamik Simulationen haben wir die Eigenschaften des anorganischen Gitters untersucht. Hier wurde ersichtlich, dass sich die Blei und Jod Atome nur um ihre Gleichgewichtspositionen bewegen. Des weiteren unterscheidet sich das Verhalten der anorganischen Bausteine in den verschiedenen Zellgrößen nicht und wird auch nicht durch die Wahl des Potentials beeinflusst.

Aus diesen Ergebnissen wurde nun versucht ein geeignetes Monte-Carlo Modell zu erstellen welches nur die organischen Kationen berücksichtigt. Die Parametrisierung für die Energie Berechnung wurde mit der sogenannten Boltzmann Inversion und den Ergebnissen aus den ab-initio Simulationen durchgeführt. Mit diesem Monte-Carlo Code besitzt man nun die Möglichkeit sehr große Systeme zu berechnen. Mit diesem Code haben wir die lokalen Polarisations-eigenschaften, welche durch die organischen Kationen herrühren, beobachtet. Diese Untersuchung hat gezeigt, dass sich kleine polarisierte Domänen innerhalb des Systems ausbilden, wobei die individuelle Polarisation der jeweiligen Domänen aber äußerst klein ist. Zum Abschluss haben wir noch den Zusammenhang der totalen Polarisation und der Temperatur betrachtet. Dabei hat sich gezeigt, dass die totale Polarisation der Zelle mit der Temperatur leicht ansteigt.

References

- [1] Field-theory calculation of the electric dipole moment of the neutron and paramagnetic atoms @ONLINE, 2015.
- [2] N. S. Akulov. Zur atomtheorie des ferromagnetismus. *Z. Phys*, 54, 1929.
- [3] Walsh Aron. Principles of chemical bonding and band gap engineering in hybrid organic- inorganic halide perovskites. *J. Phys. Chem.*, 119, 2015.
- [4] Arfken G. B. and Weber H. J. *Mathematical Methods for Physicists Sixth Edition*. Elsevier Academic Press, San Diego, California, 2003.
- [5] Vlasta Bonacic-Koutecky, Piercarlo Fantucci, and Jaroslav Koutecky. Quantum chemistry of small clusters of elements of groups ia, ib, and iia: Fundamental concepts, predictions, and interpretation of experiments. *Chem. Rev.*, 91, 1991.
- [6] Max Born and Julius R. Oppenheimer. Zur quantentheorie der molekeln. *Annalen der Physik*, 389.
- [7] Julian Burschka, Norman Pellet, Soo-Jin Monn, Robin Humphry-Baker, Peng Gao, Mohammad K. Nazeeruddin, and Michael Grtzel. Sequential deposition as a route to high-performance perovskite sensitized solar cells. *Nature*, 499, 2013.
- [8] Marcelo A. Carignano, Ali Kachmar, and Jürg Hutter. Thermal effects on ch3pbI3 perovskite from ab initio molecular dynamics simulations. *J. Phys. Chem.*, 119, 2015.
- [9] Roger Carr. Simulated annealing, 2015.
- [10] D. M. Ceperley and B. J. Alder. Ground state of the electron gas by a stochastic method. *Physical Review Letters*, 45, 1980.
- [11] Mariona Coll, Andres Gomez, Elena Mas-Marza, Osbel Almora, Germa Garcia-Belmonte, Mariano Cmpoy-Quilles, and Juan Bisquert. Polarization switching and light- enhanced piezoelectricity in lead halide perovskite. *Physical Chemistry Letters*, 6, 2015.
- [12] Lucian A. Constantin, Perdew John P., and Tao Jianmin. Meta-generalized gradient approximation for the exchange-correlation hole with an application to the jellium surface energy. *Physical Review B*, 73, 2006.
- [13] Lucian A. Constantin, Perdew John P., and Tao Jianmin. Meta-generalized gradient approximation for the exchange-correlation hole with an application to the jellium surface energy. *Physical Review B*, 73, 2006.
- [14] Manfred Drog. *Sealing with Uncertainties- A Guide to Error Analysis*. Springer-Verlag, Berlin, Heidelberg, 2009.
- [15] David A. Egger and Leor Kronik. Role of dispersive interactions in determining structural properties of organic- inorganic halide perovskites: Insights from first principle calculations. *The Journal of Physical Chemistry Letters*, 5, 2014.

- [16] Jarvis M. Frost, Keith T. Butler, Federico Brivio, Christopher H. Hendon, van Mark Schilfgaarde, and Aron Walsh. Atomistic origins of high- performance in hybrid halide perovskite solar cells. *Nano Letters*, 14, 2014.
- [17] Jarvis M. Frost, Keith T. Butler, and Aron Walsh. Molecular ferroelectric contributions to anomalous hysteresis in hybrid perovskite solar cells. *APL Materials*, 2, 2014.
- [18] Martin A. Green, Anita Ho-Baillie, and Henry J. Snaith. The emergence of perovskite solar cells. *Nature*, 8, 2014.
- [19] David J. Griffiths. *Introduction to Electrodynamics*. Prentice- Hall International, Inc., Upper Saddle River, New Jersey, 1999.
- [20] Stefan Grimme. Semiempirical gga- type density functional constructed with a long-range dispersion correction. *Journal of Computational Chemistry*, 27, 2006.
- [21] Stefan Grimme, Stephan Ehrlich, and Lars Goerigk. Effect of the damping function in dispersion corrected density functional theory. *Journal of Computational Chemistry*, 32, 2010.
- [22] Brandsen B. H. and Joachain C.J. *Physics of atoms and molecules*. Addison-Wesley, Reading, Massachusetts, 2003.
- [23] B. Hammer, L. B. Hansen, and J. K. Norskov. Improved adsorbtion energetics within density- functional theory using revised perdew- burke- ernzerhof functionals. *Physical Review B*, 59, 1999.
- [24] P. Hohenberg and Kohn W. Inhomogenous electron gas. *Physical Review*, 136, 1964.
- [25] Frank Jensen. *Introduction to Computational Chemistry*. John Wiley and Sons, West Sussex, 1999.
- [26] Eric Jones, Travis Oliphant, Pearu Peterson, et al. SciPy: Open source scientific tools for Python, 2001-. [Online; accessed 2015-10-15].
- [27] S. Kirkpatrick, C. D. Gelatt, and M. P. Vecchi. Optimization by simulated annealing. *Science*, 220, 1983.
- [28] Aurelien M. A. Leguy, Jarvis M. Frost, Andrew P. McMahon, Victoria G. Sakai, W. Kochelmann, ChunHung Law, Xiaoe Li, Fabrizia Foglia, Aron Walsh, Brian C. O'Regan, Jenny Nelson, J. T. Cabral, and Piers R. F. Barnes. The dynamics of methylammonium ions in hybrid organic -inorganic perovskite solar cells. *Nature Communications*, 2, 2015.
- [29] Elliot H. Lieb and Stephen Oxford. Improved lower bound on the indirect coulomb energy. *International Journal of Quantum Chemistry*.
- [30] Qianqian Lin, Ardalan Armin, C. R. Nagiri, Ravi, Paul L. Burn, and Paul Meredith. Electro-optics of perovskite solar cells. *nature photonics*, 2014.
- [31] Shang-Keng Ma and Keith A. Brueckner. Correlation energy of an electron gas with a slowly varying high density. *Physical Review Letters*, 100, 2008.

- [32] G. Mahajani. A contribution to the theory of ferromagnetic crystals. *Philosophical Transactions of the Royal Society A*, 228, 1929.
- [33] Richard M. Martin. *Electronic Structure- Basic Theory and Practical Methods*. Cambridge University Press, University Press, Cambridge, 2004.
- [34] Nicole K. McKinnon, David C. Reeves, and Myles H. Akabas. 5-HT₃ receptor ion size selectivity is a property of the transmembrane channel, not the cytoplasmic vestibule portals. *The Journal of General Physiology*, 4, 2011.
- [35] N. Metropolis, A. W. Rosenbluth, M. N. Rosenbluth, A. H. Teller, and E. Teller. Equation of state calculations by fast computing machines. *Journal of Chemical Physics*, 21, 1953.
- [36] Allen M. P. and Tildesley D. J. *Simulations of Liquids*. Oxford University Press, New York, United States, 1987.
- [37] Landau David P. and Kurt Binder. *A Guide to Monte Carlo Simulations in Statistical Physics*. Cambridge University Press, New York, 2000.
- [38] Nam-Gyu Park. Organometal perovskite light absorbers toward a 20% efficiency low-cost solid-state mesoscopic solar cell. *The Journal of Physical Chemistry Letters*, 4, 2013.
- [39] Nam-Gyu Park. Perovskite solar cells: an emerging photovoltaic technology. *Mater. Today (Oxford, U. K.)*, 18, 2014.
- [40] John P. Perdew, Kieron Burke, and Matthias Ernzerhof. Generalized gradient approximation made simple. *Physical Review Letters*, 77, 1996.
- [41] John. P. Perdew, Lucian A. Constantin, E. Sagvolden, and Kieron Burke. Relevance of the slowly varying electron gas to atoms, molecules, and solids. *Physical Review Letters*, 97, 2006.
- [42] John P. Perdew, Adrienn Ruzsinszky, Gabor I. Csonka, Oleg A. Vydrov, Gustavo E. Scuseria, Lucian A. Constantin, Xiaolan Zhou, and Kieron Burke. Restoring the density- gradient expansion for exchange in solids and surfaces. *Physical Review Letters*, 100, 2008.
- [43] J. M. Pitarke and J. P. Perdew. Metal surface energy: Persistent cancellation of short-range correlation effects beyond the random phase approximation. *Physical Review B*, 67, 2003.
- [44] Claudio Quarti, Edoardo Mosconi, and Filippo De Angelis. Structural and electronic properties of organo-halide hybrid perovskites from ab initio molecular dynamics. *Phys.Chem.Chem.Phys*, 17, 2015.
- [45] Robert F. Service. Perovskite solar cells keep on surging. *Science*, 344, 2014.
- [46] Constantinos C. Stoumpos, Christos D. Malliakas, and Mercouri G. Kanatzidis. Semi-conducting tin and lead iodide perovskites with organic cations: Phase transitions, high mobilities, and near-infrared photoluminescent properties. *Inorganic Chemistry*, 52, 2013.

- [47] Jianmin Tao, Staroverov, Viktor N., Scuseria Gustavo E., and John P. Perdew. Exact-exchange energy density in the gauge of a semilocal density-functional approximation. *Physical Review A*, 77, 2008.
- [48] Loup Verlet. Computer "experiments" on classical fluids. i. thermodynamical properties of lennard jones molecules. *Physical Review*, 159, 1967.
- [49] von Barth U. and Hedin L. A local exchange-correlation potential for spin polarized case:i. *J. Phys. C:Solid State Phys.*, 5, 1972.
- [50] Kohn W. Nobel lecture: Electronic structure of matter- wave functions and density functionals. *Reviews of Modern Physics*, 71, 1999.
- [51] Kohn W. and Sham L.J. Self- consistent equations including exchange and correlation effects. *Physical Review*, 140, 1965.
- [52] R. E. Wasylishen, Osvald Knop, and J. B. Macdonald. Cation rotation in methylammonium lead halides. *Solid State Communications*, 56, 1985.
- [53] Hagen Wierstorf. Gnuplotting- create scientific plots using gnuplot, Nov. 2015.
- [54] Eugene P. Wigner. Effects of the electron interaction on the energy levels of electrons in metals. *Transactions Faraday Society*, 34, 1938.
- [55] Eugene P. Wigner. On the interaction of electrons in metals. *Physical Review*, 46, 1994.
- [56] Yingkai Zhang and Weitao Yang. Comment on "generalized gradient approximation made simple". *Physical Review Letters*, 80, 1998.